PONTIFICIA
UNIVERSIDAD
CATÓLICA
DE CHILE

FACULTAD DE FÍSICA
INSTITUTO DE FÍSICA

# GAS ADSORPTION PROPERTIES OF COMPLEX COPPER OXIDES.

by
Susana Dennis Rojas de la Fuente

Thesis presented at Facultad de Física of Pontificia Universidad Católica de Chile, as a partial requirement for the degree of Doctor in Physics.

| | |
|---|---|
| Thesis Advisor | : Dr. Alejandro Cabrera |
| Dissertation Committee | : Dr. Víctor Fuenzalida |
| | Dr. Samuel Hevia |
| | Dr. David Lederman |
| | Dr. José Mejía |

Octubre, 2017
Santiago, Chile
©2017, Susana Dennis Rojas de la Fuente

# Thesis reproduction authorization

©2017, Susana Dennis Rojas de la Fuente

Total or partial reproduction, for academic purposes, is authorized by any means or process, including the citation that accredits the work and its author.

Date:

Firma:

Av. Blanco Encalada 1797, dpto. 2005, Santiago, Chile
sdrojas1@uc.cl - +56 9 7967 2993

# ACKNOWLEDGMENTS

In first place, I would like to thank to Dr. Alejandro Cabrera for his constant support during this process, in which without his advice and support this thesis would not have come to fruition.

I will also, thank to Prof. Lederman's group at West Virginia University, in special Toyanath Joshi for growing the stack of samples studied during this work.

Special thanks to **CONICyT** for its economic support under the **National Doctor scholarship 2013 admission (*beca de doctorado nacional 2013*)**, and to **FONDECYT proyect Nº1130372** in charge of Dr. Alejandro Cabrera.

Finally, but not less important I would like to thank my family and friend for all their emotional support during this entire process, specially to my husband who was constantly encouraging me to continue and finish as soon as possible this work.

# Vita

| | |
|---|---|
| 13 October 1989 | Born – Santiago, Chile |
| 2008-2012 | Licenciate in Physics, Pontificia Universidad Católica de Chile, Santiago |
| 2013 – 2017 | Doctor in Physics, Pontificia Universidad Católica de Chile, Santiago |

# Publications

*"Comparative study of the structural and optical properties of epitaxial $CuFeO_2$ and $CuFe_{1-x}Ga_xO_2$ delafossite thin films grown by pulsed laser deposition methods"*, R.A. Wheatley, **S. Rojas**, C. Oppolzer, T. Joshi, P. Borisov, D. Lederman, A.L. Cabrera, Thin Solid Films 626 (2017) 110-116, DOI: 10.1016/j.tsf.2017.02.005

*"Carbon dioxide adsorption studies on delafossite $CuFeO_2$ hydrothermally synthesized",* Sarabia, M. A., **Rojas, S. D.**, López-Cabaña, Z., Villalba, R., González, G., & Cabrera, A. L. Journal of Physics and Chemistry of Solids 98(2016), 271-279.

*"Optical detection of carbon dioxide adsorption on epitaxial $CuFe_{1-x}Ga_xO_2$ Delafossite film grown by pulse laser deposition"*, **S. Rojas**, T. Joshi, R.A. Wheatley, M. Sarabia, P. Borisov, D. Lederman, A.L. Cabrera, Surface Science (2015), DOI:10.1016/j.susc.2015.10.018

# Fields of Study

Major Field: Physics

Studies in Surface Sciences

Professor A.L. Cabrera

# Table of Contents

**Thesis reproduction authorization** ..... **i**

**ACKNOWLEDGMENTS** ..... **ii**

**Vita** ..... **iii**

**Publications** ..... **iii**

**Fields of Study** ..... **iv**

**Table of Contents** ..... **v**

**Index of Tables** ..... **viii**

**Index of Figures** ..... **ix**

**Summary** ..... **xiv**

**Chapter 1: Introduction** ..... **1**

**1.1 Motivation** ..... **1**

1.1.1. Environmental and Energy Problems ..... 1

1.1.2. Hydrogen as a Source of Energy ..... 5

1.1.3. Reforming of $CO_2$ ..... 7

1.1.4. Catalyst Requirements ..... 9

**1.2. Complex Oxides** ..... **12**

1.2.1. Delafossite Type Oxides ..... 12

**1.3. Objectives** ..... **15**

1.3.1. Samples Description ..... 16

**Chapter 2: Experimental Setup** ..... **18**

**2.1. Samples Characterization.** ..... **18**

2.1.1. X-Ray Diffraction (XRD). ..... 18

2.1.2. Raman Spectroscopy. 18
2.1.3. X-ray Photoelectron Spectroscopy (XPS). 18
2.1.4. Optical Transmittance and Difuse Reflectance. 19
**2.2. Gas Absorption properties. 20**
2.2.1. Thermal Programmed Desorption (TPD) Vacuum System 20

**Chapter 3: Results and Discussion. 24**
**3.1. Characterization. 24**
3.1.1. X-Ray Difraction (XRD) 24
3.1.2. Raman Spectroscopy. 30
3.1.3. X-Ray Photoelectron Spectroscopy (XPS) 35
3.1.4. Optical Transmittance and Diffuse reflectance. 39
**3.2. Gas Adsorption Properties. 45**
3.2.1. Thermal Programmed Desorption. 47

**Chapter 4: Conclusions and Future work. 56**
**4.1. Conclusions. 56**
**4.2. Future work. 57**

**Appendix. 59**
**Appendix A. Other Results. 59**
Appendix A.1. X-Ray Diffraction 59
Appendix A.2. Raman Spectroscopy. 65
Appendix A.3. X-Ray Photoelectron Spectroscopy 67
Appendix A.4. Thermal Programmed Desorption. 71
**Appendix B. Gas adsorption and catalysis 77**
**Appendix C. Kinetics of Desorption 81**
Appendix C.1. Rate Equation 81
Appendix C.2. Thermal Programmed Desorption of gases 83
**Appendix D. Appendix A: Thermal desorption spectrum correction. 86**
Appendix D.1. Cracking Pattern correction. 86

Appendix D.2. Sample holder desorption subtraction. ..... 89
**Appendix E. X-ray Photoelectron Spectroscopy (XPS) ..... 90**
**Appendix F. X-ray Diffraction (XRD) and Grazing Incidence Diffraction (GID) ..... 92**
**Appendix G. Raman Spectroscopy ..... 95**
**Appendix H. : Tauc Equation ..... 97**
**References ..... 99**

# Index of Tables

Table 1-1: Summary of thermodynamic potentials of $CO_2$ reduction to various products 8
Table 1-2: Samples description, thickness and calculated c lattice parameter. ..... 17
Table 3-1: parameters used for fitting GID pattern according to a multi lattice approach for $CuFe_{0.75}Ga_{0.25}O_2$ sample. ..... 27
Table 3-2: Parameters used for GID pattern fitting according to alloyed structure approach for $CuFe_{0.75}Ga_{0.25}O_2$ sample. ..... 29
Table 3-3: Summary of $E_g$ and $A_{1g}$ Raman peak position for al samples. ..... 32
Table 3-4: Summary of all measurable direct transitions from Tauc plots. ..... 45
Table 3-5: relative intensities of gases desorbed by samples. ..... 49
Table 3-6: Summary of activation energy of desorption obtained from curves fitting of thermal desorption spectra. Sub index enumerate peaks on the fitting. ..... 53
Table 4-1: XRD pattern peaks position and calculated c lattice parameter for all $CuFeO_2$ samples. Reference for $CuFeO_2$ peak position was obtained from JCP2 chart #00-039-0246. ..... 63
Table 4-2: XRD pattern peaks position and calculated c lattice parameters for all $CuFe_{0.75}Ga_{0.25}O_2$ samples. Reference for $CuFeO_2$ and $CuGaO_2$ peak position was obtained from JCP2 chart #00-039-0246 and #00-041-0255. ..... 64
Table 4-3: Fitting parameters for $H_2O$ TPD spectra on selected samples. ..... 74
Table 4-4: Fitting parameters for $CO_2$ TPD spectra on selected samples. ..... 75
Table 4-5: Fitting parameters for CO TPD spectra on selected samples. ..... 76
Table 4-6 : Principal x-rays wavelength produced by a copper source. These x-rays were used in our study. ..... 93

# Index of Figures

Figure 1-1: Top: World-wide fuel consumption over time [1]. Bottom: Total greenhouse gases emission over time [2]. 2
Figure 1-2: Greenhouse effect explicative diagram. 3
Figure 1-3: Temperature anomaly records over the time for global and south and north hemispheres [3], [ 4]. 4
Figure 1-4: schematic diagram of the photocatalytic water splitting 7
Figure 1-5: Schematic diagram of a photo-electrochemical carbon dioxide reduction mediated by photocatalytic water splitting. 9
Figure 1-6: Band structure on selected materials, contribution of metal cation and oxygen anion states to the conduction and valence bands. The bandgap energy (red for n-type, black for p-type) is shown with respect to the reversible hydrogen electrode and the water redox energy levels (assuming Nernstian behavior for the band-edge energies with respect to electrolyte pH). Reprinted by permission from Macmillan Publishers Ltd: Nature Reviews Materials (reference num. 14), copyright 2017. 11
Figure 1-7: (a) The crystal structure of the Delafossite compounds. (b) The calculated band-structures of the CuMO2 compounds from the X-LDA method. Reproduced from Ref 24 with permission of the PCCP Owner Societies. 14
Figure 2-1: Experimental transmittance and reflectance spectroscopy system. The incidence angle is 8°. P1, P2, and P3 stand for the silicon photodiodes. Photodiode P3 monitors the incident intensity to normalize the reflected and transmitted signals measured by P1 and P2 in case of lamp intensity variations. The chopper frequency is around 960 Hz. The wavelength range 400–900 nm is limited by the tungsten halogen lamp spectrum and second order diffraction in the monochromator [32]. 19
Figure 2-2: Scheme of the vacuum system used for the TPD experiments. (a) Mechanical pump. (b) Adixen ATP150 Turbo pump. (c) Mass spectrometer RGA 200, Stanford Research Systems. (d) $CO_2$ high pressure tank. (e) Hot cathode gauge. (f) Ar high pressure tank. (g) Ar+ Sputtering Ion Source IQE 11/35, Specs. (h) STAIB RQ300X X-ray. (i) Auger spectrometer DESA 100, STAIB Instruments. (j) Sample holder. 21
Figure 2-3: Home-made sample holder schematic 23
Figure 3-1: X-ray diffraction pattern for $CuFeO_2$ samples of 75 nm (red line, CFO161) and 21 nm (blue line, CFO133), black labeled peaks correspond to $CuFeO_2$ peaks and red labeled peaks correspond to $CuFe_2O_4$ spinel material. 25

Figure 3-2: XRD patter of $CuFe_{0.75}Ga_{0.25}O_2$ 48 nm thick sample (CFOCGO7), black labeled peaks correspond to $CuFeO_2$ peaks and red labeled peaks correspond to $CuFe_2O_4$ spinel material. In the inset is the rocking curve of the (006) peak. ..... 26
Figure 3-3: GID diffraction pattern for $CuFe_{0.75}Ga_{0.25}O_2$ 48 nm thickness (CFOCGO7) with fit considering the multi lattice model (top) and schematic diagram of the multi lattice structure of the sample. ..... 28
Figure 3-4: GID diffraction pattern for $CuFe_{0.75}Ga_{0.25}O_2$ 48 nm thickness (CFOCGO7) with fit considering the alloy model (top) and schematic diagram of the alloyed structure of the sample. ..... 30
Figure 3-5: Raman spectra of (black) $CuFeO_2$ 75 nm thickness (CFO161) and (blue) $CuFe_{0.75}Ga_{0.25}O_2$ 48 nm thickness (CFOCGO7). ..... 31
Figure 3-6: (a) Simulated Raman spectrum of $CuFe_{0.75}Ga_{0.25}O_2$. (b) comparison between $CuFe_{0.75}Ga_{0.25}O_2$ simulated Raman spectrum and experimentally obtained Raman spectrum from 48 nm thickness sample (CFOCGO7). ..... 34
Figure 3-7: X-ray Photoelectron survey spectrum of $CuFeO_2$ 100 nm thickness (CFO168) sample with principal peaks identified, peaks labeled with * correspond to sample holder peaks. ..... 35
Figure 3-8: XPS High resolution scans for (a) Cu 2p and (b) Fe 2p peaks for $CuFeO_2$ film 100 nm in thickness (CFO168) and peak fitting considering different oxidation states. ..... 36
Figure 3-9: X-ray Photoelectron survey spectrum of $CuFe_{0.75}Ga_{0.25}O_2$ 48 nm thickness (CFOCGO7) sample with principal peaks identified, peaks labeled with * correspond to sample holder peaks. ..... 37
Figure 3-10: XPS High resolution scans for (a) Cu 2p and (b) Fe 2p peaks for $CuFe_{0.75}Ga_{0.25}O_2$ film 48 nm in thickness (CFOCGO7) and peak fitting considering different oxidation states. ..... 38
Figure 3-11: (a) Transmittance and (b) diffuse reflectance spectra in the near infrared and visible spectra measured for both kinds of samples (CFO133 in black, CFO161in green and CFOCGO7 in blue). ..... 40
Figure 3-12: Tauc Plots for direct band gap obtained from (a) transmittance and (b) diffuse reflectance of $CuFeO_2$ 21 nm sample (CFO133). ..... 41
Figure 3-13: Tauc plots for direct transition obtained from (a) transmittance and (b) diffuse reflectance for $CuFe_{0.75}Ga_{0.25}O_2$ 48 nm thickness sample (CFOCGO7). ..... 43
Figure 3-14: XPS high resolution spectra of (a) Cu 2p and (b) Fe 2p before and after $CO_2$ exposure of $CuFeO_2$ film 75nm in thickness sample (CFO161). ..... 46
Figure 3-15: XPS measurements of O1s and C1s bands for $CuFeO_2$ 75 nm film (CFO161) before and after $CO_2$ exposure. ..... 47

Figure 3-16: Thermal desorption spectra of (a) $CuFeO_2$ 100 nm thickness (CFO168) after 1500L dose and heating rate $14.5 \pm 0.3$ K/s and (b) $CuFe_{0.75}Ga_{0.25}O_2$ 48 nm thickness (CFOCGO7) after 4500L and heating rate $25.4 \pm 0.7$ K/s. ..... 48
Figure 3-17: Peak fitting of $H_2O$ TPD spectra of (a) $CuFe_{0.75}Ga_{0.25}O_2$ film 48 nm in thickness (CFOCGO7) and (b) $CuFeO_2$ film 100 nm in thickness (CFO168). ..... 50
Figure 3-18: Peak fitting of $CO_2$ TPD spectra of (a) $CuFe_{0.75}Ga_{0.25}O_2$ film 48 nm in thickness (CFOCGO7) and (b) $CuFeO_2$ film 100 nm in thickness (CFO168). ..... 51
Figure 3-19: Peak fitting of CO TPD spectra of (a) $CuFe_{0.75}Ga_{0.25}O_2$ film 48 nm in thickness and (b) $CuFeO_2$ film 100 nm in thickness..... 52
Figure 4-1: XRD Pattern for $CuFeO_2$ 25 nm thickness (FCO163) sample. Inset figure correspond to rocking curve in (006) direction peak. ..... 59
Figure 4-2: XRD Pattern for $CuFeO_2$ 100 nm thickness (FCO168) sample. Inset figure correspond to rocking curve in (006) direction peak. ..... 60
Figure 4-3: XRD Pattern for $CuFe_{0.75}Ga_{0.25}O_2$ 95 nm thickness (FCOCGO8) sample. Inset figure correspond to rocking curve in (006) direction peak..... 60
Figure 4-4: (006) direction peak comparison between $CuFe_{0.75}Ga_{0.25}O_2$ 95 nm thickness (FCOCGO8) sample and theoretical simulation. ..... 61
Figure 4-5: XRD Pattern for $CuFe_{0.75}Ga_{0.25}O_2$ 20 nm thickness (FCOCGO10) sample. Inset figure correspond to rocking curve in (006) direction peak..... 61
Figure 4-6: (006) direction peak comparison between $CuFe_{0.75}Ga_{0.25}O_2$ 20 nm thickness (FCOCGO10) sample and theoretical simulation. ..... 62
Figure 4-7: (006) direction peak comparison between $CuFe_{0.75}Ga_{0.25}O_2$ 48 nm thickness (FCOCGO7) sample and theoretical simulation. ..... 62
Figure 4-8: Raman spectra of all $CuFeO_2$ samples (CFO133, CFO163, CFO161, CFO168). ..... 65
Figure 4-9: Raman spectra of all $CuFe_{0.75}Ga_{0.25}O_2$ samples (CFOCGO10, CFOCGO7, CFOCGO8). ..... 65
Figure 4-10: Comparison between $CuFe_{0.75}Ga_{0.25}O_2$ simulated Raman spectrum and experimentally obtained Raman spectrum from 20 nm thickness sample (CFOCGO10). ..... 66
Figure 4-11: Comparison between $CuFe_{0.75}Ga_{0.25}O_2$ simulated Raman spectrum and experimentally obtained Raman spectrum from 95 nm thickness sample (CFOCGO8). 66
Figure 4-12: X-ray Photoelectron survey spectrum of $CuFe_{0.75}Ga_{0.25}O_2$ 95 nm thickness (CFOCGO8) sample with principal peaks identified, peaks labeled with * correspond to sample holder peaks. ..... 67
Figure 4-13: XPS High resolution scan of (a) Cu 2p and (b) Fe 2p lines for $CuFe_{0.75}Ga_{0.25}O_2$ 95 nm thickness (CFOCGO8) sample. ..... 68

Figure 4-14: X-ray Photoelectron survey spectrum of $CuFeO_2$ 75 nm thickness (CFO161) sample with principal peaks identified. ..... 69
Figure 4-15: XPS High resolution scans for (a) Cu 2p and (b) Fe 2p peaks for CuFeO2 film 75 nm in thickness (CFO161) and peak fitting considering different oxidation states. ..... 69
Figure 4-16:X-ray Photoelectron survey spectrum of $CuFeO_2$ 21 nm thickness (CFO133) sample with principal peaks identified. ..... 70
Figure 4-17: XPS high resolution spectra of (a) Cu 2p and (b) Fe 2p after $CO_2$ exposure of $CuFe_{0.75}Ga_{0.25}O_2$ film 48 nm in thickness (CFOCGO7) sample. ..... 71
Figure 4-18: XPS measurements of C1s band for $CuFe_{0.75}Ga_{0.25}O_2$ 48 nm film (a) before and (b) after $CO_2$ exposure. ..... 72
Figure 4-19: XPS measurements of O 1s band for $CuFe_{0.75}Ga_{0.25}O_2$ 48 nm film (a) before and (b) after $CO_2$ exposure. ..... 73
Figure 4-20: Energetics of the reaction: $A + B \rightarrow C + D$ ..... 78
Figure 4-21: LennardeJones potential energy diagram for the adsorption of hydrogen on a metal surface; as the hydrogen molecule approaches the surface from the right-hand side, it becomes physically adsorbed and then, following dissociation in the region of the Surface. ..... 80
Figure 4-22: schematic representation of the catalyzed reaction: $A + B \rightarrow C + D$ ..... 81
Figure 4-23: Normalized graphics of a first ($E = 91.5\ \mathrm{kcal/mol}$) and second order ($E = 87\ \mathrm{kcal/mol}$) desorption, using linear temperature rates ($TP = 1400\mathrm{K}$). These numerical parameters represent the β-phase desorption of $N_2$ in W [52]. ..... 85
Figure 4-24: Schematic diagram of hardware of the mass spectrometer. ..... 87
Figure 4-25: Gas fragmentation pattern of water obtained from RGA library. ..... 88
Figure 4-26: Gas fragmentation pattern for (a) $CO_2$ and (b) CO gases obtained from RGA software library ..... 89
Figure 4-27: Thermal desorption spectra comparison for $CuFeO_2$ samples and substrate for water desorption. ..... 90
Figure 4-28: schematic diagram of the XPS system used for this work ..... 92
Figure 4-29: Scheme of diffraction produced in x-rays by a crystalline structure. The distance between the atoms d and diffraction angle θ are related by the Braggs law ..... 93
Figure 4-30: Differences between GID (a) and XRD (b) setups. In GID the x-ray source is keep at a constant small angle α, while in XRD source and detector are moved. ..... 94
Figure 4-31: Possible electronic transitions due to interactions between photon and molecule ..... 96

# Summary

Highly epitaxial films of $CuFeO_2$ and $CuFe_{0.75}Ga_{0.25}O_2$ were grown by pulsed laser deposition (PLD) from stoichiometric targets over $Al_2O_3$ (001) substrate under controlled partial pressure of oxygen as carrier gas. Resulting films were highly oriented in c-axis direction.

Structural properties of samples were characterized by X-Ray Diffraction (XRD), Raman spectroscopy, X-Ray Photoelectron Spectroscopy (XPS), optical transmittance and diffuse reflectance. This characterization techniques confirmed the rhombohedral Delafossite crystal structure for both kind of samples and $CuFe_{0.75}Ga_{0.25}O_2$ samples were formed by an alloy between $CuFeO_2$ and $CuGaO_2$ Delafossite materials. Using optical transmittance and diffuse reflectance, the optical transitions were estimated by using the Tauc method. Direct optical transitions were measured at 1.28±0.02 eV and 2.20±0.05 eV for pure $CuFeO_2$ samples and for $CuFe_{0.75}Ga_{0.25}O_2$ were measured at 1.50±0.04 eV and 2.30±0.09 eV, plots showed another higher transition near 3 eV but due to technical limitations this gap cannot be clearly determined.

Adsorption of $CO_2$ and $H_2O$ was studied via thermal programmed desorption technique. In both films Copper and Iron were present at the surface, and consequently formed part of the surface-gas interface. X-ray photoelectron data indicated that $CO_2$ is adsorbed preferentially at copper sites forming a similar coordination to $CuCO_3$. The energy for desorption of $CO_2$ and $H_2O$ was estimated to be 1.0±0.8 eV/molecule for $CuFeO_2$ and 0.7±0.4 eV/molecule for $CuFe_{0.75}Ga_{0.25}O_2$. Also, it was possible to correlate second order desorption with a $CO_2$ reduction reaction.

Copper Delafossite materials studied in this work showed some catalytic activity in good agreement with the literature. Future work in this field would involve synthesis of a

wider variety of $CuFe_{1-x}Ga_xO_2$ samples in order to get a better idea of the influence of iron substitution for gallium in the Delafossite structure. Also, for a better understanding of the relationship between adsorption properties and catalytic behavior some future work regarding electrical and electrochemical properties is proposed.

# Chapter 1: Introduction

## 1.1 Motivation

### 1.1.1. Environmental and Energy Problems

Industrial and technological development are some of the most important achievements reached by humankind. This development was expedited by the use of coal combustion to produce mechanical energy since the XVIII century originating the industrial revolution. Later, electrical energy was produced using different kinds of hydrocarbons as fuel for combustion. Since that point in history our society began to rely more and more on the use of energy for our daily life.

Energy generation has become a very important issue in our society because as the world-wide population keeps increasing and our technological demands also increase, consequently, the energy demand is increasing at a high rate, as shown in Figure 1-1(top chart).

The most important problem regarding the energy dependence and excessive use of it in our society is that most of this energy still comes from hydrocarbon combustion. The two main reasons that make it a problem are: firstly, we have a limited amount of hydrocarbons on the earth and its supplies will be exhausted at some point. And secondly, the massive combustion of hydrocarbons is generating pollution all over the world (see Figure 1-1 bottom) and its consequences for the environment are becoming more and more dangerous with time.

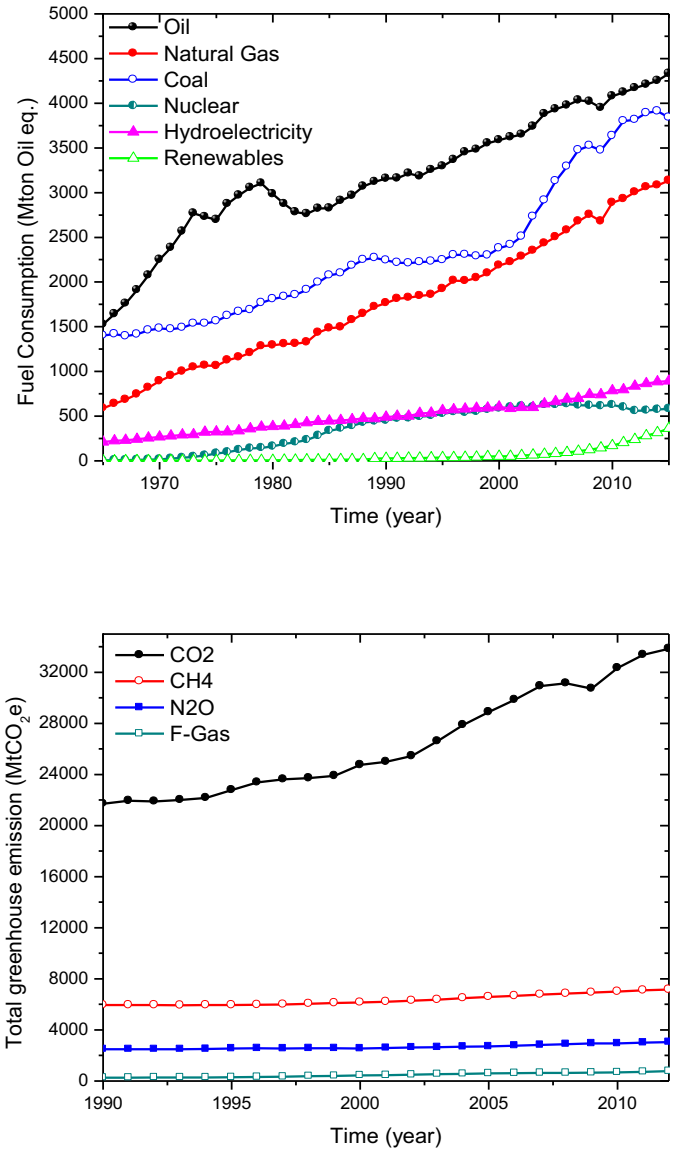


**Figure 1-1: Top:** World-wide fuel consumption over time [1]. Bottom: Total greenhouse gases emission over time [2].

The resulting substances from a combustion of any organic compound are water and carbon dioxide. These compounds as well as many other compounds from the combustion of synthetic materials or contaminated hydrocarbons are the so well-known

greenhouse gases. When these gases are in the atmosphere they prevent the thermal energy from going out from the earth causing a slightly increase of the average temperature on the atmosphere. If this effect is maintained during long periods of time we are facing the so called global warming effect that may cause several environmental problems due to the loss of the equilibrium of the global ecosystem.

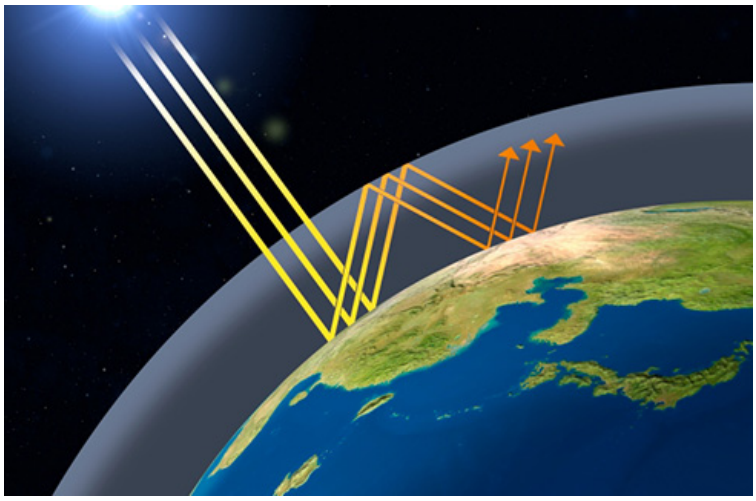

**Figure 1-2:** Greenhouse effect explicative diagram.

There are some alarming statistics that aware global society about how fast is this global warming has been happening during the last century. Some climate changes are occurring: global temperature is increasing, as it can be seen on chart from Figure 1-3, and the future perspectives are discouraging if we don't make any changes in the actual way of living or on the energy sources that we use.

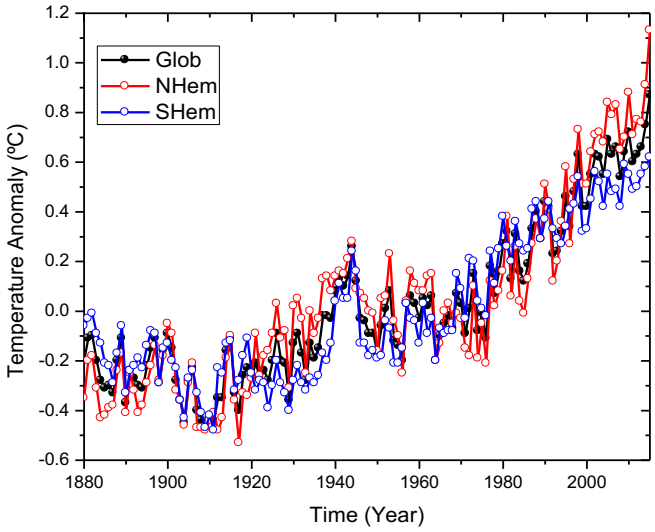


**Figure 1-3:** Temperature anomaly records over the time for global and south and north hemispheres [3], [ 4].

Given this, one of the viable solutions for all these problems is to completely change our energy generation system to more environmentally friendly sources such as solar and wind energy, but one of the main difficulties with these systems is the low efficiency and high costs of production.

To achieve a sustainable society with an energy mix primarily based on solar energy, it is critical to develop methods for storing energy from sunlight as chemical fuels. Photo-electrochemical devices offer the promise of solar fuel production through artificial photo-synthesis. So, in this situation hydrogen energy appears as a suitable energy source. Another possible solution is to find out the way to reinvest all these greenhouse gases in order to close the cycle and avoid the accumulation of greenhouse gases in the atmosphere. This would solve the environmental problems and will also make hydrocarbons a “renewable” fuel.

### 1.1.2. Hydrogen as a Source of Energy

Hydrogen as a source of energy is one solution to the energy and environmental problems that will be discussed in more detail.

Hydrogen is the lightest element on the periodic table and is the fuel with the highest energy density per mass unit (142 $MJkg^{-1}$) [5, 6]. Due to these characteristics the International Energy Agency [7] did some research on the impact that a worldwide use of hydrogen as an energy source will have. In this research the International Energy Agency report that the carbon dioxide emissions would be reduced by 5%.

However, the main difficulty for the transition to a hydrogen system is the lack of appropriate technology for hydrogen generation, storage, transport and distribution because actual technology is expensive compared to the hydrocarbons combustion system [8].

Many of the existent hydrogen storage systems are expensive, too heavy, use huge volumes and/or are unsafe. For example, if 400 km of independence is needed for an electric car that uses hydrogen as fuel, it would need at least 4 kg of hydrogen, and if we choose to transport it as a molecular gas these four kilograms will have a 45 $m^3$ volume at room temperature and atmospheric pressure [8].

Also, clean hydrogen generation is one of the most important challenges of the hydrogen energy field. Currently most hydrogen is produced from hydrocarbons by steam reforming or partial oxidation of methane and coal gasification. These technologies constitute near 95% of the hydrogen industry leaving just a small quantity of hydrogen that comes from more environmental friendly sources such as biomass gasification and water electrolysis [9].

Water electrolysis mediated by a photocatalytic process appears as one of the most promising methods for hydrogen generation. The photocatalytic water splitting is an artificial photosynthesis process where the photo-catalysis takes place in a photo-electrochemical cell used for the dissociation of water into its constituent parts using light. This method is being investigated due to its promising results. In theory, this method promises low cost hydrogen generation because only solar energy, water and a catalyst are needed. It has the simplicity of using a powder solution and sunlight to produce $H_2$ and $O_2$ from water and can provide a clean, renewable energy without producing greenhouse gases or having many adverse effects on the atmosphere.

Photocatalytic water splitting is described by

$$2H_2O \rightarrow 2H_2 + O_2 \qquad (1\text{-}1)$$

This method is mediated by photons reaching the catalyst with energy equal or greater than the semiconductor bandgap generating an electron vacancy pair generating a potential difference between balance and conduction bands. This potential will attract hydrogen ions to the conduction band (negatively charged) and oxygen ions to the balance band to finally generate hydrogen and oxygen molecules. The most important requirement for an effective photo-catalyst for water splitting is that the potential difference (voltage) must be 1.23 V at 0 pH [10]. Since the minimum band gap for successful water splitting at pH=0 is 1.23 eV, corresponding to light of 1008 nm, the electrochemical requirements can theoretically reach down into infrared light.

The conversion of solar energy to hydrogen by means of photo-catalysis is one of the most interesting ways to achieve clean and renewable energy systems. However, if this process is assisted by photo-catalysts suspended directly in water instead of using a photovoltaic and electrolytic system the reaction is in just one step, and the

semiconductor bandgap of the catalyst is adjusted to the solar emission peak. This process can therefore be more efficient [11], [12].

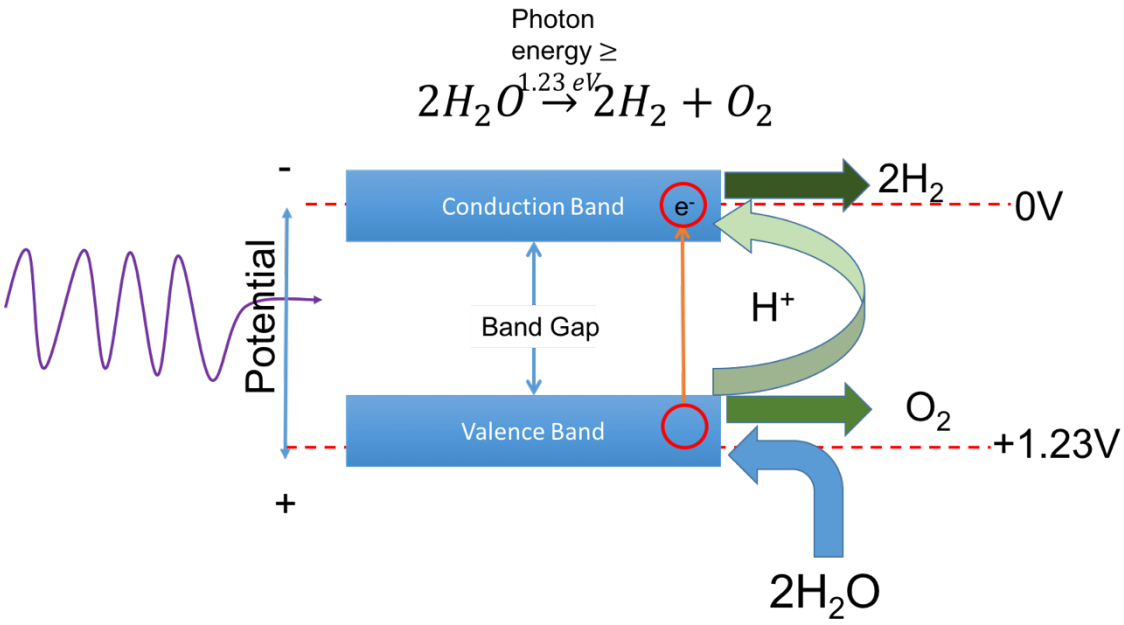


**Figure 1-4:** schematic diagram of the photocatalytic water splitting

Hydrogen generation and storage are very important research topics around the world because it seems to be a highly efficient and simple method for storing energy harvested from sunlight [13].

### 1.1.3. Reforming of $CO_2$

Another suitable solution for the incoming environmental problems is to find out a way to re-use the greenhouse gases to reduce the amount of them in the atmosphere. As shown in Figure 1-1, carbon dioxide is the most abundant greenhouse gas generated and in this way $CO_2$ reforming is a good solution for the environmental and energy problem described in section 1.1.1.

In this way photo-electrochemical reduction of $CO_2$ has captured the attention of researchers motivated by a possible reduction and sequestration of atmospheric $CO_2$. In this process carbon dioxide is reduced to carbon monoxide or hydrocarbons by the energy of incident light. This process needs to be catalyzed either homogenously or heterogeneously in order to proceed.

Carbon dioxide reduction can be performed in different ways thus obtaining different results depending on the amount of hydrogen present and the potential applied during the catalysis. Some common reductions are summarized on Table 1-1.

| $CO_2$ reduction | Thermodynamic potential |
|---|---|
| $CO_2 + 2H^+ + 2e^- \rightarrow CO + H_2O$ | $E^0 = -0.53V$ |
| $CO_2 + 2H^+ + 2e^- \rightarrow HCO_2H$ | $E^0 = -0.61V$ |
| $CO_2 + 4H^+ + 4e^- \rightarrow HCHO + H_2O$ | $E^0 = -0.48V$ |
| $CO_2 + 6H^+ + 6e^- \rightarrow CH_3OH + H_2O$ | $E^0 = -0.38V$ |
| $CO_2 + 8H^+ + 8e^- \rightarrow CH_4 + 2H_2O$ | $E^0 = -0.24V$ |
| $CO_2 + e^- \rightarrow CO_2^-$ | $E^0 = -1.90V$ |

**Table 1-1:** Summary of thermodynamic potentials of $CO_2$ reduction to various products

As most if these reactions use hydrogen ions for carbon dioxide reduction, it is desirable to perform a two steps photo-catalysis, where photocatalytic water splitting occurs firstly and then the resulting hydrogen ions are used for the $CO_2$ reduction as described in Figure 1-5.

One of the main difficulties for developing appropriate systems for photo-electrochemical reduction of $CO_2$ and photocatalytic water splitting is to find out the right semiconductor material to act as catalyst. There is a wide variety of semiconductor materials available in nature or man-made.

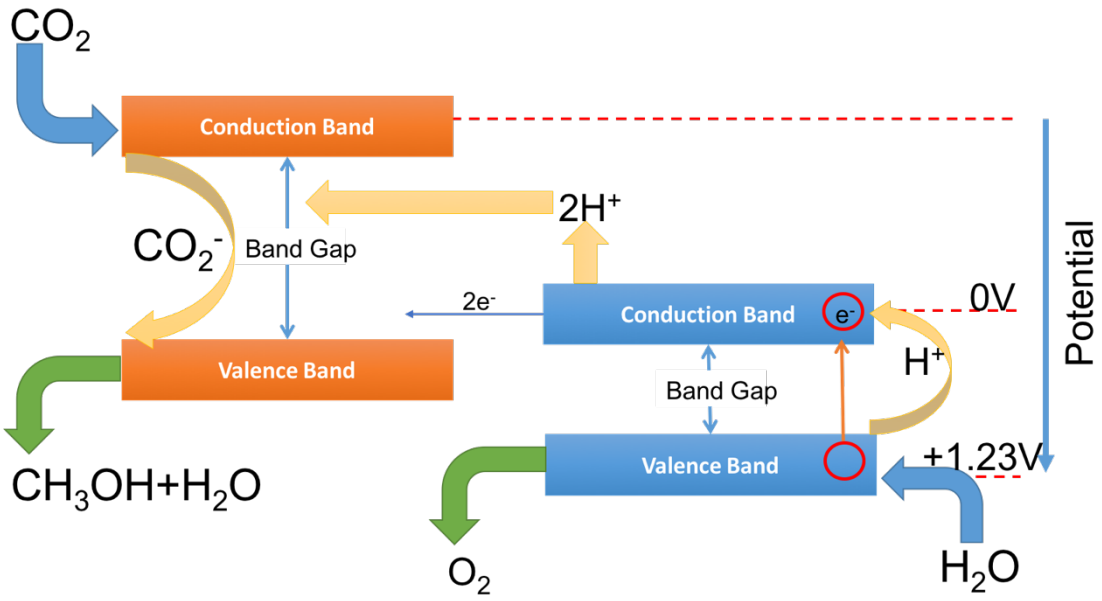


**Figure 1-5:** Schematic diagram of a photo-electrochemical carbon dioxide reduction mediated by photocatalytic water splitting.

### 1.1.4. Catalyst Requirements

As discussed before, photo electrochemical solar fuel systems offer a more straightforward energy conversion compared with conventional photovoltaic technology. This is partly because of the simplicity of the photo electrochemical device, which requires only a few elements to integrate the light-absorbing and electro-catalytic functions. In general, these systems require two electrodes and a membrane to separate the products, where the electrodes needs to absorb light in order to acts as catalyst for the reaction.

Although the simple device structure and operation of the photo electrochemical cells there are some constrains on the semiconductor material used as photo-catalyst. The most important constrain is related to the semiconductor bandgap, it is very important

that the energy obtained from photons generates the potential necessary for the reaction desired (at least 1.23 eV for water splitting).

In addition to the bandgap requirements for high conversion efficiency, the photo-electrodes must consist of widely available and low-cost component materials, be inexpensive to fabricate into their final form and — importantly — be robust enough to withstand continuous and long-term photo electrochemical operation in the presence of water and oxygen.

As occurred with technology for solar electricity production (photovoltaic cells), the photovoltaic technology mostly used at industrial scale is not based on the devices with the highest performance, as these are far too expensive, the challenge on the way to make economically sustainable photo electrochemical solar fuel production is to develop inexpensive semiconductor materials that can deliver high solar-to-fuel conversion efficiency with a direct semiconductor-liquid junction while operating stably on a timescale of years [14].

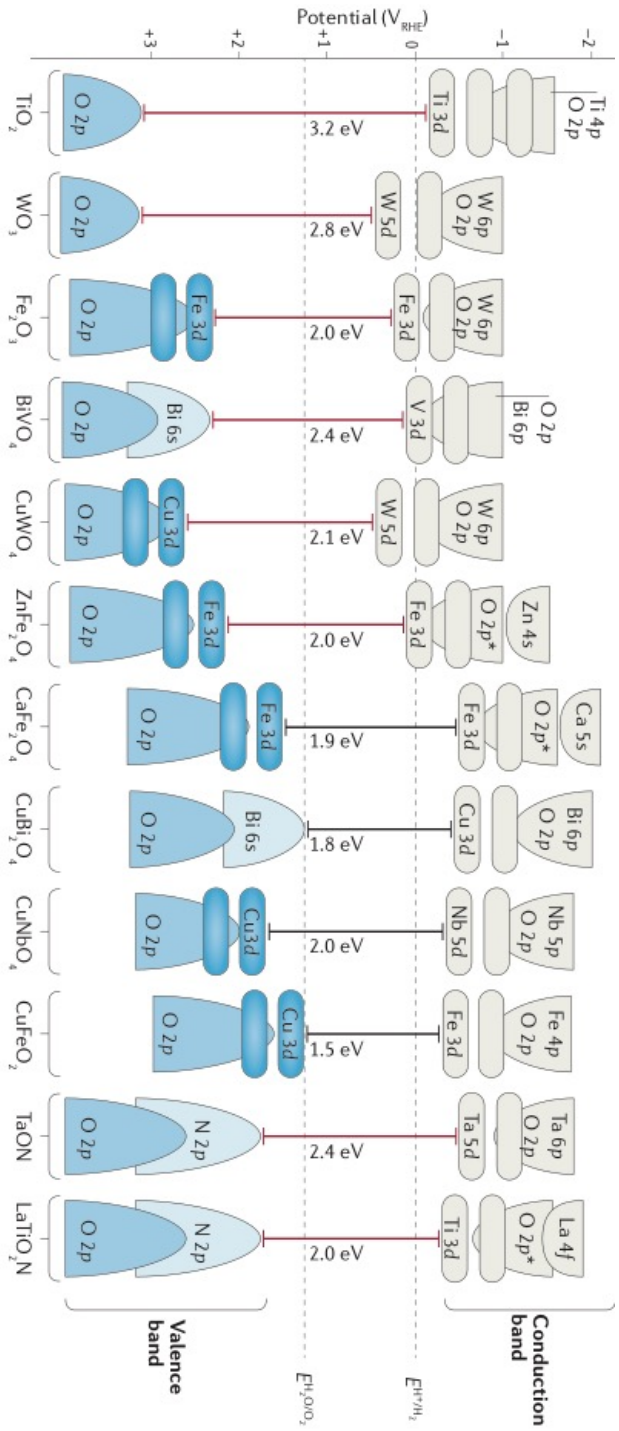


**Figure 1-6:** Band structure on selected materials, contribution of metal cation and oxygen anion states to the conduction and valence bands. The bandgap energy (red for n-type, black for p-type) is shown with respect to the reversible hydrogen electrode and the water redox energy levels (assuming Nernstian behavior for the band-edge

energies with respect to electrolyte pH). Reprinted by permission from Macmillan Publishers Ltd: Nature Reviews Materials (reference num. 14), copyright 2017.

## 1.2. Complex Oxides

The field of photo-electrochemical solar fuel production began with the observation [15, 16] of water photo-oxidation on semiconducting $TiO_2$. Semiconducting transition metal oxides are attractive photoanodes for water oxidation, as the relatively high electronegativity of oxygen results in the formation of stable compounds based on $O^{2-}$ anions. As photoanodes transfer photo- generated holes from their valence band to oxidize water, understanding and controlling the valence-band level is of interest.

The limitations of binary oxides have prompted focus to shift recently to ternary and more complex multinary oxides. With ~50 candidate metals in the periodic table, there are about 19,000 possible ternary metal oxides, and more than 220,000 quaternary oxides [17]. Clearly, a strategy is needed to identify promising candidates. Rationally engineering the bandgap in a ternary or multinary oxide through the judicious combination of metal cations is one possibility. Indeed, in many cases, the bandgaps of complex oxides can be predicted by a stoichiometrically weighted addition of the bandgaps of the parent binary oxides [18, 19].

### 1.2.1. Delafossite Type Oxides

A very promising class of materials is the family derived from Delafossite oxide. This oxide family structure was first reported and analyzed by Friedel in 1873 [20, 21] and named in honor of crystallographer G. Delafosse. Friedel found this material on caves walls placed in Yekaterinburg district, Rusia. Friedel described this structure as a natural copper iron oxide ($CuFeO_2$) grown under specific geothermal parameters.

Over hundred years after Friedel discovery, a Delafossite type material was found in 1976 in Guyana during an excavation, corresponding to the so called chromic cuprite ($CuCrO_2$) or McConnellite in honor to the geologist R.B. McConnell. After this founding, several variations of this structure were synthetized, creating a complete new material family like Delafossite that share crystalline structure but different lattice parameter. The properties of the Delafossite oxide will depend on the chemical element, stoichiometry and synthesis method used, so this allows a wide range of compounds that can be used in different research fields depending on its characteristics and expected use.

The Delafossite oxide family has a general chemical formula $AMO_2$ where A is a monovalent cation and M is a trivalent metal from Al to La [22], the main characteristic of this crystal structure is a linear coordination between the $A^+$ cation with $O^{2-}$ anions. So, the $O^{2-}$ , $A^+$ and $M^{+3}$ alignment, conform a pseudo tetrahedral structure, resulting in two basis crystallographic units: $MO_6$ octahedrons that share an edge between them, conforming horizontal layers and laminar structures O-A-O, resulting in a triangular pattern of $A^+$ ions [23].

These layers formed by $MO_6$ octahedrons and $A^+$ ions can be packed in two different ways, called Delafossite polytypes. The first one is conformed when the $MO_6$ structures present a gap between each other, in a way that a layer trough is in the same spatial position (1-2-1-2); so, the unit cell shows an $P6_3/mmc$ group symmetry (2H polytype). The other packing order is more complex, in this case the gap between the octahedral layers is such that every 3 layers the spatial position is the same (1-2-3-1-2-3); so, the unit cell shows an R3m group symmetry (3R Polytype), being the last one the most common [24].

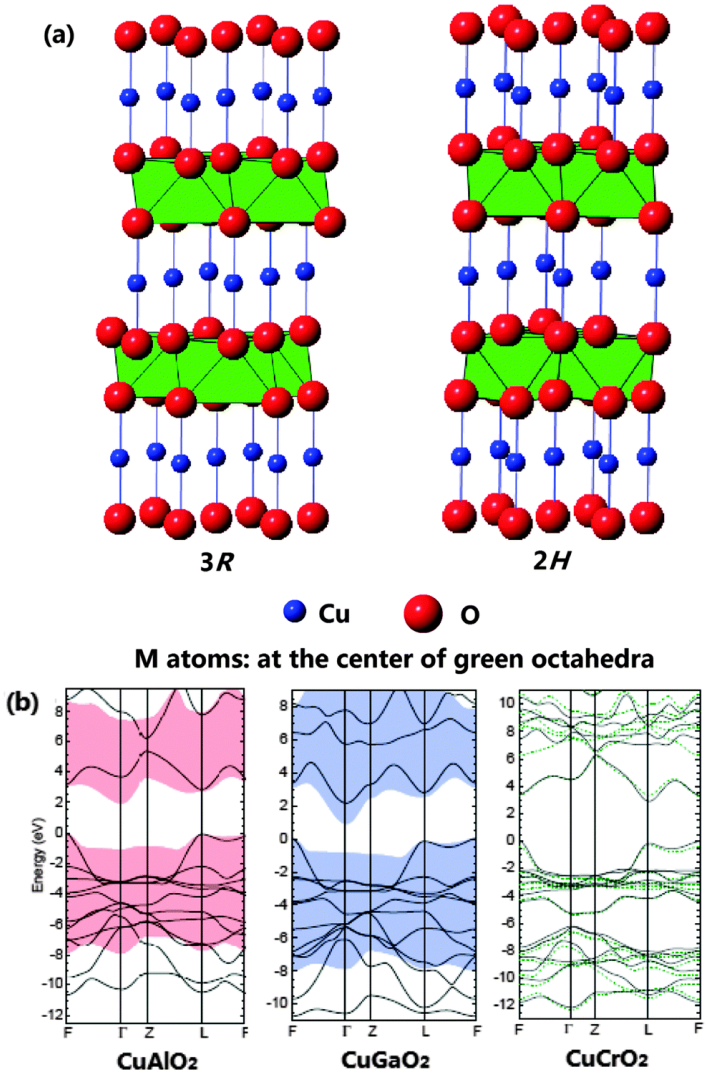


**Figure 1-7:** (a) The crystal structure of the Delafossite compounds. (b) The calculated band-structures of the CuMO2 compounds from the X-LDA method. Reproduced from Ref 24 with permission of the PCCP Owner Societies.

By varying their chemical composition (changing the M elements used) and the synthesis stoichiometry it is possible to form p-type or n-type semiconductors [25 - 28] and, as with more common semiconductor materials, the band gap(s) can be adjusted by changing the composition of the oxide, displaying a wide band gap semiconductor behavior, ranging between 1.1 eV and 3.6 eV. And, it is possible to change the mechanical properties, either structural or superficial, in the same way the optical properties change.

Copper-based ternary oxides (p-type) that crystallize in the Delafossite phase, $CuFeO_2$ [29, 30] and $CuRhO_2$ [31], have been recently investigated as potential photocathodes. Of these, $CuFeO_2$ is particularly attractive, as it is composed of widely available elements. Using a simple sol–gel route, the thickness of this material has been optimized, and an oxygen intercalation treatment can address the poor majority carrier conductivity, leading to sacrificial photocurrent densities of up to 1.5 mA $cm^{-2}$ at +0.35 VRHE ($O_2$ reduction). Photocurrent densities of up to 0.4 mA $cm^{-2}$ for $H^+$ reduction at 0 VRHE have been reported when added over layers for charge extraction and water reduction catalysts were used. The bare $CuFeO_2$ surface is a poor catalyst for water reduction but is active for $CO_2$ reduction. The bandgap of $CuFeO_2$ (1.5 eV) is lower than that of the parent binary oxide ($Cu_2O$) despite the valence and conduction bands being mostly Cu 3d in character in both cases (the Fe 3d bands lower the conduction band). Moreover, in stark contrast to $Cu_2O$, $CuFeO_2$ is remarkably stable under PEC operation in basic electrolytes, operating without a decrease in photocurrent for days, which makes it a highly promising photocathode material if the charge separation and catalytic activity can be further improved.

## 1.3. Objectives

Considering the positive results obtained with different copper Delafossite oxides as catalyst for photo electrochemical applications, in this work we will study the structural and adsorption properties of $CuFeO_2$ and $CuGaO_2$ Delafossite type oxides grown by Pulsed Laser deposition (PLD). Thermal desorption and x-ray photoelectron spectroscopy were used to obtain accurate information about chemical interaction between gas and catalyst surface, using this information in junction with structural characterization will give an idea if which properties have an incidence on absorption properties and samples behaviors as catalyst.

Delafossite thin films were deposited onto $Al_2O_3$ (001) substrates from a stoichiometric polycrystalline $CuFeO_2$ and $CuGaO_2$ target PLD technique. Due to technical issues, it was not possible to grow good epitaxial films of $CuGaO_2$ Delafossite oxide and $CuFe_{0.75}Ga_{0.25}O_2$ was grown and studied on its place.

### 1.3.1. Samples Description

In this work, we studied highly epitaxial thin films of $CuFeO_2$ and $CuFe_{0.75}Ga_{0.25}O_2$ Delafossite samples grown by pulsed laser deposition (PLD) by our collaborators at West Virginia University, United States of America.

The copper Delafossite thin films were deposited onto $Al_2O_3$ (001) substrates from a stoichiometric polycrystalline $CuFeO_2$ and $CuGaO_2$ target (Shangai Optics) using a Neocera PLD system with a KrF excimer laser (248 nm) from Coherent, Inc. Before deposition, the base pressure was $1 \cdot 10^{-8}$ Torr and $O_2$ gas was introduced into the chamber during the growth and controlled by mass flow. The distance between target and substrate was kept at 7.3 cm and the energy density at the target was approximately 2 J/cm$^2$. The pulse repetition rate was set to 2 Hz. The surface quality of the substrates and films was monitored using an in-situ Reflection High-Energy Electron Diffraction (RHEED) system from STAIB Instruments. Prior to each sample growth, the $Al_2O_3$ substrates were pre-cleaned and annealed at 1200 C for 2 h in air to obtain step-and-terrace surface quality, as verified by atomic force microscopy (AFM) using a Veeco Multimode microscope.

Delafossite $CuFeO_2$ and $CuFe_{0.75}Ga_{0.25}O_2$ thin films samples were grown under 0.1 mTorr of $O_2$ partial pressure and the substrate was heated to 600ºC. In order to make the multilayer structure, a buffer layer of 9 monolayers of $CuFeO_2$ was grown on top of the sapphire substrate. Then one monolayer of $CuGaO_2$ was deposited on top, followed by

three monolayers of $CuFeO_2$. This $CuGaO_2/CuFeO_2$ was repeated several times. Thus, the surface was terminated by $CuFeO_2$.

In Table 1-2 a brief description of samples used during this work is shown.

| Composition | Sample Code | Thickness (nm) | C lattice parameter (Å) |
|---|---|---|---|
| $CuFeO_2$ | CFO133 | 21 | 17.303±0.006 |
| | CFO163 | 25 | 17.404±0.015 |
| | CFO161 | 75 | 17.170±0.001 |
| | CFO168 | 100 | 17.148±0.002 |
| $CuFe_{0.75}Ga_{0.25}O_2$ | CFOCGO10 | 20 | 17.155±0.005 |
| | CFOCGO7 | 48 | 17.163±0.006 |
| | CFOCGO8 | 95 | 17.125±0.003 |

**Table 1-2:** Samples description, thickness and calculated c lattice parameter.

# Chapter 2: Experimental Setup

## 2.1. Samples Characterization.

### 2.1.1. X-Ray Diffraction (XRD).

A four-axis Rigaku x-ray diffraction (XRD) system with a Cu Kα rotating anode and Huber goniometers was used for structural characterization of the deposited films. $CuFeO_2$ and $CuFe_2O_4$ phases were identified using powder diffraction files # 01–075–2146 and #00–025-0283, respectively.

### 2.1.2. Raman Spectroscopy.

Raman spectra were obtained with a LabRam010 system from Instruments, S.A. (Horiba) using a 5.5 mW He–Ne laser (632.8 nm wave- length). This instrument uses an Olympus confocal optical microscope with a light spectrometer in a back-scattering geometry, where the incident beam is linearly polarized and spectral detection is unpolarized. The spectra were taken at room temperature using a 100x objective (~10μm spot size) and with an energy resolution of approximately 1 $cm^{-1}$.

### 2.1.3. X-ray Photoelectron Spectroscopy (XPS).

The surface chemical information was obtained by X-ray Photoelectron Spectroscopy (XPS). Measurements were performed with a STAIB RQ300X x-ray source using Mg Kα and Al Kα x-radiation and a STAIB DESA100 electron spectrometer as detector, which was operated in a constant pass energy mode at 225 V. The working pressure in the analysis chamber was typically lower than $10^{-8}$ Torr. The binding energy scale was calibrated by measuring the C 1 s peak at 284.8 eV. The composition and chemical state

were investigated based on the areas and binding energies of O 1s, C 1s, Fe 2p and Cu 2p photoelectron peaks and Cu (L3VV) Auger peaks. Data analysis was performed by a fitting program using properly mixed Lorentzian–Gaussian functions after background subtraction according to the Shirley method. Surface atomic compositions were determined using standard XPS cross sections.

### 2.1.4. Optical Transmittance and Difuse Reflectance.

Transmittance and reflectance spectroscopies were recorded for the sample post surface heat treatment. Both spectra were recorded over wavelength range 350–1100 nm corresponding to photon energies 1.12–3.5 eV. A tungsten halogen lamp provides the broadband light source. The beam is chopped before entering the monochromator, and the signals are measured using lock-in amplifiers. The monochromator (Triax 180, Jobin Yvon-Horiba) is equipped with a 1200 g/mm blazed ruled grating and set up to provide a1 nm full width at half maximum.

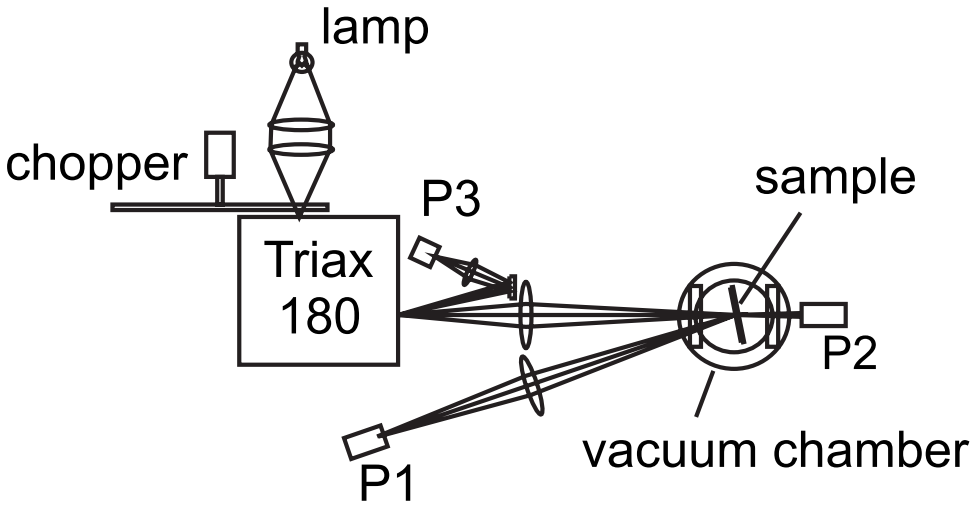


**Figure 2-1**: Experimental transmittance and reflectance spectroscopy system. The incidence angle is 8°. P1, P2, and P3 stand for the silicon photodiodes. Photodiode P3 monitors the incident intensity to normalize the reflected and transmitted signals measured by P1 and P2 in case of lamp intensity variations. The chopper frequency is around 960 Hz. The wavelength range 400–900 nm is limited by the tungsten halogen lamp spectrum and second order diffraction in the monochromator [32].

## 2.2. Gas Absorption properties.

### 2.2.1. Thermal Programmed Desorption (TPD) Vacuum System

To perform the thermal program desorption (TPD) measurements in this work, we used a high vacuum system composed by a stainless-steel chamber which was custom made by MDC Vacuum Inc. of approximately $4 \times 10^{-2}$ $m^3$, pumped by an Adixen 0.15 $m^3/s$ Turbo pump (ATP150), backed by an Adixen 20.7 $m^3/h$ dual stage rotatory pump (Pascal 2021C1). Using this configuration, it was possible to perform the TPD experiments under pressures lower than $10^{-8}$ Torr to be able to detect desorbed gases. Partial pressures and total pressure were measured by a mass spectrometer (RGA 200) from Stanford Research Systems.

Another important condition for TPD experiments is how much clean the surface of the sample is. Normal contaminations from the air like water, carbon and oxygen are usually adsorbed on the samples, so when a TPD experiment is performed these contaminations are desorbed incrementing the background pressure, which decrease the sensibility in the measurement of desorbed gases. To ensure a proper surface condition, the samples were underwent to a fast heating and sputtered with $Ar^+$ ions using an ion source (IQE 11/35) from Specs. Then samples were characterized by X-ray Photoelectron Spectroscopy (XPS) using a STAIB RQ300X X-ray source using Mg Kα x-radiation and a STAIB DESA100 electron spectrometer as detector.

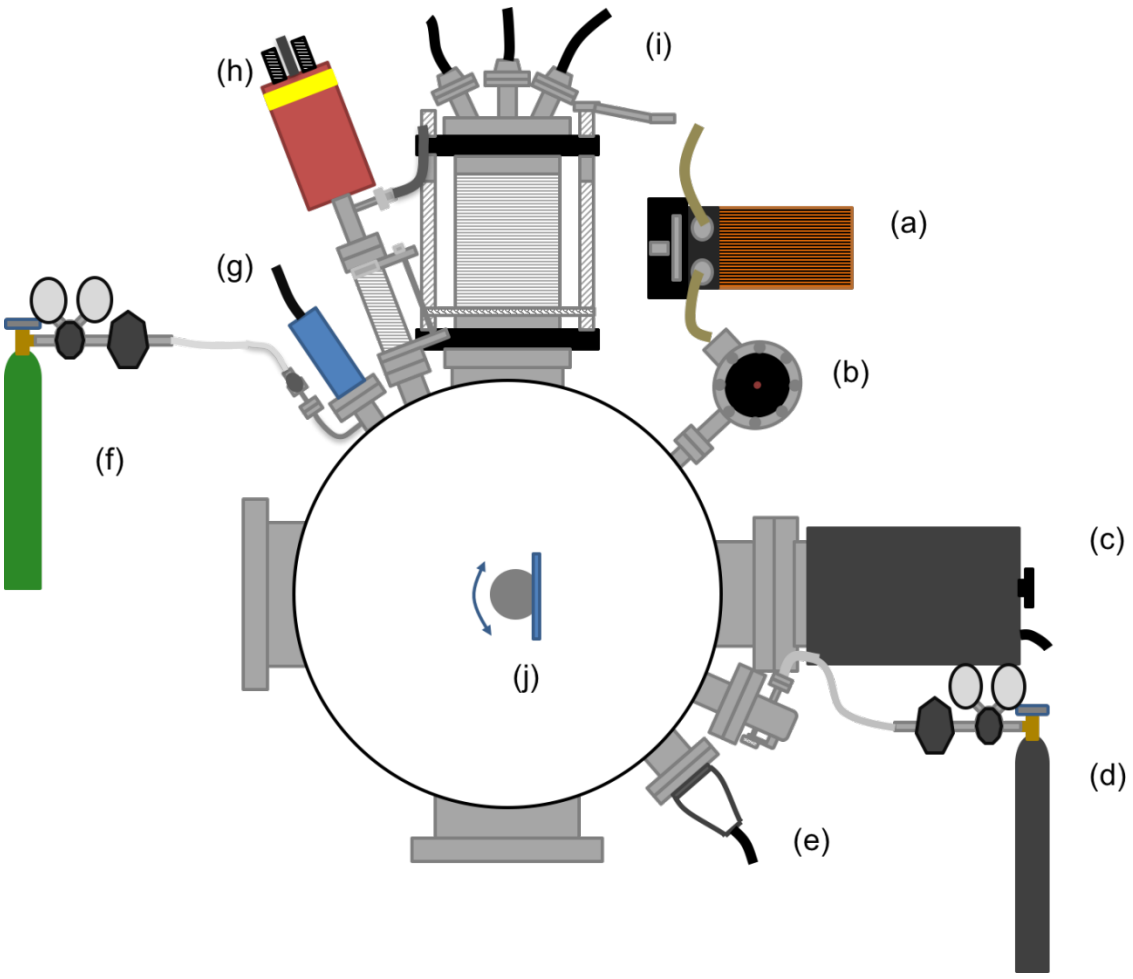


**Figure 2-2:** Scheme of the vacuum system used for the TPD experiments. (a) Mechanical pump. (b) Adixen ATP150 Turbo pump. (c) Mass spectrometer RGA 200, Stanford Research Systems. (d) $CO_2$ high pressure tank. (e) Hot cathode gauge. (f) Ar high pressure tank. (g) Ar+ Sputtering Ion Source IQE 11/35, Specs. (h) STAIB RQ300X X-ray. (i) Auger spectrometer DESA 100, STAIB Instruments. (j) Sample holder.

When the background pressure and the surface cleaning were optimized, TPD experiments were performed. First, the samples were exposed to 1500 L and 5000 L (1 L=$10^{-6}$ torr s) of $CO_2$ gas from INDURA (99 % of purity) through a leak valve, always at room temperature. Then, the samples were heated using a home-made manipulator integrated with a Eurotherm 2404 temperature controller. Using a method in where a constant power was applied to the samples, linear ramps from 300 K to approximately 1000K were obtained with temperature rates in the range of 10 K/s to 30 K/s. Finally,

the monitoring of the pressures was performed with a quadrupole mass spectrometer RGA 200 from Stanford Research Systems. Temperature and pressure measurements were performed simultaneously using a Laview software as function of time.

The home-made manipulator used in the TPD experiments, which is shown in the Figure 2-3, is composed of a ceramic support in where two Copper rigid bars are fixed. On this bars a stainless-steel foil was directly bolted and in the surface of the foil a thermocouple was spot welded, to measure the temperature during the desorption process. The Delafossite samples were hold on the stainless-steel foil by to stainless steel wires used as tweezers.

From outside the vacuum chamber, the manipulator has two copper feedthroughs in where the temperature controller was connected, so the current flows directly through the samples with a constant power. Also from outside, the system has a 6 pins feedthrough where two of them were used for the thermocouple so using an analog devices model 6BP0 controlled by a Labview software for temperature monitoring during the TPD. The manipulator allows two degrees of freedom for the samples, as are show in the figure; a rotation of 360° and a height movement in a range of 2.54 cm during the experiments.

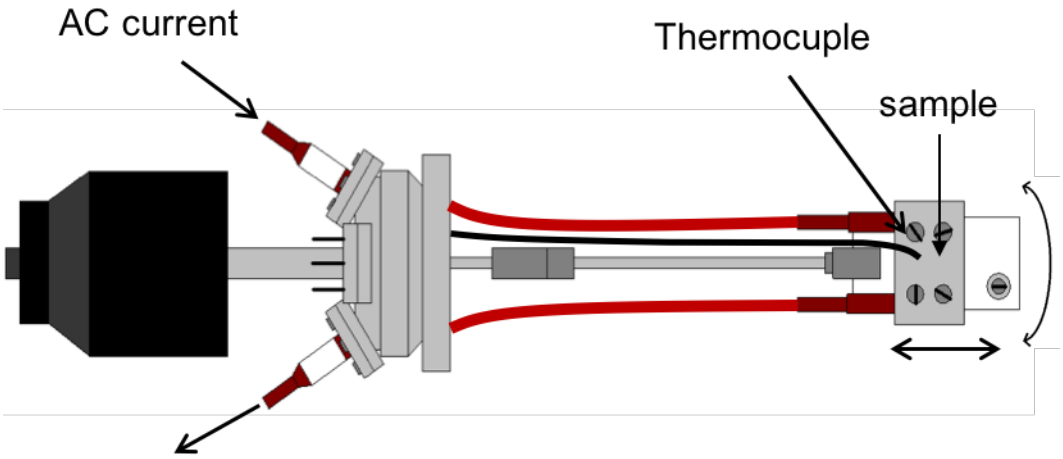


**Figure 2-3:** Home-made sample holder schematic

# Chapter 3: Results and Discussion

## 3.1. Characterization.

### 3.1.1. X-Ray Difraction (XRD)

Using X-ray diffraction structural characterization was performed for $CuFeO_2$ and $CuFe_{0.75}Ga_{0.25}O_2$ samples. In Figure 3-1 XRD patterns for two $CuFeO_2$ samples are shown, in this figure it is possible to observe well defined peaks, each of them correspond to different crystal planes along the c-axis of a rhombohedral Delafossite type structure, as the main peaks showed are (003), (006), (009), (0012) and (0015) plane directions this confirm that a highly epitaxial thin film oriented in the (001) direction was achieved during the growth, from the pattern it is possible to determine the c lattice constant of 1.728 nm [33]. It is also possible to observe peaks attributed to the $Al_2O_3$ (001) substrate corresponding to different crystalline planes along the c-axis corresponding to (003), (006) and (009) planar directions respectively. From Figure 3-1 is also possible to observe a change between relative intensities of peaks related to the $CuFeO_2$ composite versus the substrate related peaks, for $CuFeO_2$ 75 nm thickness we observe a decrease of relative intensity of peaks attributed to $Al_2O_3$, meanwhile in the 21 nm sample these peaks showed more intensity. This situation is easily explained by the increase of the $CuFeO_2$ thickness making more difficult to detect the substrate peaks.

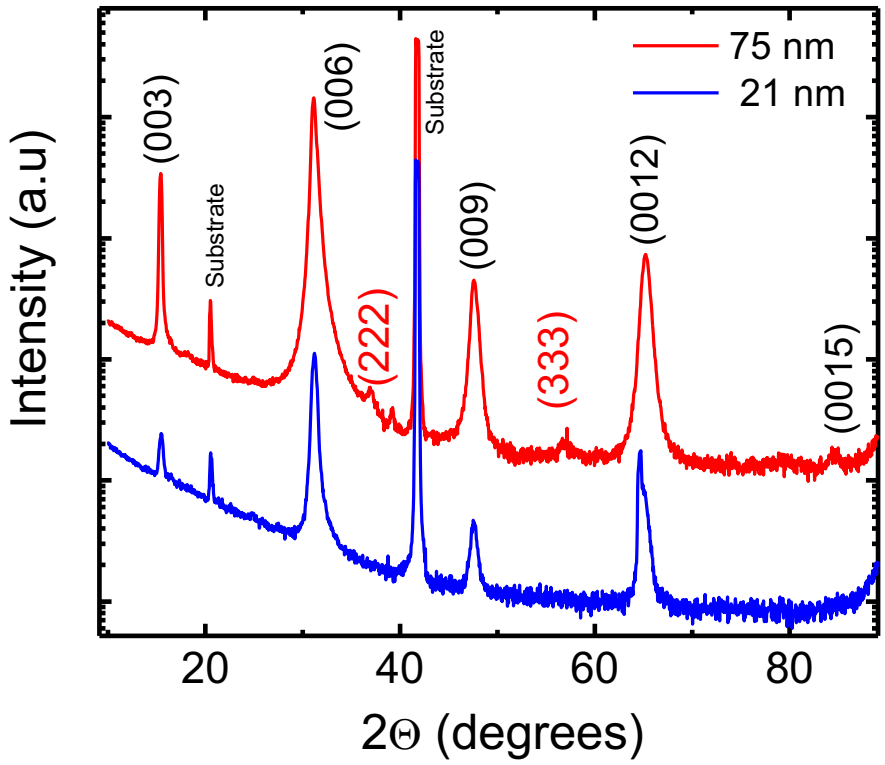


**Figure 3-1:** X-ray diffraction pattern for $CuFeO_2$ samples of 75 nm (red line, CFO161) and 21 nm (blue line, CFO133), black labeled peaks correspond to $CuFeO_2$ peaks and red labeled peaks correspond to $CuFe_2O_4$ spinel material.

Also in Figure 3-1 there is some evidence of $CuFe_2O_4$ spinel formation in the 75 nm thickness sample, where small peaks related to (222) and (333) plane orientation begin to be visible. These implies that while thicker is the sample there are more defects present on the sample.

Exact peak center position for all $CuFeO_2$ samples and $CuFeO_2$ reference pattern #01-085-0605 are shown in Table 4-1 of Appendix A.1.

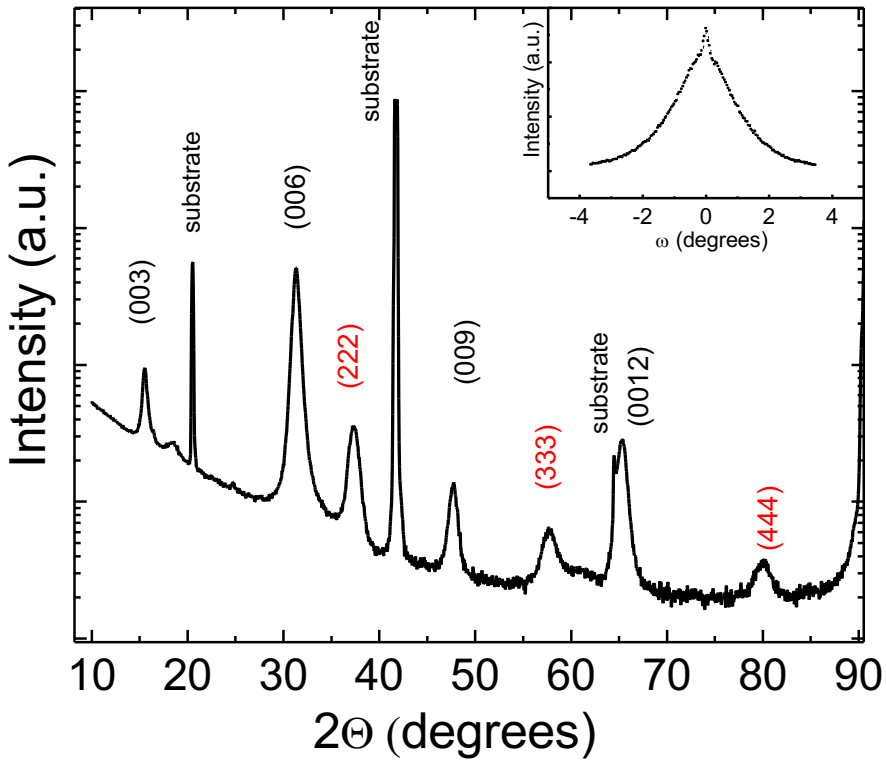


**Figure 3-2:** XRD patter of $CuFe_{0.75}Ga_{0.25}O_2$ 48 nm thick sample (CFOCGO7), black labeled peaks correspond to $CuFeO_2$ peaks and red labeled peaks correspond to $CuFe_2O_4$ spinel material. In the inset is the rocking curve of the (006) peak.

The same measurement was performed for the $CuFe_{0.75}Ga_{0.25}O_2$ samples, where pattern for the 48 nm sample (CFOCGO7) is shown in Figure 3-2. The main peaks shown in this pattern are related to the epitaxial growth of the sample on (001) direction, (003), (006), (009) and (0012) peaks labeled in black, in this case the c lattice constant was estimated of 1.7095 nm, smaller than for pure $CuFeO_2$ film. Peaks related to spinel formation (222), (333) and (444) labeled in red gain more importance in this kind of sample than in pure $CuFeO_2$ samples, the increased presence of this spinel material on the sample is attributed to defects on the junction between $CuFeO_2$ and $CuGaO_2$ Delafossite materials during the growth. XRD pattern for all $CuFe_{0.75}Ga_{0.25}O_2$ samples were also measured, peak center information of samples, $CuFeO_2$ reference and $CuGaO_2$ reference are shown in Table 4-2 in Appendix A.1.

The inset plot in Figure 3-2 shows the rocking curve of (006) peak, this plot shows a single peak structure and not a sum of two peaks (shoulder) as it will be expected for a multi lattice structure of two different compounds, this single peak structure is more related to a single material but as we know that this sample was made from two different materials ($CuFeO_2$ and $CuGaO_2$) this single peak structure of the rocking curve give us a an idea of an inhomogeneous alloy between these two materials more than a multi lattice as it was intended.

This non-homogeneous alloyed structure may give a good explanation of the increased presence of spinel peaks in the diffraction pattern, as these peaks related to defects on the film, the junction between $CuFeO_2$ and $CuGaO_2$ may generate such defects due to mismatching between them.

| | **Repetitions** | **Composite** | **Density ($g/cm^3$)** | **Thickness (nm)** | **Roughness (nm)** |
|---|---|---|---|---|---|
| Core | 21 | $CuFeO_2$ | 5.51 | 1.29 | 1.2 |
| | | $CuGaO_2$ | 6.25 | 0.296 | 0.916 |
| Buffer | 1 | $CuFeO_2$ | 5.51 | 3.34 | 0.288 |

**Table 3-1:** parameters used for fitting GID pattern according to a multi lattice approach for $CuFe_{0.75}Ga_{0.25}O_2$ sample.

For getting more information about the surface structure of this film, a grazing incidence diffraction pattern was measured and fitted according to two different models, first it was fitted using the initial idea about the sample *i.e.* the multi lattice structure and then using the alloy approach.

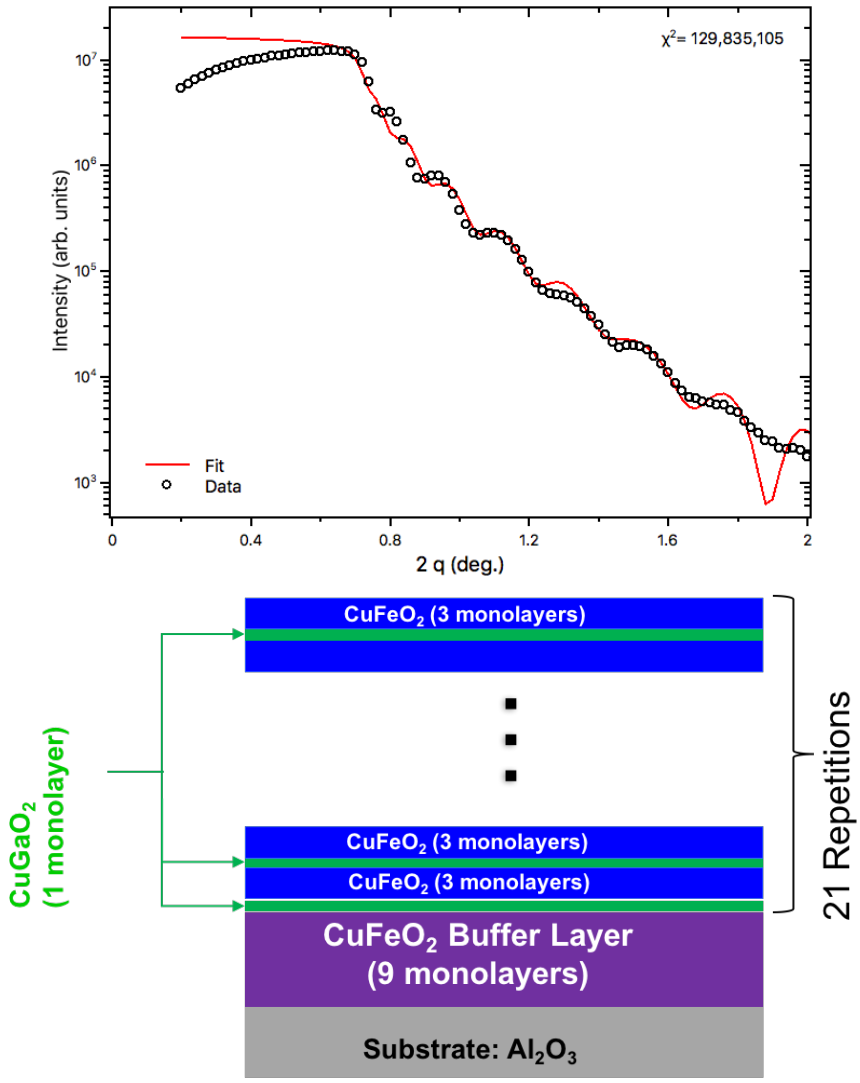


**Figure 3-3:** GID diffraction pattern for $CuFe_{0.75}Ga_{0.25}O_2$ 48 nm thickness (CFOCGO7) with fit considering the multi lattice model (top) and schematic diagram of the multi lattice structure of the sample.

In Figure 3-3 (top) the GID spectra for the $CuFe_{0.75}Ga_{0.25}O_2$ 48 nm thick is shown with a fit that considered the sample as a multi lattice structure as shown in the diagram in Figure 3-3 bottom considering parameters in Table 3-1 for fitting. Unless this model fit quite well with the data obtained but in the first two peaks the model doesn't fit

completely and as this peaks are sensitive to surface properties it suggests that the multi lattice approach is not the best for our data.

| | Composite | Density ($g/cm^3$) | Thickness (nm) | Roughness (nm) |
|---|---|---|---|---|
| Alloy | $CuFe_{0.75}Ga_{0.25}O_2$ | 5.695 | 22.6 | 1.24 |
| Buffer | $CuFeO_2$ | 5.51 | 7.19 | 1.86 |

**Table 3-2:** Parameters used for GID pattern fitting according to alloyed structure approach for $CuFe_{0.75}Ga_{0.25}O_2$ sample.

If we consider a model where the two compounds form a relatively homogeneous alloy with 75% of $CuFeO_2$ and 25% of $CuGaO_2$ for density calculation, parameters shown in Table 3-2 can be used for the GID fitting, obtaining fitting of Figure 3-4. As it is possible to see from the plot the model has better adjustment to the first peaks and lower $\chi^2$ value than multi lattice approach in this range, this situation let us think that the alloy approach is closer to the real structure of the sample as expected from results of XRD.

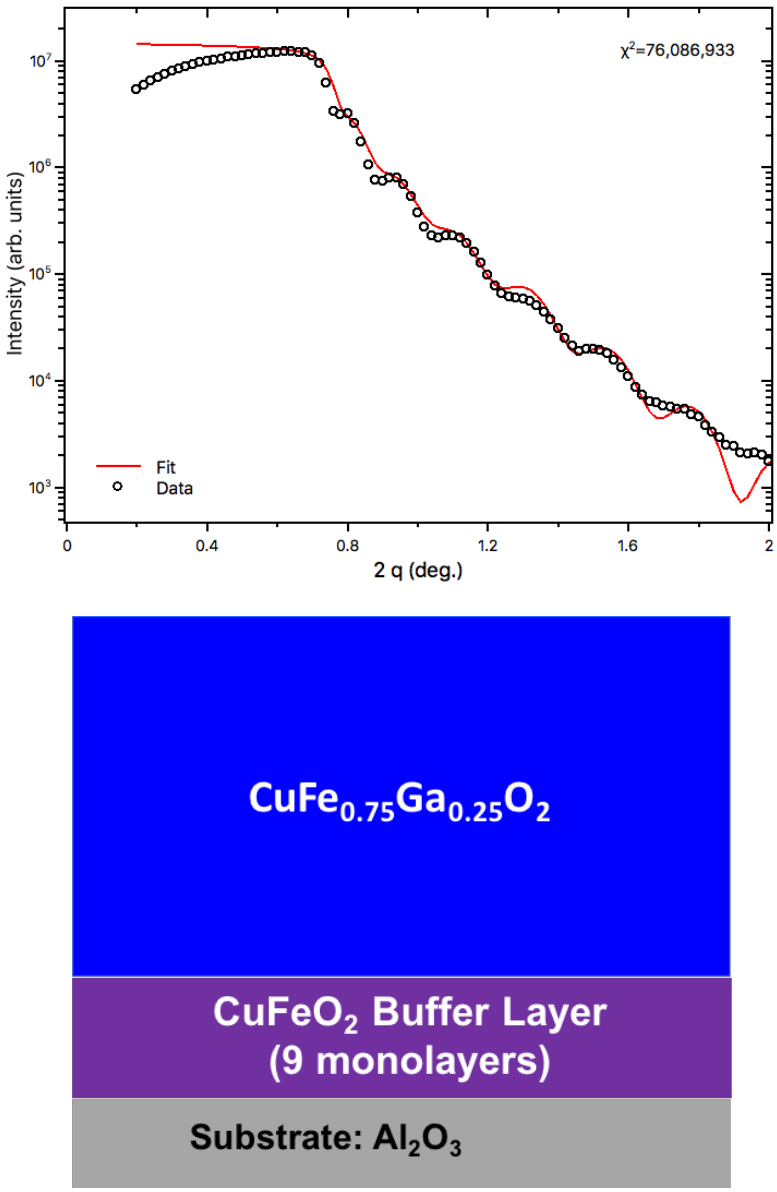


**Figure 3-4:** GID diffraction pattern for $CuFe_{0.75}Ga_{0.25}O_2$ 48 nm thickness (CFOCGO7) with fit considering the alloy model (top) and schematic diagram of the alloyed structure of the sample.

### 3.1.2. Raman Spectroscopy

Raman spectroscopy was used in order to confirm the quality of the samples, in Figure 3-5 Raman spectra of $CuFeO_2$ and $CuFe_{0.75}Ga_{0.25}O_2$ samples are shown. Black line data

in Figure 3-5 shows the spectra for $CuFeO_2$ 75 nm thick sample, in this spectrum three main peaks are shown at 351.23±0.28, 506.26±0.37, and 686.37±0.14 $cm^{-1}$ [33] whose positions and relative magnitudes were consistent with other reported $CuFeO_2$ materials [34 - 36]. In this case, the vibrational mode at 350 $cm^{-1}$ is attributed to the $E_g$ mode along the c axis of the octahedral structure. The peak located at 689 $cm^{-1}$ is attributed to the $A_{1g}$ vibrational mode along a perpendicular plane to the c axis. The peak found at 511 $cm^{-1}$ was attributed to non-zero wave vector phonons typical of crystalline defects in this structure [35].

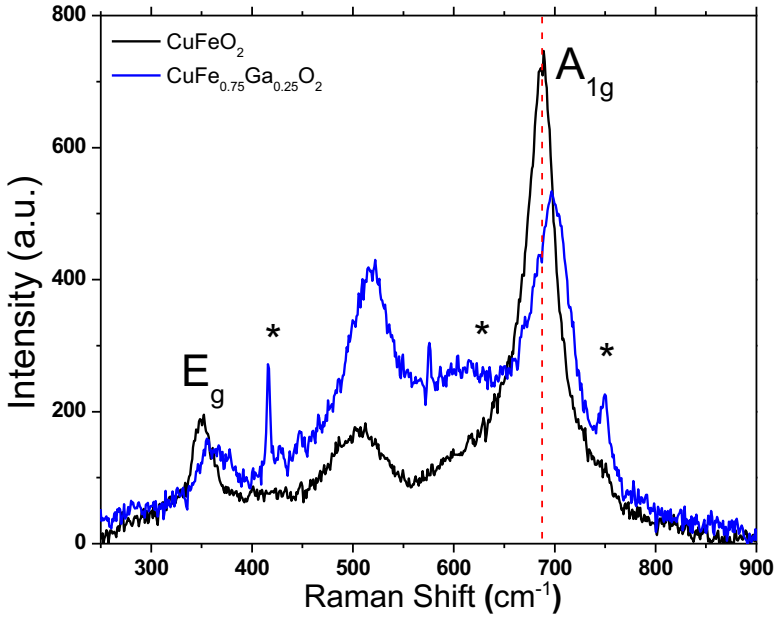


**Figure 3-5:** Raman spectra of (black) $CuFeO_2$ 75 nm thickness (CFO161) and (blue) $CuFe_{0.75}Ga_{0.25}O_2$ 48 nm thickness (CFOCGO7).

Blue line data in Figure 3-5 shows Raman spectrum of $CuFe_{0.75}Ga_{0.25}O_2$ 48 nm thick sample, the peaks seen in this case at 360.37±0.62, 516.31±0.25, and 697.94±0.30 $cm^{-1}$ correspond to the same modes but shifted 9 $cm^{-1}$ due to the inclusion of gallium in the solid solution. A pure $CuGaO_2$ sample shows Raman peaks at 368 and 729 $cm^{-1}$ [36]. If

the Raman peaks shift to higher values linearly with gallium content, we can determine that the gallium is at ~25 at % in the solution.

In Table 3-3 peak center positions for $E_g$ and $A_{1g}$ modes are shown, these peak centers were obtained by fitting each peak to a lorentzian peak and $R^2$ value is also showed for each peak. Results in this table shows that all $CuFeO_2$ samples showed Raman modes at same energies and in good agreement with references. A different situation occurs for $CuFe_{0.75}Ga_{0.25}O_2$ samples, in this case there is more dispersion in peak centers.

| Composition | Code | $E_g$ | | $A_{1g}$ | |
|---|---|---|---|---|---|
| | | $X_c$ ($cm^{-1}$) | $R^2$ | $X_c$ ($cm^{-1}$) | $R^2$ |
| $CuFeO_2$ | CFO133 | 355.42±0.88 | 0.76 | 685.78±0.37 | 0.96 |
| | CFO163 | 355.42±0.88 | 0.71 | 685.20±0.34 | 0.95 |
| | CFO161 | 351.23±0.28 | 0.94 | 686.37±0.14 | 0.99 |
| | CFO168 | 351.23±0.27 | 0.91 | 690.25±0.15 | 0.99 |
| $CuFe_{0.75}Ga_{0.25}O_2$ | CFOCGO10 | 363.64±0.96 | 0.69 | 699.80±0.35 | 0.95 |
| | CFOCGO7 | 360.37±0.62 | 0.84 | 697.94±0.30 | 0.96 |
| | CFOCGO8 | 351.96±0.69 | 0.56 | 689.94±0.22 | 0.97 |

**Table 3-3:** Summary of $E_g$ and $A_{1g}$ Raman peak position for al samples.

If we consider $CuFe_{0.75}Ga_{0.25}O_2$ samples as multilattice, the resulting Raman spectrum should be an addition of both composites spectrum, *i.e.* 0.75 $CuFeO_2$ and 0.25 $CuGaO_2$ in intensity. In Figure 3-6 (a), a simulation of the resulting spectrum using reference data for both Delafossite composites is showed, from this figure is easy to distinguish between $A_{1g}$ Raman modes coming from each Delafossite composite. Then in Figure 3-6 (b) the comparison between calculated and obtained (experimentally) spectra is shown, from this figure is possible to see that experimental Raman spectrum does not show any clear contribution from $CuGaO_2$ composite, meanwhile what is really observed is a

single peak at different Raman shift position. Similar behavior is observed for other $CuFe_{0.75}Ga_{0.25}O_2$ samples showed in Figure 4-10 and Figure 4-11 of Appendix A.2.

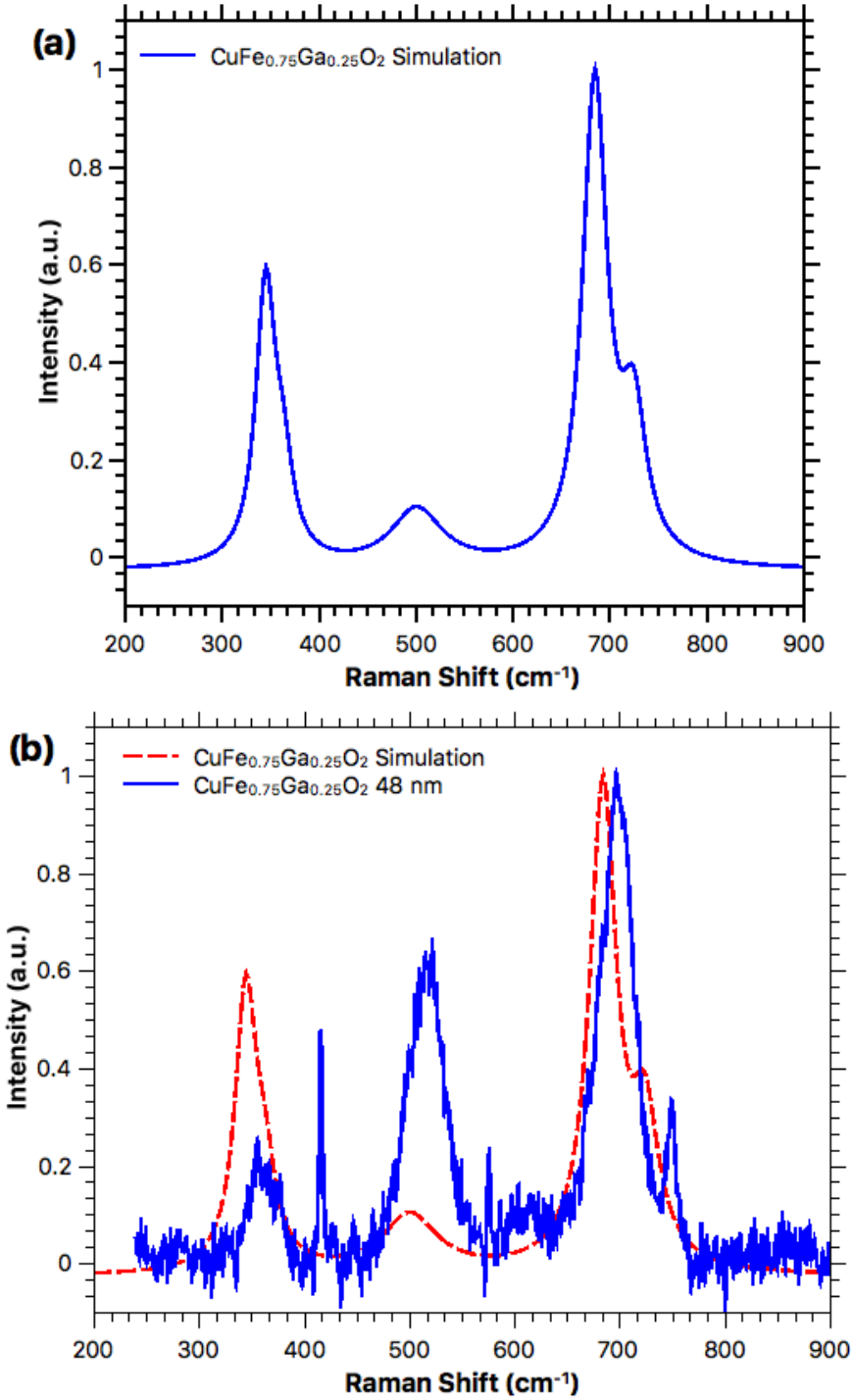


**Figure 3-6: (a)** Simulated Raman spectrum of $CuFe_{0.75}Ga_{0.25}O_2$. (b) comparison between $CuFe_{0.75}Ga_{0.25}O_2$ simulated Raman spectrum and experimentally obtained Raman spectrum from 48 nm thickness sample (CFOCGO7).

As it can be seen from Figure 4-9 of Appendix A.2 peak center position of $A_{1g}$ Raman mode is not showed in the same position for all samples, this situation indicates that the vibrational modes are not equally modified in all cases unless all samples were constructed in a 75% $CuFeO_2$ and 25% $CuGaO_2$. Therefore, Raman spectroscopy also confirms the alloyed structure assumed in previous analysis with the observation of a non-homogeneous structure.

### 3.1.3. X-Ray Photoelectron Spectroscopy (XPS)

Surface chemical composition was determined for both kind of samples using XPS, in Figure 3-7 (a) survey spectrum acquired using an Al Kα anode is shown, in this plot main peaks are labeled showing that the surface is mainly composed by copper, iron, oxygen and carbon. Carbon presence is attributed to surface contamination due to air exposure. While for confirming the Delafossite chemical composition, i.e. $Cu^{+1}$ and $Fe^{+2}$, high resolution scans of Cu 2p and Fe 2p bands were performed.

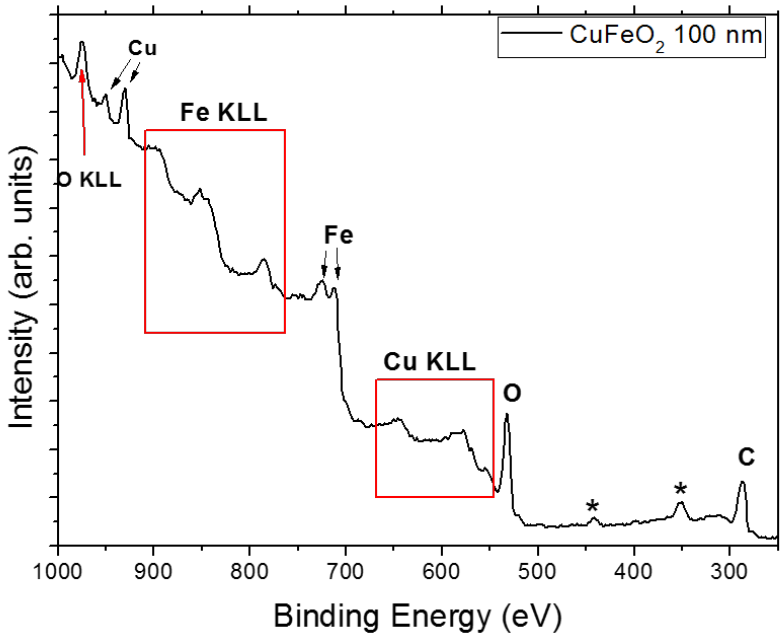


**Figure 3-7:** X-ray Photoelectron survey spectrum of $CuFeO_2$ 100 nm thickness (CFO168) sample with principal peaks identified, peaks labeled with * correspond to sample holder peaks.

A high resolution scan of Cu 2p is shown in Figure 3-8 (a), in this case peak fitting was performed considering 4 different copper species, metallic copper ($Cu^{0}$), copper oxides ($Cu^{+1}$ and $Cu^{+2}$) and copper hydroxides and carboxylates ($Cu(OH)_2$ and $CuCO_3$). Depending on the oxidation state of copper the Cu $2p^{3/2}$ peak will be shifted allowing to differentiate these three copper species, in the case of $Cu(OH)_2$ and $CuCO_3$ the situation is not that favorable because both compounds shows the same binding energy for Cu 2p 3/2 [37 - 39]. Using this information for peak fitting we can realize that surface sample is mainly composed of $Cu^{+1}$ oxide as expected for Delafossite structure, other compounds such as $Cu(OH)_2$ and $CuCO_3$ were also observed, but in this case, is attributable to surface contamination due to air exposure.

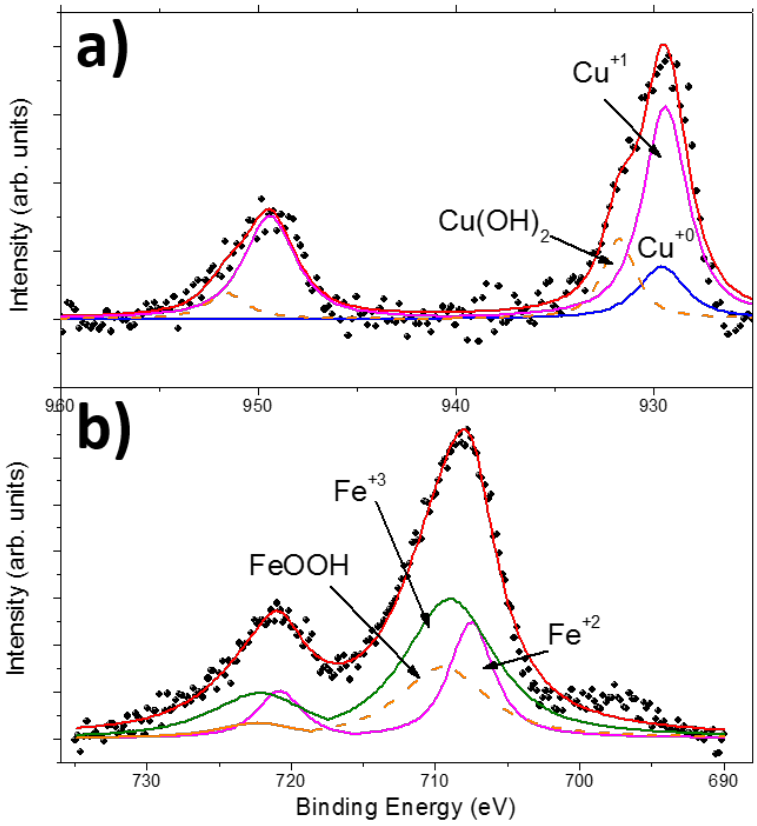


**Figure 3-8:** XPS High resolution scans for (a) Cu 2p and (b) Fe 2p peaks for $CuFeO_2$ film 100 nm in thickness (CFO168) and peak fitting considering different oxidation states.

The same method was used to perform the peak fitting of the Fe 2p peak showed in Figure 3-8 (b), in this case the fitting showed that most iron was found in $Fe^{+3}$ oxide as expected for $CuFeO_2$ Delafossite oxide [40], other compound such as FeOOH were found in the fitting and are attributable to surface contamination, like in copper case [41 - 43].

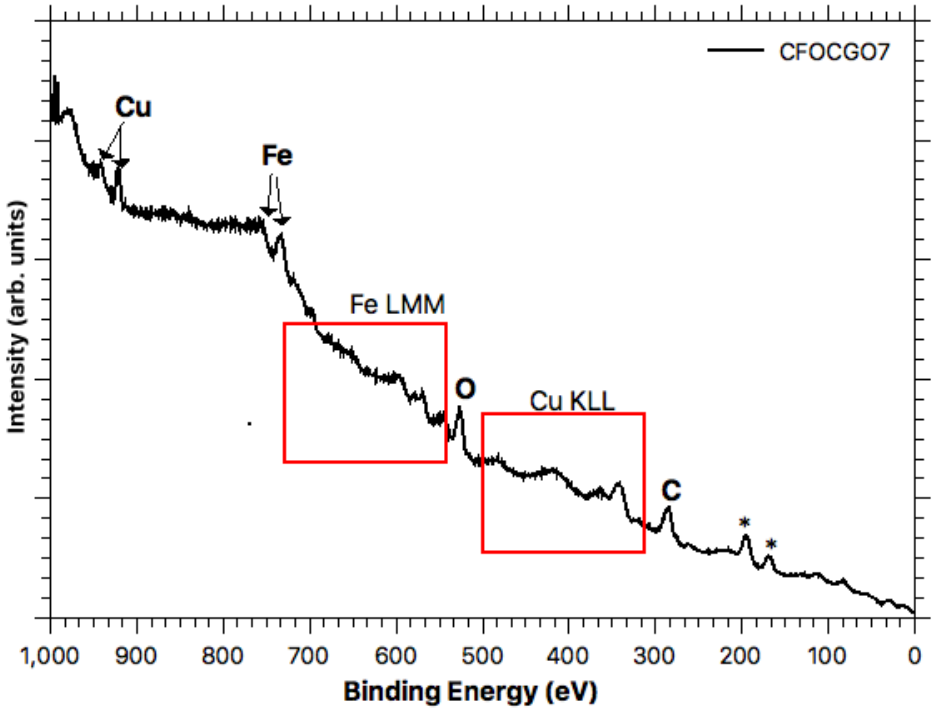


**Figure 3-9:** X-ray Photoelectron survey spectrum of $CuFe_{0.75}Ga_{0.25}O_2$ 48 nm thickness (CFOCGO7) sample with principal peaks identified, peaks labeled with * correspond to sample holder peaks.

XPS measurements were also performed for $CuFe_{0.75}Ga_{0.25}O_2$ samples using Mg Kα X-radiation, survey spectrum and high resolution spectra for Fe 2p and Cu 2p are sowed in Figure 3-9 and Figure 3-10. In this case gallium peaks were not observed in the survey scan (Ga 3d should be at 20 eV and Ga 2p at 100 eV in Binding Energy) and consequently high resolution scan of this composite was not recorded. Fitting of Cu 2p and Fe 2p peaks was performed using the same parameters used in $CuFeO_2$ film peaks

fitting, results obtained revealed that high presence of $Cu^{+1}$ and $Fe^{+2}$ oxides confirming the Delafossite structure [37 – 43].

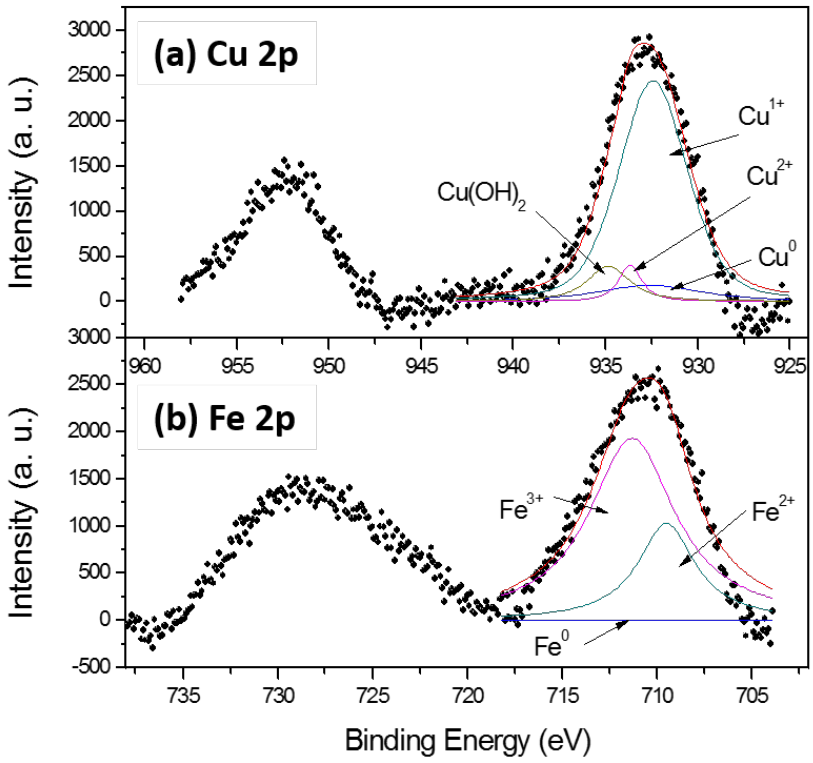


**Figure 3-10:** XPS High resolution scans for (a) Cu 2p and (b) Fe 2p peaks for $CuFe_{0.75}Ga_{0.25}O_2$ film 48 nm in thickness (CFOCGO7) and peak fitting considering different oxidation states.

XPS spectrum of other samples were also recorded and all results are showed in Appendix A.3.

Most of the information showed in this section intended to confirm and know the structure and surface properties of the stack of samples used for this study, as it was the idea all samples have a Delafossite type structure and were epitaxial grown over $Al_2O_3$ substrate, including the $CuFeO_2/CuGaO_2$ mixed samples. Although the original idea with these samples was to get a super lattice structure what we finally got was a $CuFeO_2$ film doped with $CuGaO_2$ forming a quite non homogeneous alloy within the two

compounds, this alloy structure generates a change on some properties as it can be observed from the Raman spectrum showed in Figure 3-5 the addition of $CuGaO_2$ into the $CuFeO_2$ lattice generated a shifting of the phonons energy.

### 3.1.4. Optical Transmittance and Diffuse reflectance

Transmittance and diffuse reflectance in the near infrared and visible spectra were also measured for investigating how changed the optical properties due to the addition of gallium into the lattice. In Figure 3-11 (a) transmittance spectra are shown for 3 different samples, $CuFeO_2$ 20 nm (CFO133) and 75 nm (CFO161) thickness and $CuFe_{0.75}Ga_{0.25}O_2$ 48 nm (CFOCGO7) thickness. From figure is possible to observe a clear difference between $CuFe_{0.75}Ga_{0.25}O_2$ spectrum and the $CuFeO_2$ ones, this situation gives a glimpse of changes on the optical properties due to gallium addition into the lattice. On the other hand, from the same plot we can see that the two spectra of $CuFeO_2$ samples are slightly different, but in this case these differences are attributable to defects presence on the lattice.

When looking at diffuse reflectance spectra showed in Figure 3-11 (b) there is also an observable difference between the two kinds of samples, unless this difference is not as important as in the transmittance spectra.

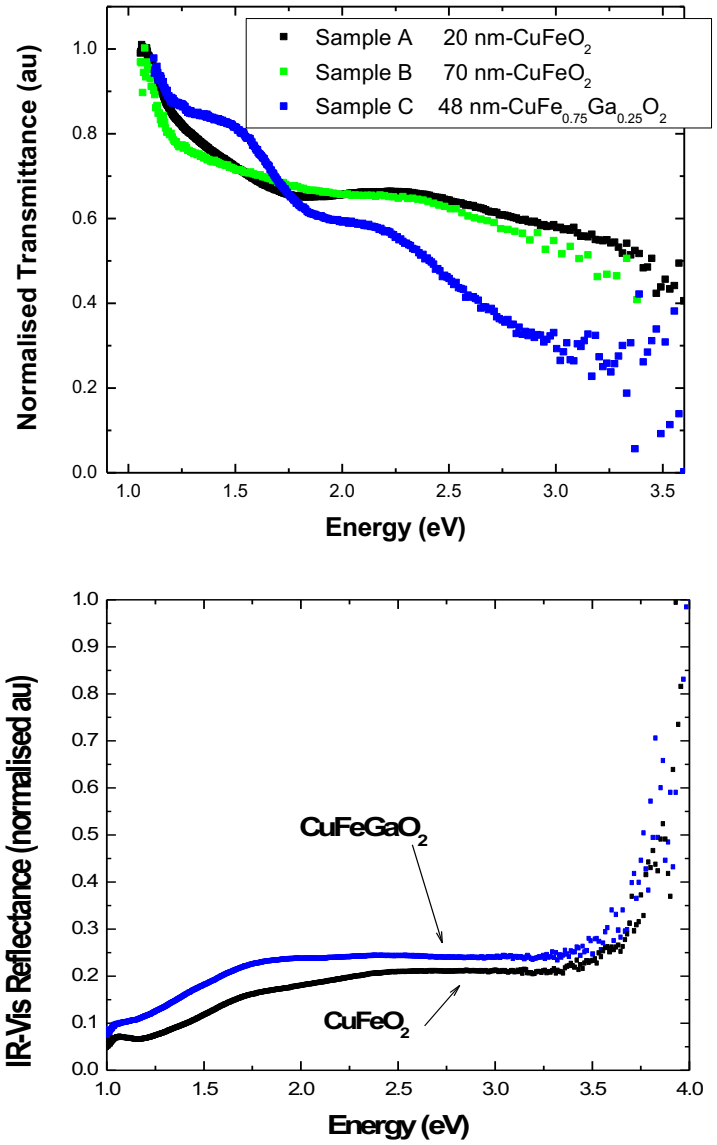


**Figure 3-11:** (a) Transmittance and (b) diffuse reflectance spectra in the near infrared and visible spectra measured for both kinds of samples (CFO133 in black, CFO161in green and CFOCGO7 in blue).

A more interesting property that is measurable from this transmittance and diffuse reflectance is the optical bandgap, firstly is necessary to calculate the optical absorption from the spectra showed in Figure 3-11 and then use the Tauc pot to determine the bandgap according to the method described in Appendix H

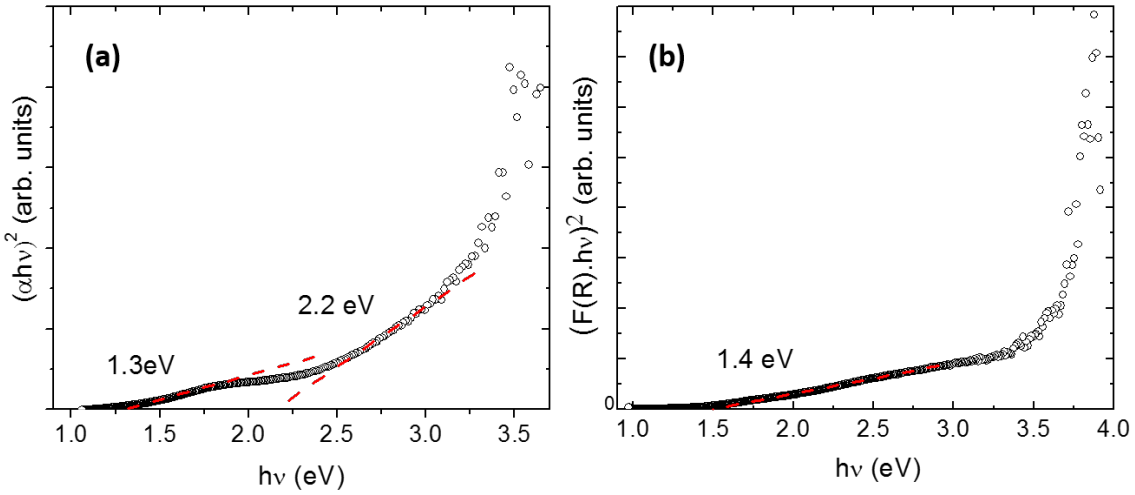


**Figure 3-12:** Tauc Plots for direct band gap obtained from (a) transmittance and (b) diffuse reflectance of $CuFeO_2$ 21 nm sample (CFO133).

In Figure 3-12 Tauc plots for direct gap obtained from transmittance and reflectance of $CuFeO_2$ sample are shown, as it can be seen from both plots more than one linear region is observable. From Figure 3-12 (a) there are three possible linear regions, and according to Tauc equation the projections of these linear regions to $y=0$ will be $x=E_g$ so in this case we can calculate 2 possible direct bandgaps, 1.29±0.01 eV and 2.18±0.07 eV. Following similar procedure with the plot in Figure 3-12 (b) and one direct bandgap is determined from diffuse reflectance, 1.42±0.02 eV. These results agree with other experimental reports that showed indirect bandgap at 1.15ev and a direct transition at 2.03 eV and 3.2 eV [44 – 46], also some theoretical calculation have predicted direct gap transitions at 1.30, 2.06 and 3.20 eV for pure $CuFeO_2$ [47, 48]. Plots for indirect allowed transition (n=1/2 in equation (4-22)) were also performed, but in this case, are not showed.

As showed in Table 3-4, results for direct optical transitions obtained from transmittance Tauc plots showed two transitions (1.3 eV and 2.2 eV) for the two $CuFeO_2$ samples studied, while there is only one observable transition in tauc plots obtained from diffuse reflectance data. To discuss the results from both transmittance and reflectance,

reference is given to the theoretical work of Haycock et al. [49]. For the $CuFeO_2$ thin films, we have measured fundamental absorption edges in the region of 1.3 eV, these results can be compared and attributed to the expected 1.2–1.4 eV indirect L–Γ transitions forecasted in [49], with an expected Urbach tail formed from sub-gap indirect d-d state transitions. Both $CuFeO_2$ samples displayed the activation of a direct transition in the 2.2 eV region, this absorption edge can be attributed to the activation of direct L-point transitions and direct Γ-point transitions calculated to be at 1.6 eV and 2.4 eV respectively [49]. It is possible that the absorption observed in this spectral region takes place via a super-positioning of direct transitions over both symmetry points.

The measured band gaps from reflectance (Figure 3-12 (b)) show a main dependence on an absorption edge observed at 1.4 eV corresponding to direct transitions. There are two possible ways of viewing this discrepancy between reflectance and transmittance data: Firstly, the absence of the absorption edge at 2.2 eV could indicate that a relatively large optical path length is required in order for the direct L and Γ- point transitions to have a strong effect on the spectra. Secondly, because the lower band gap at 1.0–1.3 eV is expected to emerge from indirect transitions and the spectra shows a strong direct absorption edge in this region, the reflectance spectra may represent direct L and Γ-point transitions assisted by intra-gap states emerging from the discontinuity of the crystalline structure at the surface. In either case, these results suggest that relatively large optical path lengths are required to observe the absorption edge related to the direct fundamental gap within these samples.

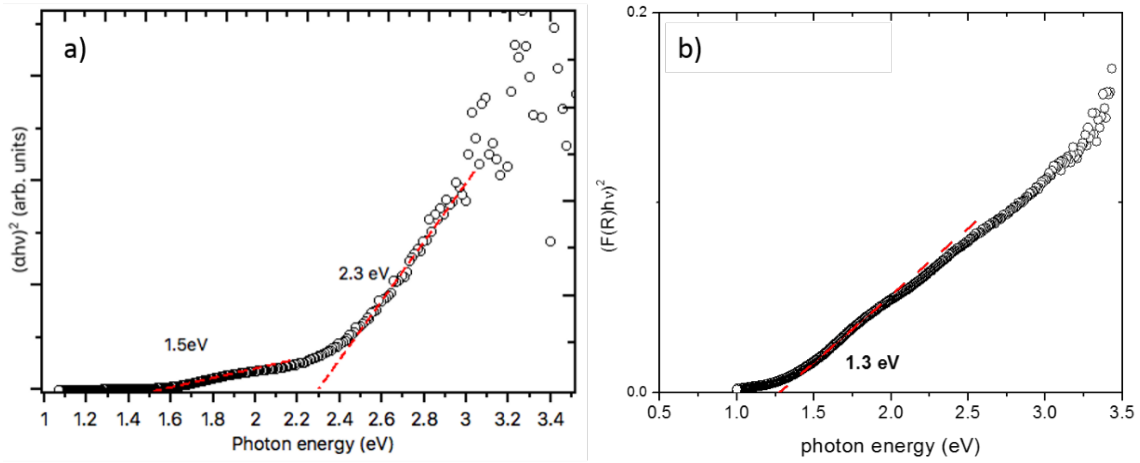


**Figure 3-13:** Tauc plots for direct transition obtained from (a) transmittance and (b) diffuse reflectance for $CuFe_{0.75}Ga_{0.25}O_2$ 48 nm thickness sample (CFOCGO7).

The same analysis to determine the optical transitions was performed with $CuFe_{0.75}Ga_{0.25}O_2$ samples and is shown in Figure 3-13. Plots in Figure 3-13 (a) and (b) showed two main direct transitions at 1.50±0.04 eV and 2.30±0.09 eV from transmittance, and one at 1.28±0.06 eV from reflectance. The estimated gaps for this alloyed sample are slightly different to the ones obtained for the pure $CuFeO_2$ sample, as expected due to iron substitution by gallium. First, the primary gap – located in the NIR region for $CuFeO_2$ – was found to be close to 1.50±0.04 eV for direct transitions showing an apparent upward shift in energy from the 1.3 eV recorded for the pure $CuFeO_2$ samples and may represent a change in optical gap brought about by the hybridization of $CuFeO_2$ with $CuGaO_2$. Further up the energy range, a strong absorption edge emerged corresponding to a Tauc-gap of approximately 2.30±0.09 eV. Moreover, the gradient of this absorption edge was found to have increased compared to the absorption edges at 2.2 eV for the pure $CuFeO_2$ samples.

The fundamental direct Tauc-gap measured at 1.5 eV from transmittance is comparable to the absorption edge reported by Lekse et al. [44] for $CuFe_{1-x}Ga_xO_2$ with x = 0.85 who describe the position of this absorption edge as being independent of fractional iron

content. As with the studies of Lekse et al. [44], an expected outcome of B-site alloying of gallium and iron is the breaking of Delafossite crystal symmetry, which is expected to modify selection rules leading to the increased availability of transition states.

Following a similar analysis as the one exposed for $CuFeO_2$ films, the direct gap obtained from transmittance at 2.30±0.09 eV for $CuFe_{0.75}Ga_{0.25}O_2$ film can be attributed to the activation of direct L-point transitions and direct Γ-point transitions calculated to be at 1.6 eV and 2.4 eV respectively for $CuFeO_2$ [49] and 2.54 eV and 1.81 eV respectively for $CuGaO_2$ [50]. It is possible that the absorption observed in this spectral region takes place via a super-positioning of direct transitions over both symmetry points and the increase of this direct transition observed will be explained by the addition of this extra sites on the lattice.

Reflectance tauc gap is observed at 1.28±0.06 eV not showing the shifting up that transmittance tauc gaps showed due to iron substitution by gallium. This result is explained by the fact that $CuFe_{0.75}Ga_{0.25}O_2$ samples were constructed in a way that top layers on the surface are $CuFeO_2$ as described in section 1.3.1 and then confirmed with results of sections 3.1.1 and 3.1.3 (XRD and XPS results respectively). So, as reflection transitions are surface dependent it would be wise to think that both samples ($CuFeO_2$ and $CuFe_{0.75}Ga_{0.25}O_2$) may have the same reflection tauc gap.

Optical band gaps measured by tauc method for different samples studied are shown in Table 3-4, where it is possible to observe a trend for both kinds of samples. Main optical transitions were estimated by averaging transitions of different samples and is also shown in Table 3-4. As it can be seen from Figure 3-12 there is a linear region observable at higher energy regions that shows an optical transition at 3.30±0.42 eV that has not been considered due to low sensitivity of the photodiodes at that photon energy and in consequence to high scattering on data collected in that region. Unless this optical transition is in good agreement with values reported previously [44 - 48].

| | Transmittance Tauc gaps | Reflectance Tauc gaps |
|---|---|---|
| **$CuFeO_2$** | 1.29±0.01 eV | 1.42±0.02 eV |
| **20 nm** | 2.18±0.07 eV | - |
| **$CuFeO_2$** | 1.27±0.02 eV | 1.84±0.03 eV |
| **75 nm** | 2.22±0.03 eV | - |
| **$CuFe_{0.75}Ga_{0.25}O_2$** | 1.50±0.04 eV | 1.28±0.06 eV |
| **48 nm** | 2.30±0.09 eV | - |

**Table 3-4:** Summary of all measurable direct transitions from Tauc plots.

This shifting of the optical transitions with the addition of $CuGaO_2$ to the $CuFeO_2$ lattice was also observed by J. W. Lekse et al. [44] with $CuGa_{1-x}Fe_xO_2$ with x = 0.05, 0.10, 0.15, 0.20, synthetized by solid state method, in this work they observed a reduction of the band gap due to the substitution of gallium with iron. This information lead us to think that substitution or doping will allow to progressively change the position of optical transition in this kind of material leaving open the possibility of adjust the band gap to a certain desired value.

## 3.2. Gas Adsorption Properties.

In section 3.1 we discussed about the nature of samples studied during this work realizing that our stack of samples is composed of epitaxial $CuFeO_2$ and $CuFe_{0.75}Ga_{0.25}O_2$, and the second kind of samples showed an alloy structure more than a super lattice structure and the optical properties were modified due to gallium substitution of iron. In this section, we will discuss the implications of this substitution on gas adsorption properties.

In Figure 3-14 XPS measurement for Fe 2p and Cu 2p band and peak fitting before and after $CO_2$ exposure are shown, as it can be seen from Cu 2p fitting the presence of more sites corresponding to a carboxylate structure formed via coordination of a bent $CO_2^{-\delta}$ molecule to a Cu center similar in binding energy to a $CuCO_3$ (copper carbonate) is evident [51]. The position of the Cu (L3VV) Auger peak (not showed) now shifted to at 917.2 eV, also confirmed this chemical state.

From Fe 2p band is more difficult to identify changes attributable to $CO_2$ exposure because iron carbonates and hydroxylates have the same binding energy that FeO oxides [41 – 43], despite this an increase of peak attributable to FeO, carbonates and hydroxylates increase in relative intensity with $CO_2$ exposure.

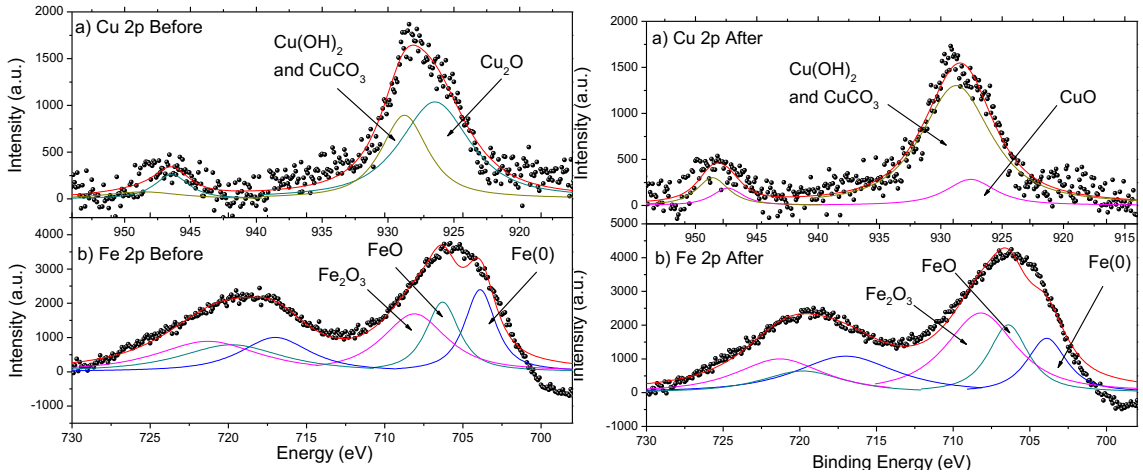


**Figure 3-14:** XPS high resolution spectra of (a) Cu 2p and (b) Fe 2p before and after $CO_2$ exposure of $CuFeO_2$ film 75nm in thickness sample (CFO161).

The XPS spectra for C 1s and O 1s were also recorded before and after $CO_2$ dosage and after TPD. XPS spectra of the C 1s band are shown in Figure 3-15 before and after $CO_2$ dosage. Adventitious carbon which appears at a binding energy of 284.6 eV was not completely removed in order to have a reference to determine binding energies of other elements due to sample surface charging. After $CO_2$ dosage, an important increase of the

peak located at 290 eV, attributed to an increase of carbon due to $CO_2$ exposure, was observed. XPS spectra of the O 1s band are shown in Figure 3-15 before and after $CO_2$ dosage, the O 1s fit showed an increase of peaks attributed to the bonding within metal carbonates ($CO_3^{2-}$) [37] and water after $CO_2$ exposure.

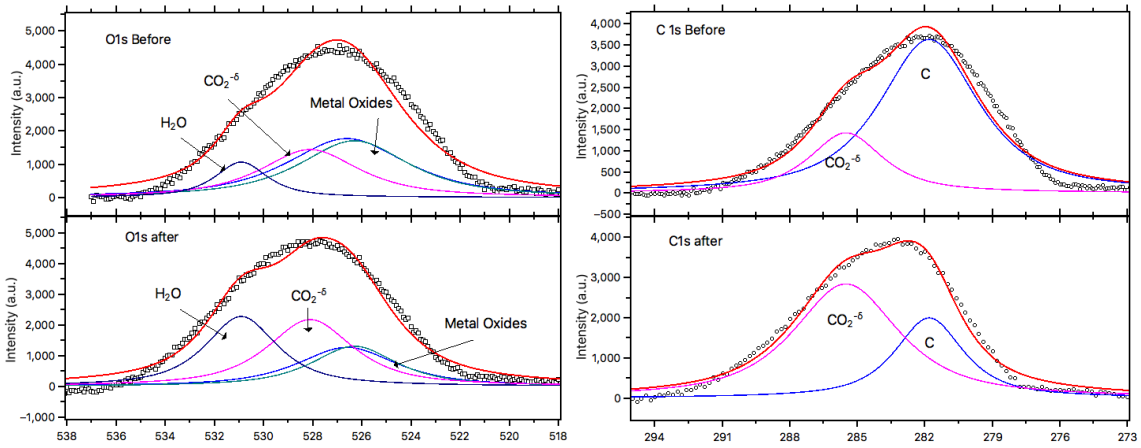


**Figure 3-15:** XPS measurements of O1s and C1s bands for $CuFeO_2$ 75 nm film (CFO161) before and after $CO_2$ exposure.

Same analysis was performed for $CuFe_{0.75}Ga_{0.25}O_2$ samples obtaining quite similar results to those obtained for pure $CuFeO_2$ discussed previously, for $CuFe_{0.75}Ga_{0.25}O_2$ samples there was also an increase of peaks related to $CO_2^{-\delta}$ and hydroxylates bonding with metal oxide surface after $CO_2$ exposure. This results shows that in both cases $CO_2$ and/or $H_2O$ is being chemisorbed on metal oxide surface.

### 3.2.1. Thermal Programmed Desorption.

Then, samples were fast heated to perform a thermal programed desorption (TPD) and to measure the released gases using a mass spectrometer. Temperature and partial pressure of different gases, such as $CO_2$, $H_2O$ and CO, were measured at the same time. Then, spectra were corrected using the protocol described in Appendix D.1

This procedure was repeated with sample holder without sample and with a clean substrate, to distinguish between sample's desorption and sample holder desorption the spectrum of the sample holder with a clean substrate was subtracted from samples desorption spectra, as described in Appendix D.2. With this procedure, clean desorption peaks associated to different gases were obtained for both kinds of samples.

Thermal programmed desorption of $CuFeO_2$ and $CuFe_{0.75}Ga_{0.25}O_2$ samples is shown in Figure 3-16, from figure it is possible to see that a double peak is observed for $CuFeO_2$ and a single peak is observed for $CuFe_{0.75}Ga_{0.25}O_2$, also the main gas desorbed by $CuFeO_2$ is water meanwhile for $CuFe_{0.75}Ga_{0.25}O_2$ is not completely clear because $CO_2$ and $H_2O$ peaks are quite similar in intensity.

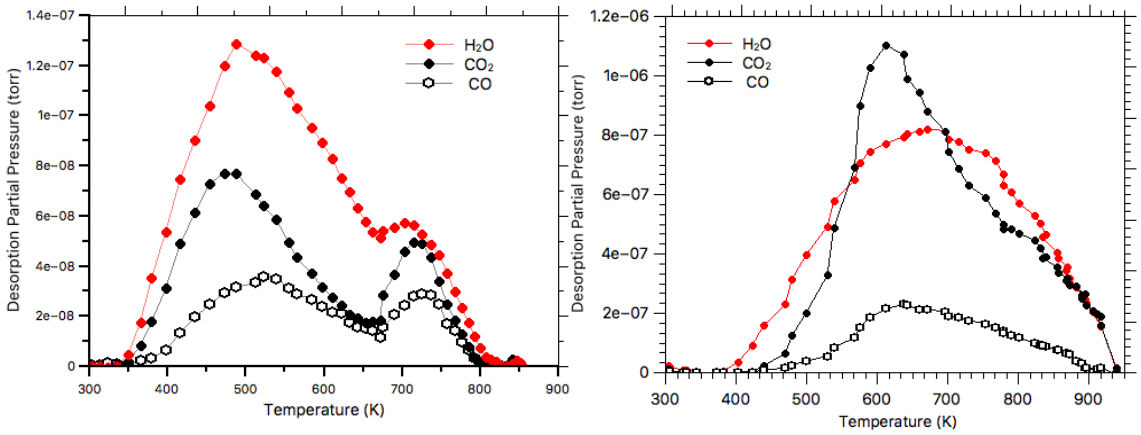


**Figure 3-16:** Thermal desorption spectra of (a) $CuFeO_2$ 100 nm thickness (CFO168) after 1500L dose and heating rate $\mathbf{14.5 \pm 0.3}\ \boldsymbol{K/s}$ and (b) $CuFe_{0.75}Ga_{0.25}O_2$ 48 nm thickness (CFOCGO7) after 4500L and heating rate $\mathbf{25.4 \pm 0.7}\ \boldsymbol{K/s}$.

As the area above partial pressure is proportional to the number of gas molecules desorbed by samples, it is possible to compare relative intensities in each case. If we consider that all the molecules come from a different absorption site, we can consider

that the sum of all peaks area will represent 100% of the available sites. The portion of total sites occupied by each gas can be determined by

$$N_i = \frac{A_i}{\sum_j A_j} \times 100, \quad (3\text{-}1)$$

where $A_i$ correspond to the area of the desorption peak. Using equation (3-1) we can determine the contribution of each gas to the desorption spectrum, in Table 3-5 contributions of each gas to spectra in Figure 3-16 are shown. In both samples the main gas desorbed is water, unless the doses contained less than 1% of water. The main difference is observed in $CO_2$ and CO, the addition substitution of iron with gallium in the Delafossite structure generated an increase of desorbed $CO_2$ and a decrease of CO. As samples were exposed to 99% $CO_2$ and 1% $H_2O$, we can assume that CO and $CO_2$ comes from the same absorption sites and CO is a resulting species of $CO_2$ reduction on samples surface.

| | $CO_2$ | $H_2O$ | CO |
|---|---|---|---|
| $CuFeO_2$ | 29.9% | 54.8% | 15.3% |
| $CuFe_{0.75}Ga_{0.25}O_2$ | 44.0% | 46.5% | 9.5% |

**Table 3-5:** relative intensities of gases desorbed by samples**.**

As it can be seen from Table 3-5, the substitution of iron by gallium generated an increase of sites available for $CO_2$ adsorption, but decreased the catalytic activity for $CO_2$ reduction. It is important to note the remarkable capability of Delafossite samples to adsorb water in this conditions, considering that water was present in a very low concentration in both cases.

Desorption pressure curves in Figure 3-16 were used to calculate the normalized desorption rate spectrum N(T) according to equation, then by normalization of the

curves it was possible to determine N(T)/Np curves of Figure 3-17, Figure 3-18 and Figure 3-19.

$$\beta \frac{dP(T)}{dT} + \frac{P(T)}{\tau} = \frac{N(T)}{\sigma_0} \qquad (3\text{-}2)$$

Where $\tau = \frac{V}{S}$ is the characteristic pumping time with V the system volume ($4 \times 10^{-2}$ $m^3$) and S the pumping speed of the system (0.15 $m^3/s$).

Fitting of TPD spectra was performed for samples using two second order desorption peaks as showed in equation (4-14). Fittings of water TPD spectrum for $CuFeO_2$ and $CuFe_{0.75}Ga_{0.25}O_2$ samples is shown in Figure 3-17. As can be seen from Figure 3-17 in both cases the two peaks contribution model adjust with the experimental data and agrees with P.A. Redhead theoretical description of thermal desorption [52], where higher heating rates will cause higher peak temperatures.

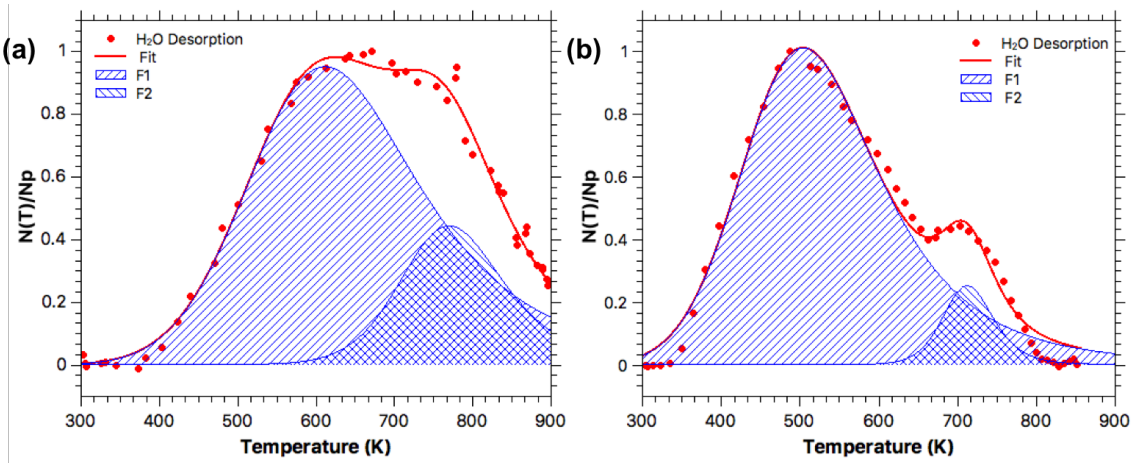


**Figure 3-17:** Peak fitting of $H_2O$ TPD spectra of (a) $CuFe_{0.75}Ga_{0.25}O_2$ film 48 nm in thickness (CFOCGO7) and (b) $CuFeO_2$ film 100 nm in thickness (CFO168).

Peak fitting for $CO_2$ desorption was performed in a similar way, second order desorption peaks are attributed to $CO_2$ formed by recombination of reduced $CO_2$ into CO and then recombined with oxygen from the ambient and by surface recombination during the adsorption process.

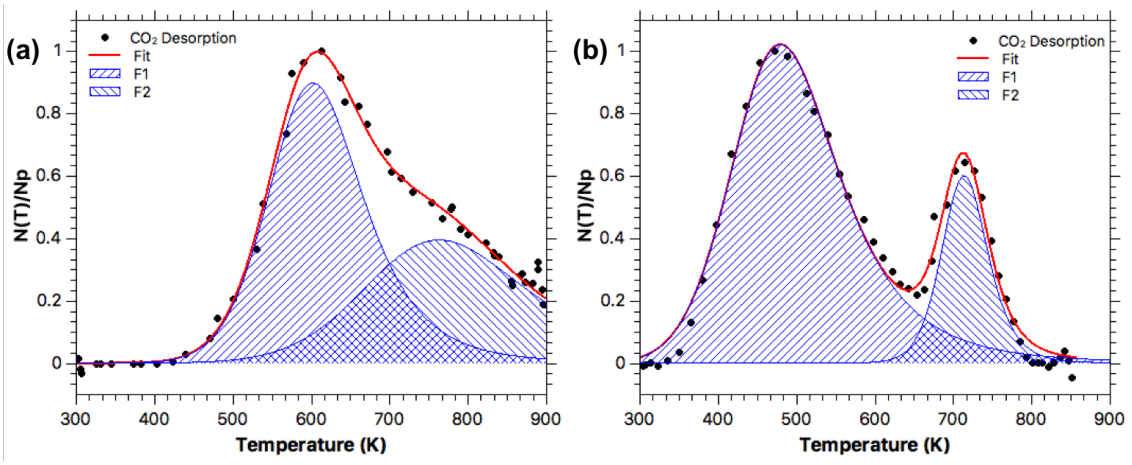


**Figure 3-18:** Peak fitting of $CO_2$ TPD spectra of (a) $CuFe_{0.75}Ga_{0.25}O_2$ film 48 nm in thickness (CFOCGO7) and (b) $CuFeO_2$ film 100 nm in thickness (CFO168).

Finally, for CO desorption spectra fitting was performed considering two second order desorption peaks, this kind desorption peaks were chosen due to absence of CO in the dosage and the only possibility of releasing CO from samples is due to $CO_2$ reduction.

According to equations (4-13) and (4-14) activation energy of desorption reaction can be determined from fitting as well as temperature of the desorption peak (maximum value). Activation energies of desorption reaction and peak temperature (Tp) obtained from fits in all selected samples are summarized in Table 4-3 (water desorption), Table 4-4 ($CO_2$ desorption) and Table 4-5 (CO desorption) in Appendix A.4, from these tables average activation energies were calculated for each gas studied, all these results are shown in Table 3-6.

From average activation energies showed in Table 3-6 we can observe a decrease in desorption energy of $CO_2$ with the addition gallium explaining the increase of desorbed $CO_2$ and the reduction of catalytic activity.

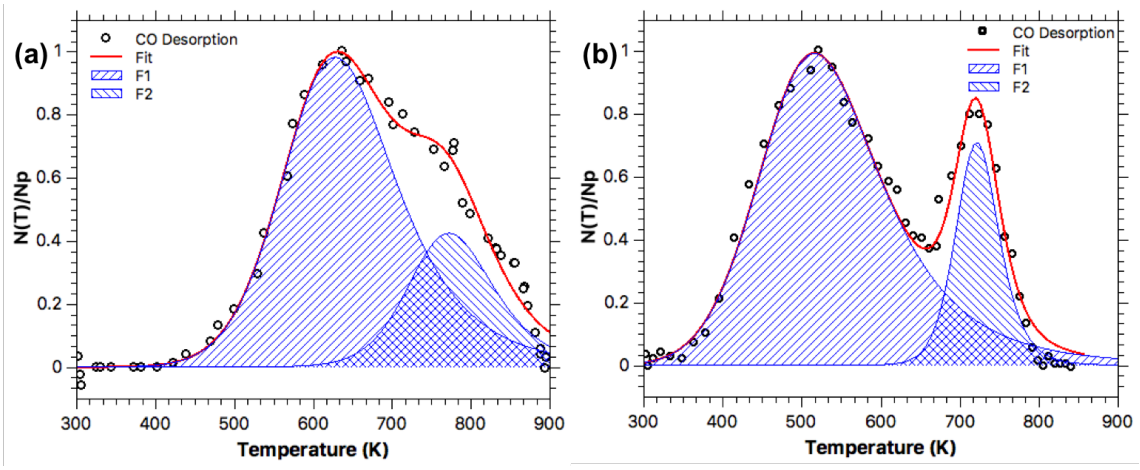


**Figure 3-19:** Peak fitting of CO TPD spectra of (a) $CuFe_{0.75}Ga_{0.25}O_2$ film 48 nm in thickness and (b) $CuFeO_2$ film 100 nm in thickness.

Activation energy for CO desorption did not showed an important variation at first instance with the addition of gallium, the first activation energy 0.6±0.4 eV/atom and 0.5±0.1 eV/atom are consistent with the -0.53 eV of thermodynamic potential for CO production from $CO_2$ described in Table 1-1, also both activation energies obtained for CO matches with energies obtained from $CO_2$ desorption with a relative error of 50% and 6.7% in first and second peaks respectively, this result gives a good sign for catalytic activity of $CuFeO_2$. Then with addition of gallium to the lattice the CO activation energy of the first peak is slightly lower than energy obtained for $CuFeO_2$ sample (0.5±0.1 eV/atom), although this value is still matching with desorption energy obtained for $CO_2$ with a relative error of 20%, the second peak has higher activation energy that the one obtained for $CO_2$ (42.9% relative error), this will also explain the decrement of catalytic activity in $CuFe_{0.75}Ga_{0.25}O_2$ sample.

Water desorption activation energy of $CuFeO_2$ also showed similar activation energies in both peaks with CO. In this case, we obtained 0.4±0.2 eV/atom and 1.5±0.8 eV/atom with a relative error of 33.3% and 1.3% respectively, this situation gives a glimpse of obtaining water trough recombination of desorbed gases or from surface reaction more than direct desorption of $H_2O$, this confirm the idea described in the analysis of CO desorption energies and agrees with reaction described in Table 1-1.

Considering previous discussion, results in Table 3-6 support the idea of better catalytic activity on $CuFeO_2$ than in $CuFe_{0.75}Ga_{0.25}O_2$ at first instance in contrast with results obtained by J.W. Lekse et al. [44] this contrast may be explained by results of S. Kato et al. [53] because they found better interactions of $CuFeO_2$ with $O_2$ than $CuGaO_2$ at lower temperatures, then wen increasing temperature $CuGaO_2$ takes the lead and overpass absorption activity recorded by $CuFeO_2$.

| Sample | $H_2O$ | | $CO_2$ | | CO | |
|---|---|---|---|---|---|---|
| | $E_1$ (eV/atom) | $E_2$ (eV/atom) | $E_1$ (eV/atom) | $E_2$ (eV/atom) | $E_1$ (eV/atom) | $E_2$ (eV/atom) |
| $CuFeO_2$ | 0.4±0.2 | 1.5±0.8 | 0.3±0.1 | 1.6±0.7 | 0.6±0.4 | 1.5±0.6 |
| $CuFe_{0.75}Ga_{0.25}O_2$ | 0.4±0.1 | 0.8±0.3 | 0.4±0.2 | 0.8±0.5 | 0.5±0.1 | 1.4±0.8 |

**Table 3-6:** Summary of activation energy of desorption obtained from curves fitting of thermal desorption spectra. Sub index enumerate peaks on the fitting.

In general, there is not much information in the literature about desorption energy for $CO_2$ chemisorption on oxide surfaces that allows us to compare our results with other results. Isahank et al. [54] studied the adsorption desorption of $CO_2$ in copper oxides ($Cu_2O$ and CuO) by different analytical methods including XPS, they report the formation of copper carbonates after $CO_2$ adsorption and observed the same $CO_2^{-\delta}$ binding energy after $CO_2$ adsorption. In that work, they reported adsorption/desorption activation energies of 141 kJ/mole (1.46 eV/atom) for $Cu_2O$ and 45 kJ/mole (0.46

eV/atom) for CuO. Breyer et al [55] worked on kinetics of adsorption and desorption process of $CO_2$ by α-$Fe_2O_3$, obtaining activation energy of 112.8 kJ/mole (1.17 eV/atom) from TPD fitting. Activation energies obtained for $Cu_2O$ and $Fe_2O_3$ are consistent with our results using $CuFeO_2$ due to similar chemisorption method ($CO_2^{-\delta}$) bending, consistent with the idea of recombination due to catalytic activity explained before.

In order to explain the TPD data and knowing that chemisorption on oxide surfaces is related to oxygen vacancies [56], we can sketch the following reactions taking place at the surface of Delafossite oxides

$$CO_2 \xrightarrow{adsorption} CO_2^{ads} \xrightarrow{\substack{surface \\ difussion}} CO^{ads} + O^{ads} \tag{3-3}$$

$$H_2O \xrightarrow{adsorption} H_2O^{ads} \xrightarrow{\substack{surface \\ difussion}} OH^{ads} + H^{ads} \tag{3-4}$$

$$(CO^{ads} + O^{ads}) + (OH^{ads} + H^{ads}) \xrightarrow{\substack{surface \\ difussion}} COOH^{ads} + OH^{ads} \tag{3-5}$$

$$2COOH^{ads} + 2OH^{ads} \xrightarrow{desorption} CO_2 + 2H_2O + CO + 2O \tag{3-6}$$

This reaction implies that more $H_2O$ than $CO_2$ will be released after desorption showing a good agreement with results showed in Table 3-5, also this reaction gives a good explanation to the fact that CO, $CO_2$ and $H_2O$ shows similar desorption energies for second order desorption peaks adjusted (see Table 3-6). For pure $CuFeO_2$ sample it was possible to identify two desorption energies in common for all these three gases, first desorption with energy of 0.4±0.2 eV/molecule and then with 1.5±0.7 eV/molecule. For $CuFe_{0.75}Ga_{0.25}O_2$ sample the relationship between all gases desorption is not so clear, but if we consider a desorption model like the one for $CuFeO_2$, 0.4±0.1 eV/molecule and 1.0±0.5 eV/molecule desorption energies are obtained.

Then, if we consider that these two desorption reactions observed in TPD results form part of the same reaction we can estimate the desorption energies of $H_2O$, $CO_2$ and $CO_2$ at 1.0±0.8 eV/molecule for $CuFeO_2$ and 0.7±0.4 eV/molecule for $CuFe_{0.75}Ga_{0.25}O_2$.

# Chapter 4: Conclusions and Future work.

## 4.1. Conclusions

$CuFeO_2$ and $CuFe_{1-x}Ga_xO_2$ epitaxial thin films were produced using the pulsed laser deposition technique. Using XRD, GID and Raman spectroscopy we found that composition of the $CuFe_{1-x}Ga_xO_2$ sample is near the $CuFe_{0.75}Ga_{0.25}O_2$ stoichiometry and present an alloyed structure more than the desired multi lattice structure.

Chemical composition of samples surface was confirmed using XPS, as both samples were terminated in $CuFeO_2$, XPS spectra did not showed mayor differences between both samples. Evidence of semiconductor behavior was found from the "Tauc" analysis of the samples' characteristic transmittance and diffuse reflectance. Direct optical transitions were measured at 1.28±0.02 eV and 2.20±0.05 eV for pure $CuFeO_2$ samples showing good agreement with theoretical prediction and previous results of other researchers [35, 47 – 51]. Direct transition for $CuFe_{0.75}Ga_{0.25}O_2$ were measured at 1.50±0.04 eV and 2.30±0.09 eV, plots showed another higher transition near 3 eV but due to technical limitation this gap cannot be clearly determined. Reflectance Tauc gap for both kind of samples did not show mayor changes due to similar surface composition of samples, showing that reflectance is more surface dependent.

The difference between direct transitions measured for $CuFeO_2$ and $CuFe_{0.75}Ga_{0.25}O_2$ is associated with the inclusion of gallium in a solid solution and consequently producing changes to the optical characteristics of the semiconductor material. Similar results were observed by J. W. Lekse et al. [47] when working with $CuGaO_2$ and $CuGa_{1-x}Fe_xO_2$ materials. These results in conjunction with our results lead us to think of a progressive change in optical transitions due to metal substitution on the Delafossite oxide.

Carbon dioxide adsorption properties were studied via XPS and thermal programmed desorption on $CuFeO_2$ and $CuFe_{0.75}Ga_{0.25}O_2$ film, samples were exposed to $CO_2$ and confirmed the chemisorption of $CO_2$ onto its surface. These studies reveal that the samples surface interacted strongly with carbon dioxide and water, forming chemisorbed hydroxides and carbonates on the Cu–Fe oxide surface. We can ascertain from XPS characterization that a carboxylate structure formed via coordination of a bent $CO_2^{-\delta}$ molecule to a Cu center is present.

The activation energies for desorption were obtained from fitting of a combination of second order desorption peaks of the TPD spectrum obtained for each gas studied. Activation energy for second order desorption of $H_2O$, $CO_2$ and CO in both samples was found to be 1.0±0.8 eV/molecule for $CuFeO_2$ and 0.7±0.4 eV/molecule for $CuFe_{0.75}Ga_{0.25}O_2$. According to the approach described in section 3.2.1 both gases come from the same reaction occurring on sample surface. Also, the energy related to this reaction is in good agreement with $CO_2$ reduction thermodynamic potentials showed in Table 1-1.

Iron substitution for gallium in the Delafossite structure modified activation energies for thermal desorption in all cases, these changes of activation energy suggest a decrement of catalytic activity due to gallium addition into the lattice in short reaction times.

## 4.2. Future work

Most of this work relies on the characterization and study of adsorption properties of $CuFeO_2$ and $CuFe_{0.75}Ga_{0.25}O_2$ samples under $CO_2$ exposure, a good improvement of this work would be to perform this measurement to a wider variety of samples of the same family, i.e. to perform this measurement with $CuFe_{1-x}Ga_xO_2$ samples with x varying from 0 to 1 obtaining a good stack of samples that confirm the ideas exposed in this work regarding to catalytic activities of both kinds of samples under this conditions.

In order to have a better understanding of adsorption properties on the samples and of the factors that may have some effect on these properties it would be desirable to measure electrical conductivity of samples under different conditions, i.e. (i) in absence of light, (ii) in presence of light (full spectrum and spectroscopy), (iii) at controlled temperature and (iv) in presence of $CO_2$ gas. These conditions and its combinations may give useful information for better understanding of $CO_2$ absorption and catalytic reduction.

Also, to directly obtain the catalytic activity of these kind of samples it would be necessary to build a photo electrochemical reaction cell, were catalytic activity can be measured as function of: (i) samples composition, (ii) samples structure, (iii) light exposure and (iv) reaction time. Modifying samples structure will necessary imply a different synthesis method, like solid state or hydrothermal synthesis method where synthesis parameter like temperature, pressure or gas carrier has direct effects on samples structures (porosity, specific surface area, particles size, etc).

# Appendix

## Appendix A. Other Results

During the body of this thesis some representative results have been exposed in order to avoid redundancy during the text, but for better understanding this appendix present most of the experimental data recorded.

### Appendix A.1. X-Ray Diffraction

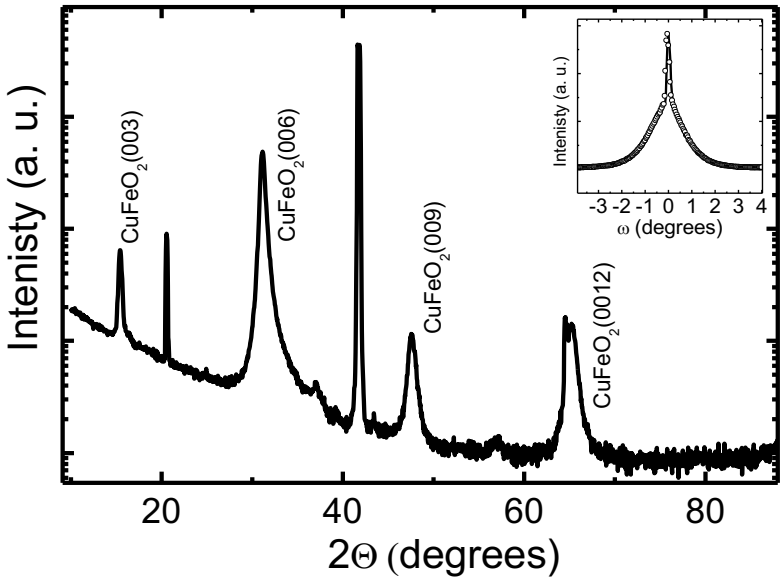


**Figure 4-1:** XRD Pattern for $CuFeO_2$ 25 nm thickness (FCO163) sample. Inset figure correspond to rocking curve in (006) direction peak.

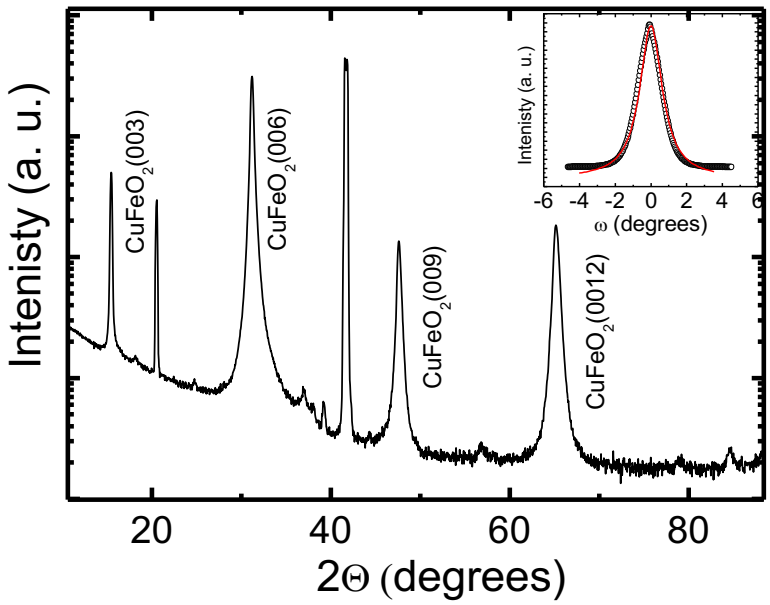


**Figure 4-2:** XRD Pattern for $CuFeO_2$ 100 nm thickness (FCO168) sample. Inset figure correspond to rocking curve in (006) direction peak.

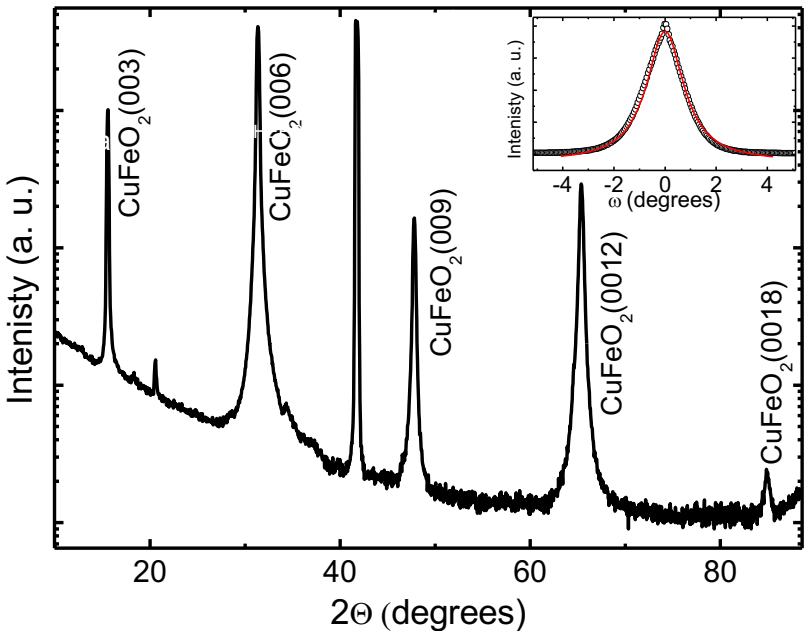


**Figure 4-3:** XRD Pattern for $CuFe_{0.75}Ga_{0.25}O_2$ 95 nm thickness (FCOCGO8) sample. Inset figure correspond to rocking curve in (006) direction peak.

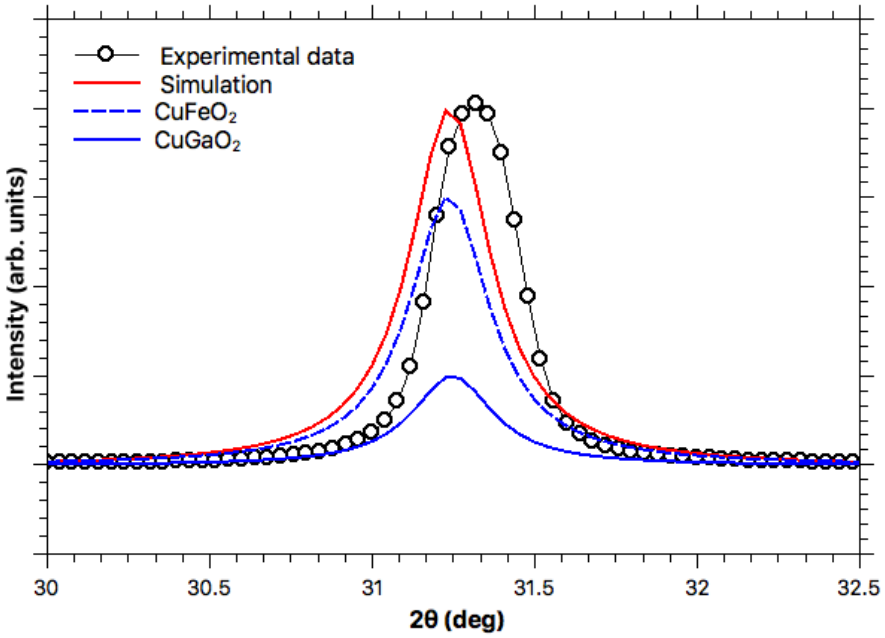


**Figure 4-4:** (006) direction peak comparison between $CuFe_{0.75}Ga_{0.25}O_2$ 95 nm thickness (FCOCGO8) sample and theoretical simulation.

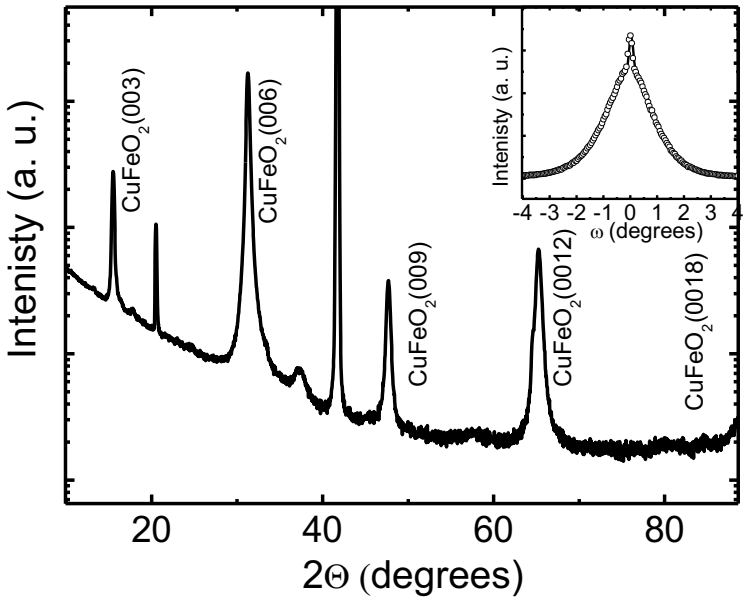


**Figure 4-5:** XRD Pattern for $CuFe_{0.75}Ga_{0.25}O_2$ 20 nm thickness (FCOCGO10) sample. Inset figure correspond to rocking curve in (006) direction peak.

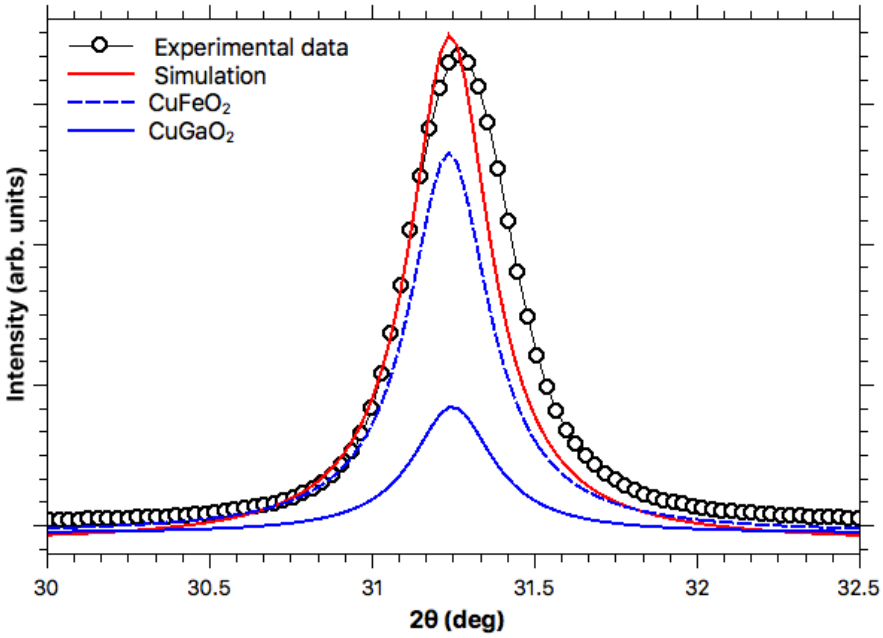


**Figure 4-6:** (006) direction peak comparison between $CuFe_{0.75}Ga_{0.25}O_2$ 20 nm thickness (FCOCGO10) sample and theoretical simulation.

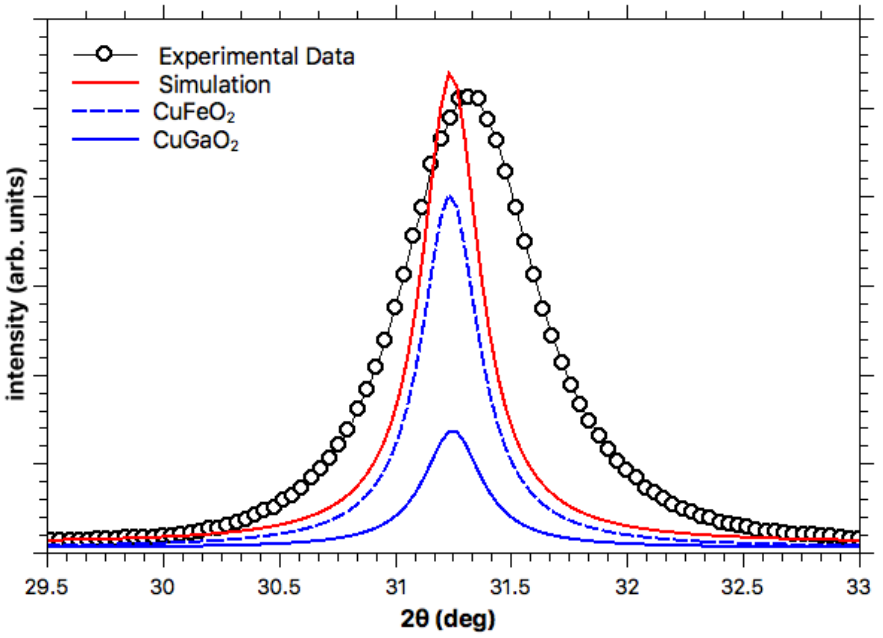


**Figure 4-7:** (006) direction peak comparison between $CuFe_{0.75}Ga_{0.25}O_2$ 48 nm thickness (FCOCGO7) sample and theoretical simulation.

X-ray diffraction (XRD) pattern of all samples described in Table 1-2ware measured, for all spectra Lorentzian peaks were fitted for getting each peak center. Results obtained for $CuFeO_2$ samples are summarized in Table 4-1

| $CuFeO_2$ Reference | | CFO133 | | CFO163 | | CFO161 | | CFO168 | |
|---|---|---|---|---|---|---|---|---|---|
| Xc | direction | $X_c$ | $R^2$ | $X_c$ | $R^2$ | $X_c$ | $R^2$ | $X_c$ | $R^2$ |
| 15.473 | (003) | 15.465±0.012 | 0.663 | 15.409±0.002 | 0.986 | 15.428±0.003 | 0.985 | 15.452±0.002 | 0.980 |
| Substrate | | 20.573±0.007 | 0.748 | 20.531±0.003 | 0.971 | 20.552±0.003 | 0.971 | 20.523±0.003 | 0.964 |
| 31.238 | (006) | 31.198±0.002 | 0.992 | 31.137±0.002 | 0.992 | 31.140±0.003 | 0.993 | 31.193±0.002 | 0.995 |
| Substrate | | 41.744±0.009 | 0.821 | 41.752±0.012 | 0.828 | 41.753±0.012 | 0.844 | 41.714±0.011 | 0.848 |
| 47.667 | (009) | 47.565±0.005 | 0.983 | 47.608±0.003 | 0.995 | 47.597±0.003 | 0.995 | 47.618±0.002 | 0.994 |
| 65.156 | (0012) | 64.678±0.011 | 0.876 | 65.216±0.003 | 0.996 | 65.072±0.024 | 0.861 | 65.189±0.003 | 0.995 |
| **C lattice parameter** | | | | | | | | | |
| 17.166 Å [57] | | 17.303±0.006 Å | | 17.404±0.015 Å | | 17.170±0.001 Å | | 17.148±0.002 Å | |

**Table 4-1:** XRD pattern peaks position and calculated c lattice parameter for all $CuFeO_2$ samples. Reference for $CuFeO_2$ peak position was obtained from JCP2 chart #00-039-0246.

Same procedure was followed with $CuFe_{0.75}Ga_{0.25}O_2$ samples, results obtained are summarized in Table 4-2.

| $CuFeO_2$ Reference | | $CuGaO_2$ Reference | | CFOCGO10 | | CFOCGO7 | | CFOCGO8 | |
|---|---|---|---|---|---|---|---|---|---|
| $X_c$ (deg) | direction | $X_c$ (deg) | direction | $X_c$ (deg) | $R^2$ | $X_c$ (deg) | $R^2$ | $X_c$ (deg) | $R^2$ |
| 15.473 | (003) | 15.482 | (003) | 15.504±0.002 | 0.987 | 15.533±0.004 | 0.985 | 15.539±0.003 | 0.977 |
| Substrate | | | | 20.513±0.003 | 0.961 | 20.508±0.004 | 0.966 | 20.543±0.004 | 0.974 |
| 31.238 | (006) | 31.249 | (006) | 31.275±0.002 | 0.994 | 31.321±0.002 | 0.998 | 31.335±0.003 | 0.981 |
| Substrate | | | | 41.741±0.010 | 0.862 | 41.741±0.014 | 0.824 | 41.732±0.010 | 0.883 |
| 47.667 | (009) | 47.678 | (009) | 47.693±0.002 | 0.997 | 47.703±0.005 | 0.988 | 47.784±0.002 | 0.995 |
| 65.156 | (0012) | 65.171 | (0012) | 65.258±0.002 | 0.997 | 65.251±0.014 | 0.942 | 65.368±0.001 | 0.997 |
| **C lattice parameter** | | | | | | | | | |
| 17.166 Å [57] | | 17.154 Å [57] | | 17.155±0.005 Å | | 17.163±0.006 Å | | 17.125±0.003 Å | |

**Table 4-2:** XRD pattern peaks position and calculated c lattice parameters for all $CuFe_{0.75}Ga_{0.25}O_2$ samples. Reference for $CuFeO_2$ and $CuGaO_2$ peak position was obtained from JCP2 chart #00-039-0246 and #00-041-0255.

.

## Appendix A.2. Raman Spectroscopy

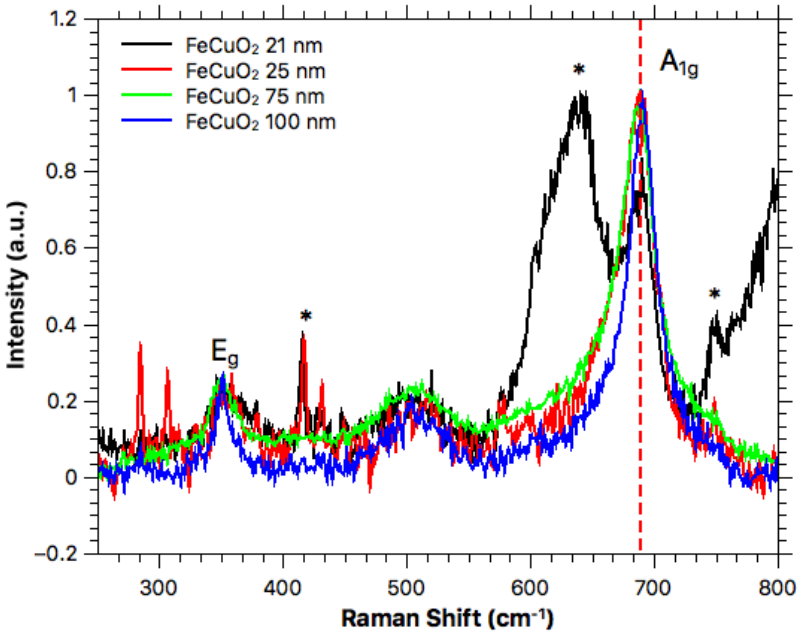


**Figure 4-8:** Raman spectra of all $CuFeO_2$ samples (CFO133, CFO163, CFO161, CFO168).

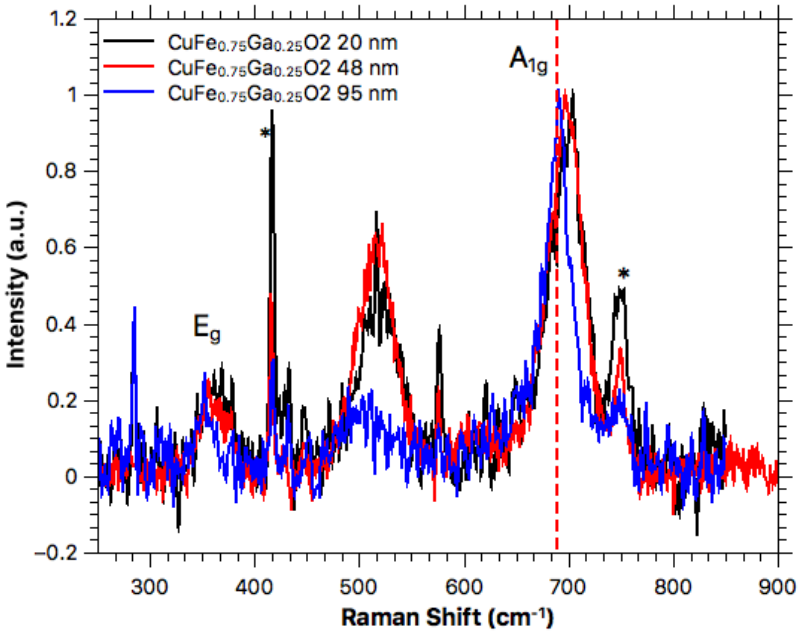


**Figure 4-9:** Raman spectra of all $CuFe_{0.75}Ga_{0.25}O_2$ samples (CFOCGO10, CFOCGO7, CFOCGO8).

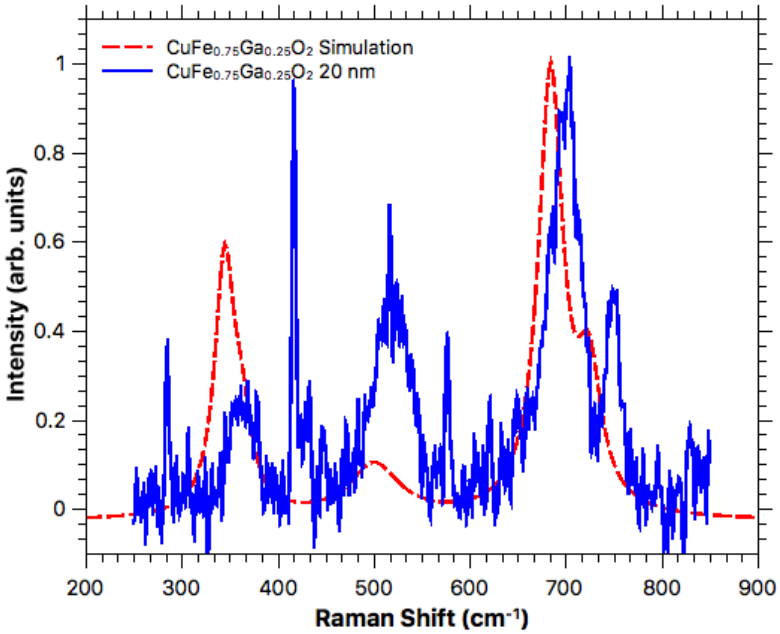


**Figure 4-10**: Comparison between $CuFe_{0.75}Ga_{0.25}O_2$ simulated Raman spectrum and experimentally obtained Raman spectrum from 20 nm thickness sample (CFOCGO10).

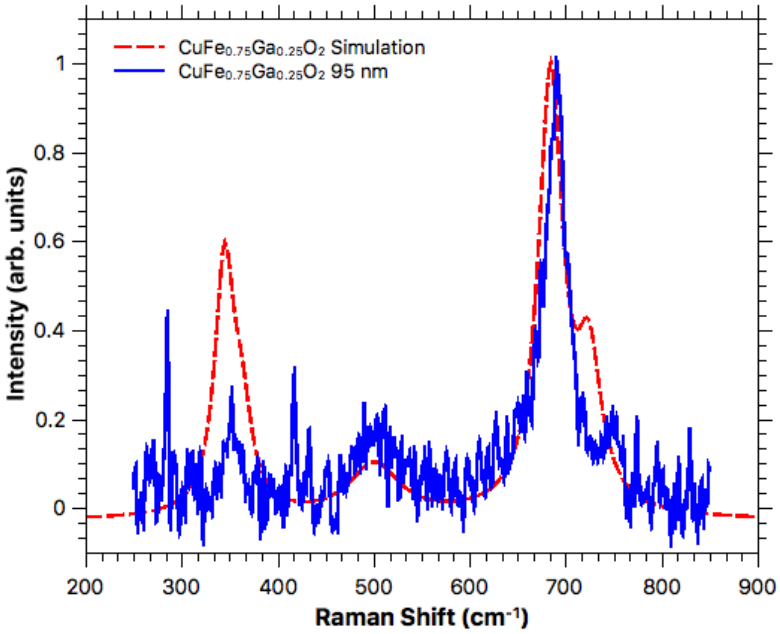


**Figure 4-11:** Comparison between $CuFe_{0.75}Ga_{0.25}O_2$ simulated Raman spectrum and experimentally obtained Raman spectrum from 95 nm thickness sample (CFOCGO8).

# Appendix A.3. X-Ray Photoelectron Spectroscopy

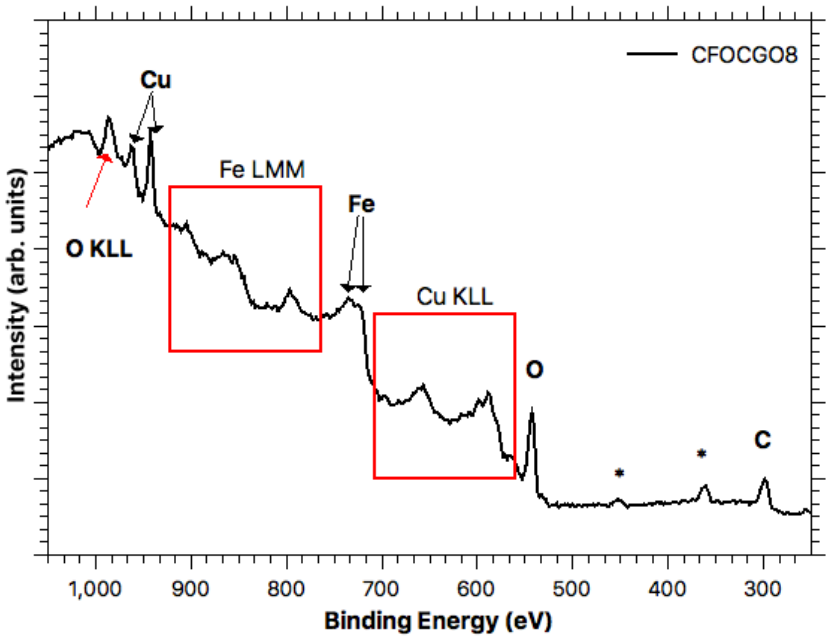


**Figure 4-12:** X-ray Photoelectron survey spectrum of $CuFe_{0.75}Ga_{0.25}O_2$ 95 nm thickness (CFOCGO8) sample with principal peaks identified, peaks labeled with * correspond to sample holder peaks.

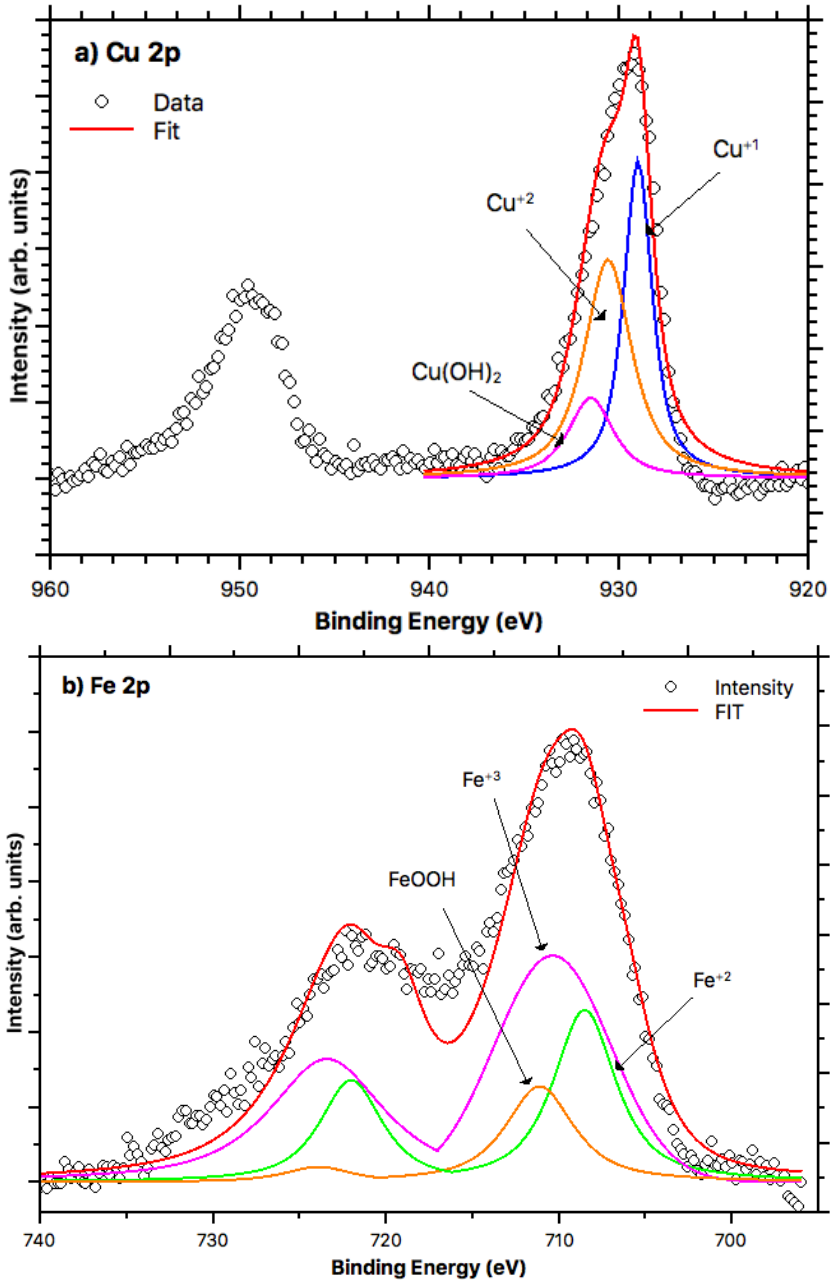


**Figure 4-13:** XPS High resolution scan of (a) Cu 2p and (b) Fe 2p lines for $CuFe_{0.75}Ga_{0.25}O_2$ 95 nm thickness (CFOCGO8) sample.

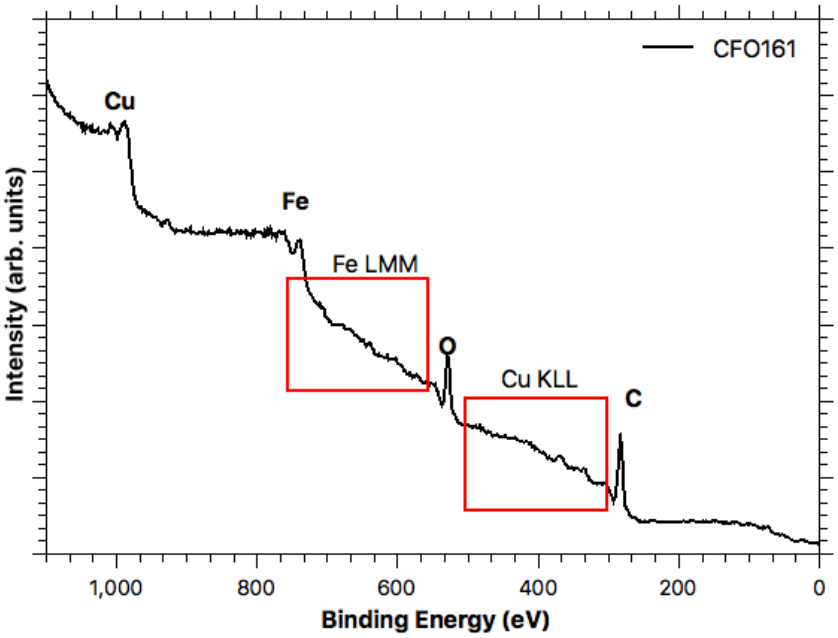


**Figure 4-14:** X-ray Photoelectron survey spectrum of $CuFeO_2$ 75 nm thickness (CFO161) sample with principal peaks identified.

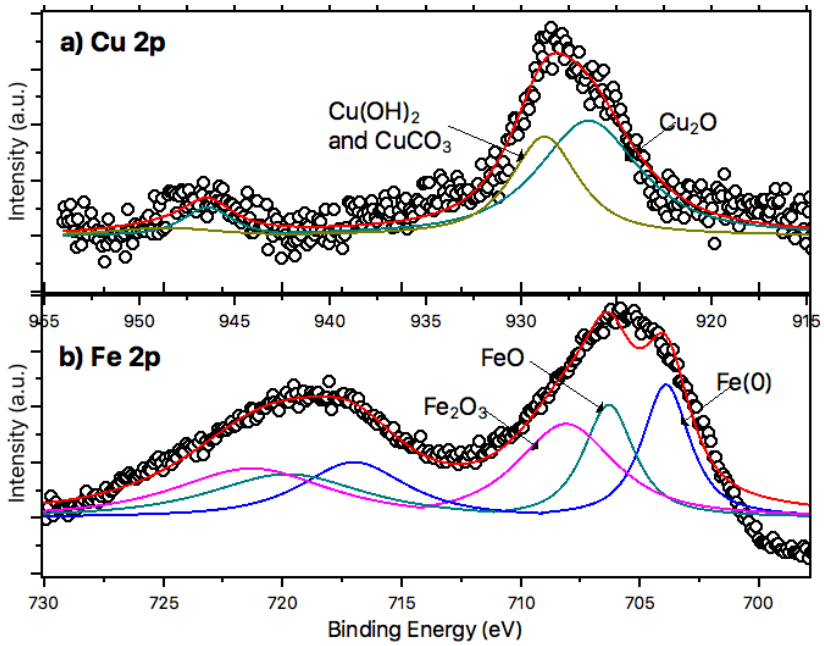


**Figure 4-15:** XPS High resolution scans for (a) Cu 2p and (b) Fe 2p peaks for CuFeO2 film 75 nm in thickness (CFO161) and peak fitting considering different oxidation states.

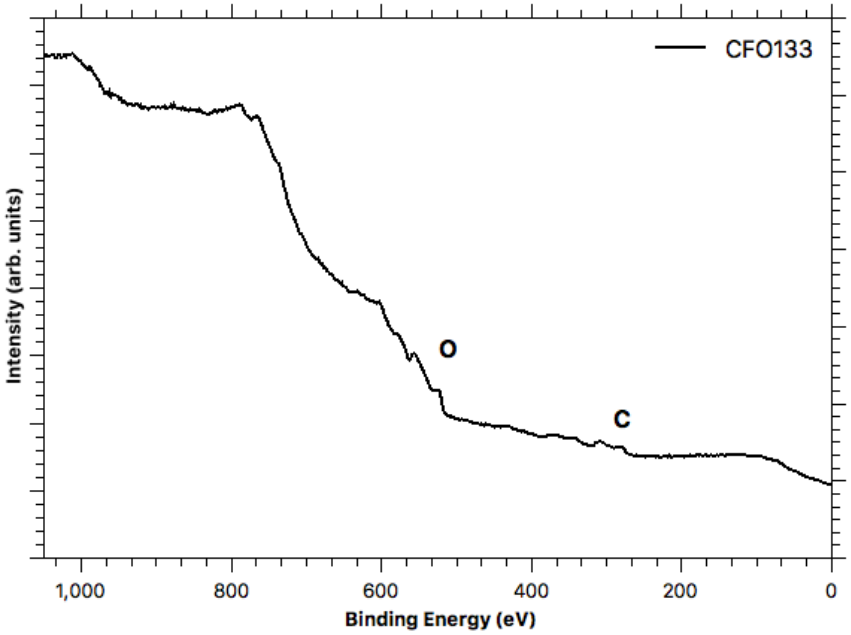


**Figure 4-16:** X-ray Photoelectron survey spectrum of $CuFeO_2$ 21 nm thickness (CFO133) sample with principal peaks identified.

# Appendix A.4. Thermal Programmed Desorption

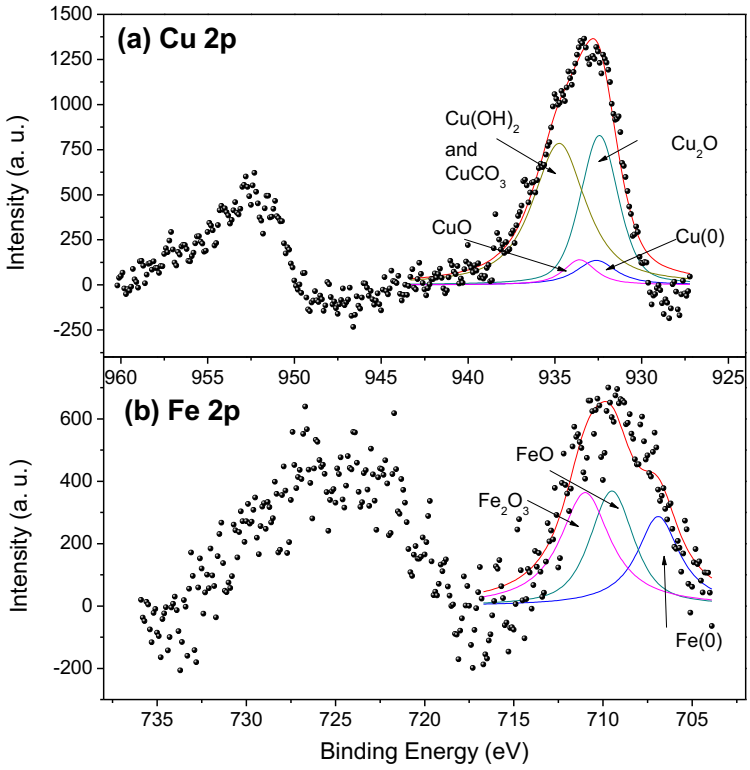


**Figure 4-17:** XPS high resolution spectra of (a) Cu 2p and (b) Fe 2p after $CO_2$ exposure of $CuFe_{0.75}Ga_{0.25}O_2$ film 48 nm in thickness (CFOCGO7) sample.

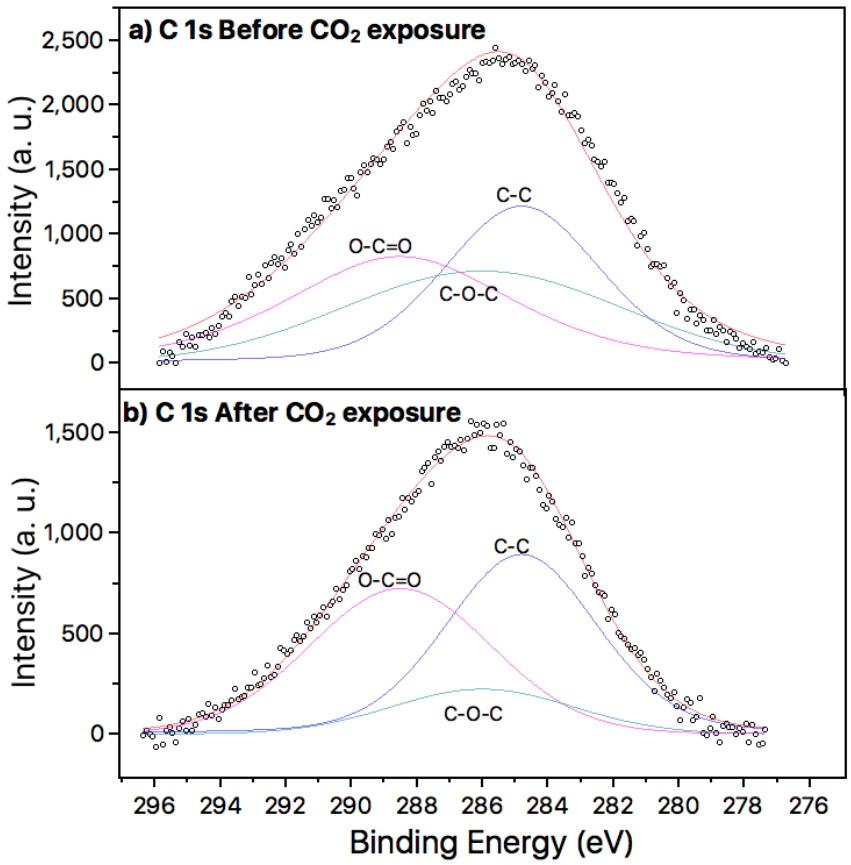


**Figure 4-18:** XPS measurements of C1s band for $CuFe_{0.75}Ga_{0.25}O_2$ 48 nm film (a) before and (b) after $CO_2$ exposure.

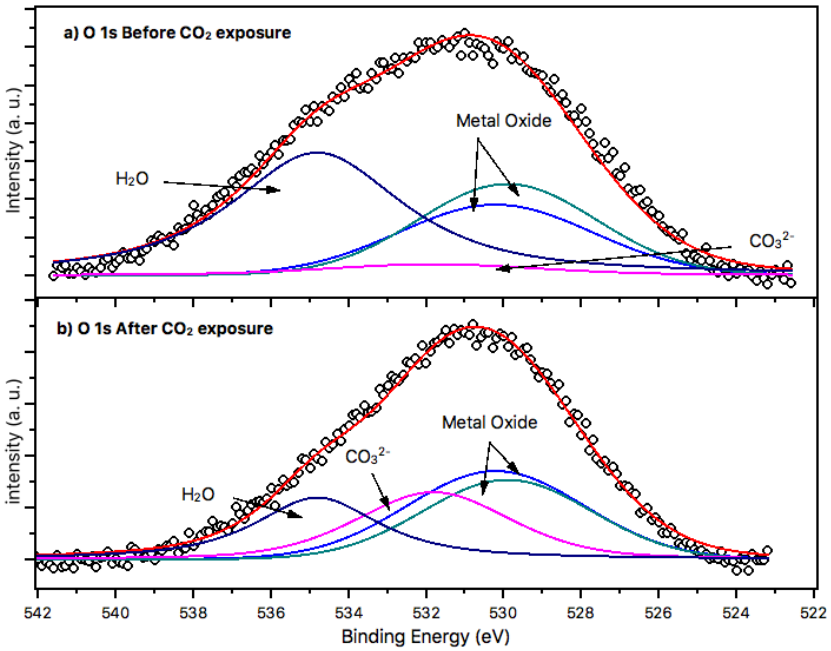


**Figure 4-19:** XPS measurements of O 1s band for $CuFe_{0.75}Ga_{0.25}O_2$ 48 nm film (a) before and (b) after $CO_2$ exposure.

# $H_2O$ TPD Fitting Parameters

| Composition | Code | Dosis (L) | Heating rate (K/s) | $E_1$ (eV/atom) | $T_p^1$ (K) | $E_2$ (eV/atom) | $T_p^2$ (K) | $R^2$ |
|---|---|---|---|---|---|---|---|---|
| $CuFeO_2$ | CFO161 | 1500 | 14.3±0.2 | 0.70±0.12 | 527.84±8.94 | 0.44±0.07 | 678.33±15.59 | 0.96 |
| | | 5000 | 6.9±0.1 | 0.28±0.01 | 633.59±7.97 | 2.05±0.50 | 742.92±4.90 | 0.90 |
| | | 5000 | 7.9±0.1 | 0.55±0.04 | 568.98±4.93 | 0.93±0.03 | 746.29±1.61 | 0.98 |
| | | 5000 | 13.1±0.3 | 0.36±0.02 | 628.37±5.23 | 2.24±0.35 | 781.90±3.28 | 0.98 |
| | CFO168 | 1500 | 14.5±0.3 | 0.29±0.01 | 533.35±3.28 | 1.93±0.32 | 715.06±4.02 | 0.98 |
| $CuFe_{0.75}Ga_{0.25}O_2$ | CFOCGO7 | 1500 | 41.5±0.5 | 0.46±0.11 | 595.47±31.02 | 0.53±0.16 | 816.53±23.41 | 0.84 |
| | | 5000 | 25.4±0.7 | 0.34±0.02 | 649.14±15.83 | 1.03±0.17 | 780.30±3.75 | 0.98 |
| | CFOCGO8 | 1500 | 17.2±0.3 | 0.53±0.02 | 478.62±1.74 | 0.98±0.05 | 701.40±2.53 | 0.97 |

**Table 4-3**: Fitting parameters for $H_2O$ TPD spectra on selected samples.

# $CO_2$ TPD Fitting Parameters

| Composition | Code | Dosis (L) | Heating rate (K/s) | $E_1$ (eV/atom) | $T_p^1$ (K) | $E_2$ (eV/atom) | $T_p^2$ (K) | $R^2$ |
|---|---|---|---|---|---|---|---|---|
| $CuFeO_2$ | CFO161 | 1500 | 14.3±0.2 | 0.48±0.32 | 574.79±78.80 | 0.38±0.55 | 728.47±222.97 | 0.75 |
| | | 5000 | 6.9±0.1 | 0.28±0.03 | 607.06±6.18 | 1.95±0.16 | 918.13±2.68 | 0.84 |
| | | 5000 | 7.9±0.1 | 0.17±0.04 | 734.88±51.43 | 1.47±0.09 | 723.49±2.12 | 0.92 |
| | | 5000 | 13.1±0.3 | 0.30±0.03 | 679.55±21.51 | 2.14±0.31 | 785.64±2.48 | 0.97 |
| | CFO168 | 1500 | 14.5±0.3 | 0.35±0.01 | 498.01±1.83 | 2.13±0.11 | 716.18±1.41 | 0.97 |
| $CuFe_{0.75}Ga_{0.25}O_2$ | CFOCGO7 | 1500 | 41.5±0.5 | 0.65±0.23 | 660.00±15.84 | 0.30±0.21 | 800.00±275.23 | 0.86 |
| | | 5000 | 25.4±0.7 | 0.67±0.04 | 613.07±4.72 | 0.59±0.09 | 789.05±11.83 | 0.97 |
| | CFOCGO8 | 1500 | 17.2±0.3 | 0.31±0.03 | 490.71±6.25 | 0.98±0.06 | 721.27±2.72 | 0.94 |

**Table 4-4:** Fitting parameters for $CO_2$ TPD spectra on selected samples.

# CO TPD Fitting Parameters

| Composition | Code | Dosis (L) | Heating rate (K/s) | $E_1$ (eV/atom) | $T_p^1$ (K) | $E_2$ (eV/atom) | $T_p^2$ (K) | $R^2$ |
|---|---|---|---|---|---|---|---|---|
| $CuFeO_2$ | CFO161 | 1500 | 14.3±0.2 | 0.53±0.04 | 613.47±7.47 | 1.00±0.18 | 786.07±9.14 | 0.96 |
| | | 5000 | 6.9±0.1 | 0.53±0.05 | 566.28±6.14 | 1.04±1.46 | 824.20±11.98 | 0.80 |
| | | 5000 | 7.9±0.1 | 1.32±1.28 | 536.09±21.94 | 1.05±0.05 | 764.11±2.87 | 0.88 |
| | | 5000 | 13.1±0.3 | 0.46±0.06 | 663.08±13.74 | 2.06±0.19 | 790.54±1.77 | 0.97 |
| | CFO168 | 1500 | 14.5±0.3 | 0.36±0.03 | 537.66±5.70 | 2.34±0.32 | 723.53±3.07 | 0.98 |
| $CuFe_{0.75}Ga_{0.25}O_2$ | CFOCGO7 | 1500 | 41.5±0.5 | 0.63±0.06 | 634.51±9.01 | 2.61±1.58 | 727.58±9.08 | 0.95 |
| | | 5000 | 25.4±0.7 | 0.59±0.05 | 643.37±7.58 | 1.28±0.18 | 779.06±6.16 | 0.97 |
| | CFOCGO8 | 1500 | 17.2±0.3 | 0.33±0.05 | 489.59±8.33 | 0.82±0.07 | 742.52±4.46 | 0.86 |

**Table 4-5:** Fitting parameters for CO TPD spectra on selected samples.

# Appendix B. Gas adsorption and catalysis

It is generally considered that there are three states of matter, solid, liquid and gas, although each of these can be further refined or subdivided. In general, most chemical reaction occurs at either liquid or gas phase even though there are also many reactions that occurs at solid phase. However, it is common to recognize that many reactions occur on the interface between two or more phases, for example the formation of gas bubbles in a liquid. When a surface is unsaturated it has energy and this energy can contribute to the allover energy changes occurring when a process occurs at the surfaces, whether this process is purely a physical interaction or a chemical reaction. The study of the chemical phenomena in such surfaces involve the study of adsorption and reactions of molecules at solid surfaces.

When a reaction at a surface leads to a new surface entity that desorbs to give products and results in the regeneration of the surface, we have a catalytic process. In order to understand a catalytic process, we should have a good understanding of the phenomena of adsorption and, to a lesser extent, desorption.

Let's consider the following homogeneous reaction described in equation (4-1)

$$A + B \rightleftarrows C + D. \qquad (4\text{-}1)$$

As written, this equation represents an equilibrium situation in which species A reacts with species B reversibly to give species C and D. The equilibrium position for the reaction is determined by thermodynamics and, once equilibrium is achieved, the rates of the forward and reverse reactions are equal. The energetics of the process are shown schematically in Figure 4-20.

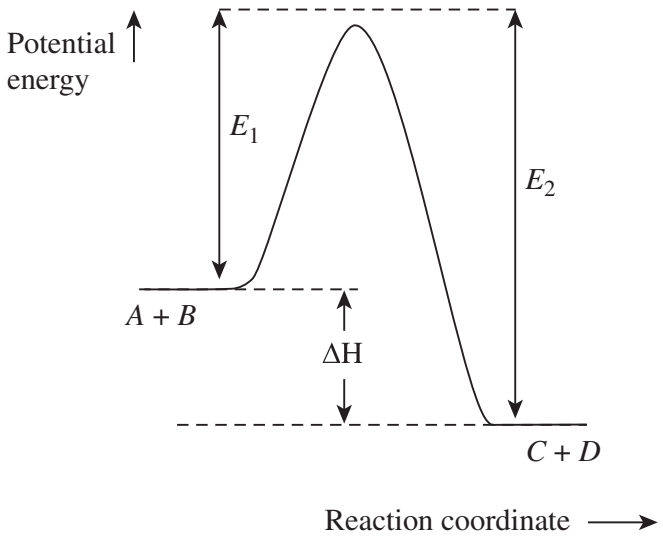


**Figure 4-20:** Energetics of the reaction: $\boldsymbol{A + B \rightarrow C + D}$

In this figure, the reaction is shown as being exothermic ($\Delta H < 0$) but it could equally well have been shown as being endothermic. In order to transform into the products C and D, the reactants A and B must come together to form an activated (or transition state) complex $(AB)^{\ddagger}$ which then decomposes to form the products. The activation energy for the formation of the complex is $E_1$ and this has a numerical value well above the average thermal energy of the molecules A and B. Once C and D are formed, they can transfer back to A and B by the reverse process, the activation energy for that change being $E_2$.

We now consider the situation when A and B are reacted in the presence of a solid surface which will adsorb both A and B. As shown in equation (4-2), the adsorbed species $A_{ads}$ and $B_{ads}$ may then transform on the surface to give $C_{ads}$ and $D_{ads}$ and these can in turn desorb to give the gaseous products C and D:

$$A + B \xrightarrow{1} A_{ads} + B_{ads} \xrightarrow{2} (AB)^{\ddagger}_{ads} \xrightarrow{3} C_{ads} + D_{ads} \xrightarrow{4} C + D. \qquad (4\text{-}2)$$

In this situation, the presence of the solid surface will generate the adsorbed species (first reaction in equation (4-2)), in this process as the molecules begins to get closer to the surface, Van der Waals attractive forces occur and the molecule becomes "physically adsorbed" (i.e. held by physical forces of attraction, $\Delta H_p$) at a distance from the surface corresponding to the sums of the Van der Waals radii, if the molecules approaches the surface any more closely, there will be a strong repulsion between the electron clouds of the molecule and the surface. If then the molecules are attracted by an even stronger force, they can become in to adsorbed molecules with a heat of adsorption $-\Delta H_C$ (chemisorption curve). It can be seen in Figure 4-21 that the chemisorption curve intersects the physical adsorption curve at a value below or very close to the zero of the energy axis, this means that the chemisorption process does not have an activation energy barrier.

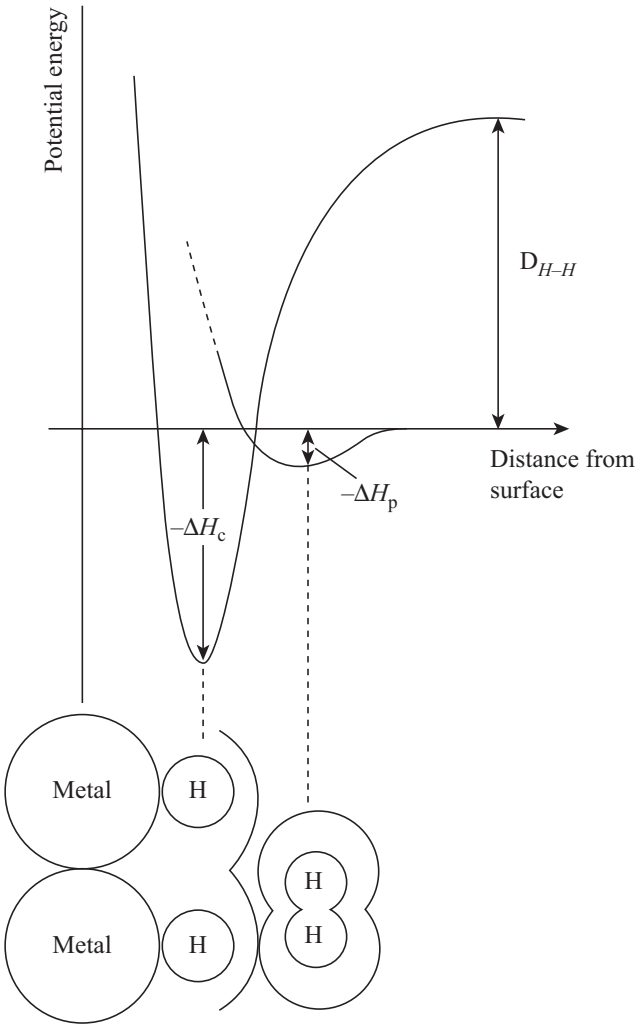


**Figure 4-21:** LennardeJones potential energy diagram for the adsorption of hydrogen on a metal surface; as the hydrogen molecule approaches the surface from the right-hand side, it becomes physically adsorbed and then, following dissociation in the region of the Surface.

Considering adsorption potentials, the situation described in equation (4-2) can be represented schematically as in Figure 4-22, in which, for simplification, single energy troughs are shown for $A_{ads}$ and $B_{ads}$ and for $C_{ads}$ and $D_{ads}$ and a single step is shown for the inter-conversion to the adsorbed products. Two curves are shown in the figure. Curve (i) represents the situation in which both A and B adsorb without any activation energy for the adsorption step while curve (ii) represents a situation in which there is an

activation energy for the adsorption of A and B. Once A and B are adsorbed, they can transfer, via an adsorbed complex $(AB)^{\ddagger}_{ads}$, to give adsorbed C and D and these surface species then desorb to give products [58].

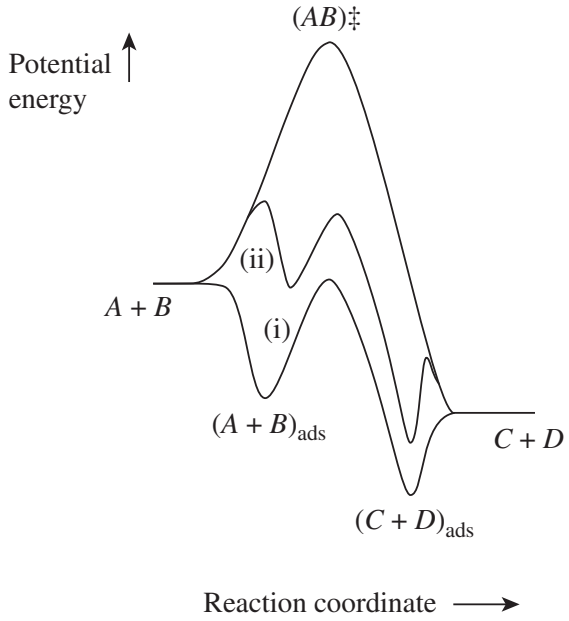


**Figure 4-22:** schematic representation of the catalyzed reaction: $\boldsymbol{A + B \rightarrow C + D}$

# Appendix C. Kinetics of Desorption

## Appendix C.1. Rate Equation

Suppose we have a reaction between three elements, with concentrations [A], [B] and [C], which are related by the reaction described in (4-3),

$$a[A] + b[B] \rightarrow c[C]. \tag{4-3}$$

One way to describe the velocity of this reaction is to calculate the change in time of the concentration of any of the elements, as in (4-4),

$$v = -\frac{1}{a}\frac{d[A]}{dt} = -\frac{1}{b}\frac{d[B]}{dt} = \frac{1}{C}\frac{d[C]}{dt}. \quad (4\text{-}4)$$

A second form to describe this velocity, is use an empirical relation commonly known as the velocity law, which is written as in the equation (4-5),

$$v = k[A]^x[B]^y, \quad (4\text{-}5)$$

where $k$, $x$ and $y$, are constants that need to be found experimentally. The order of the reaction $n$ is then defined as

$$n = x + y. \quad (4\text{-}6)$$

The constant has a temperature dependence following an Arrhenius law, so can be written as

$$k(T) = \upsilon_n e^{-E/k_b T}, \quad (4\text{-}7)$$

where $E$ is the activation energy and the constant pre-exponential factor. If we define σ as the concentration per unit area [molecules/cm$^2$] desorbed, the desorption rate $N$ is obtained as

$$N(t) = -\frac{d\sigma}{dt} = \upsilon_n \sigma^n e^{-E/k_b T}. \quad (4\text{-}8)$$

Normally solve this equation for is not easy, because we have a time dependence both in $\sigma^n$ and in $T$ during a desorption process [59].

## Appendix C.2. Thermal Programmed Desorption of gases

To study a desorption process, as it was described in Appendix C.1, we need to solve the equation (4-8) to find $\sigma(t)$, and for that we need to know the time dependence of the temperature $T(t)$. In most of the theoretical descriptions there are two different time dependencies for temperature normally used; one linear and one reciprocal, both developed by P. A. Redhead in 1962 [52]. In these two cases, it is possible to solve the equation (4-8) and find an analytical expression for $\sigma(t)$, because perform the experiments is easier using the linear type, we will be focused only on this case.

To start, we replace a linear dependence in equation (4-9) into the rate equation (4-8), to obtain the relation (4-10),

$$T(t) = T_0 + \beta t, \tag{4-9}$$

$$N(t) = \upsilon_n \sigma^n e^{-E/k_b(T_0+\beta t)}, \tag{4-10}$$

where $T_0$ is the initial temperature of the linear ramp and β is the temperature rate. Then, we derivate this relation to find the temperature where the desorption rate is maximal ($T_P$),

$$\frac{E}{k_B T_p^2} \upsilon_n \sigma^n \beta + n\upsilon_n \sigma^{n-1} \frac{d\sigma}{dt} = 0. \tag{4-11}$$

If we use again (4-8) a relation for the maximal desorption temperature (4-12) is found,

$$\frac{E}{k_B T_p^2} = \frac{n\upsilon_n \sigma^{n-1}}{\beta} e^{-E/k_B T_P}. \tag{4-12}$$

This is an important expression, because it relates physical parameters of a desorption that characterizes it, as the activation energy, the order, the pre-exponential factor and the temperature for maximal desorption, with a parameter that can be controlled during the experiments; the temperature rate β.

The shape of desorption rates can also be approximated when the temperature is changed lineally. For this, the equation (4-8) is integrated for the special cases with $n = 1$ and $n = 2$. The relations (4-13) and (4-14) shown below correspond to a first and second order desorption, respectively.

$$\ln\left(\frac{N_P}{N(T)}\right) = \frac{E}{k_B}\left(\frac{1}{T} - \frac{1}{T_P}\right) + \left(\frac{T}{T_P}\right)^2 e^{-\frac{E}{k_B}\left(\frac{1}{T}-\frac{1}{T_P}\right)} - 1, \qquad (4\text{-}13)$$

$$\frac{N_P}{N(T)} = \frac{1}{4}\left[e^{\frac{E}{2k_B}\left(\frac{1}{T}-\frac{1}{T_P}\right)} + \left(\frac{T}{T_P}\right)^2 e^{-\frac{E}{2k_B}\left(\frac{1}{T}-\frac{1}{T_P}\right)}\right]^2, \qquad (4\text{-}14)$$

where the constant $N_P$ represents the desorption rate at $T_P$. With the assumption that T is near to $T_P$ $(T/T_P \sim 1)$, $N(T)$ becomes an asymmetric function of temperature, around $T_P$, when $n = 1$, instead of the case with $n = 2$, where it is symmetric because

$$\frac{N_P}{N(T)} \sim cosh^2\left(\frac{E}{2k_B}\left(\frac{1}{T} - \frac{1}{T_P}\right)\right). \qquad (4\text{-}15)$$

This is an important fact, because we can know if a desorption process is closer to a first or a second order one, just analyzing the form of the curve. In the Figure 1.2 we show a plot of the equations (4-13) and (4-14), using parameters found in the reference [52]. The differences around the center are clear.

Finally, from an experimental point of view, in a thermal program desorption process a sample is heated lineally under high vacuum conditions. Then, the partial pressure produced by the desorbed gas is measured, as a function of time or temperature. The curve obtained for the pressure will be proportional to the number of molecules desorbed, due to the ideal gases law (4-16).

$$P_{Chamber}\left(T_{Sample}\right) = \frac{N\left(T_{Sample}\right)k_B T_{Chamber}}{V}, \qquad (4\text{-}16)$$

where the volume $V$ and the temperature $T_{Chamber}$ are constants of the vacuum system.

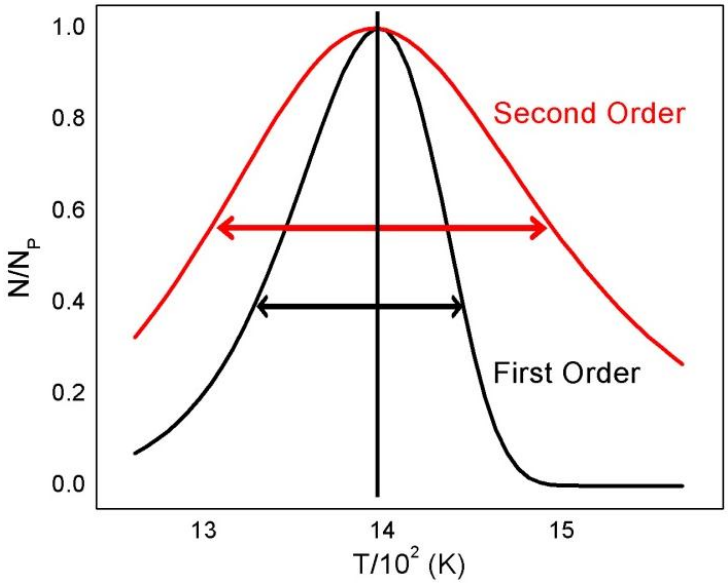


**Figure 4-23:** Normalized graphics of a first ($\boldsymbol{E = 91.5\ kcal/mol}$) and second order ($\boldsymbol{E = 87\ kcal/mol}$) desorption, using linear temperature rates ($\boldsymbol{T_P = 1400K}$). These numerical parameters represent the β-phase desorption of $N_2$ in W [52].

# Appendix D. Appendix A: Thermal desorption spectrum correction.

During thermal programmed desorption (TPD) experiments described in section 2.2.1, thermal desorption spectrum can be obtained for desired gas as it was discussed in section 3.2. The mean difficulty when trying to analyze this kind of plots is to clearly identify sample desorption from any other environmental contribution, such as sample holder. To do so, two corrections were performed during the analysis, first one is a technical correction related to cracking pattern of the mass spectrometer and the second one y related to sample holder and substrate desorption.

## Appendix D.1. Cracking Pattern correction.

During this work, we used a Residual Gas Analyzer from Stanford Research Instrument (SRS RGA 200), this mass spectrometer consisting of a quadrupole probe, and an Electronics Control Unit (ECU) which mounts directly on the probe's flange and contains all the necessary electronics for operating the instrument.

The total probe equipment consists of three parts: the **ionizer**, the **quadrupole filter** and the **ion detector**. These parts reside in the vacuum space where the gas analysis measurements are made.

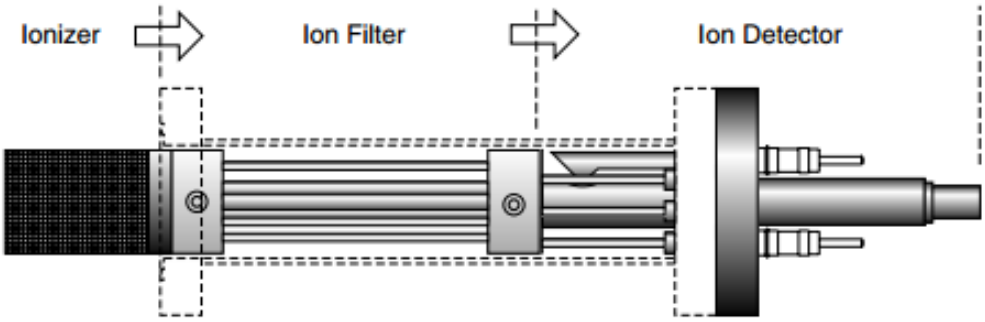


**Figure 4-24:** Schematic diagram of hardware of the mass spectrometer.

Positive ions are produced in the ionizer by bombarding residual gas molecules with electrons derived from a heated filament. The ions are then directed toward the entrance of the ion filter where they are separated based on their mass-to-charge ratio. Then, positive ions are transferred from the ionizer into the quadrupole where they are filtered according to their mass-to-charge ratios. Ions that successfully pass through the quadrupole are focused towards the detector by an exit aperture held at ground potential. Finally, the detector measures the ion currents directly (Faraday Cup) or, using an optional electron multiplier detector, measures an electron current proportional to the ion current [60].

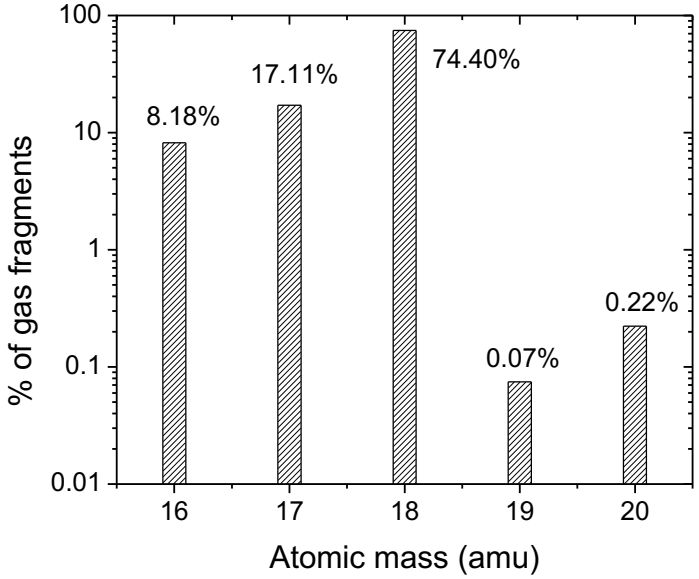


**Figure 4-25:** Gas fragmentation pattern of water obtained from RGA library.

During this procedure ions can be cracked, this cracking implies that when detecting a single gas, there is a well-defined group of mases that can be detected, in the case of water (see Figure 4-25) 18 amu will be the main mass detected but it only correspond to 74.4% of the total water molecules available because the resting 25.6% has been fragmented according to the pattern showed in Figure 4-25.

The same analysis can be performed for most gases, in our case we are interested in $CO_2$, CO and $H_2O$. As shown in Figure 4-26 $CO_2$ has a gas fragment in 28 amu corresponding to 8.63% of its total and this fragmentation gas has the same atomic mass of CO mean fragment.

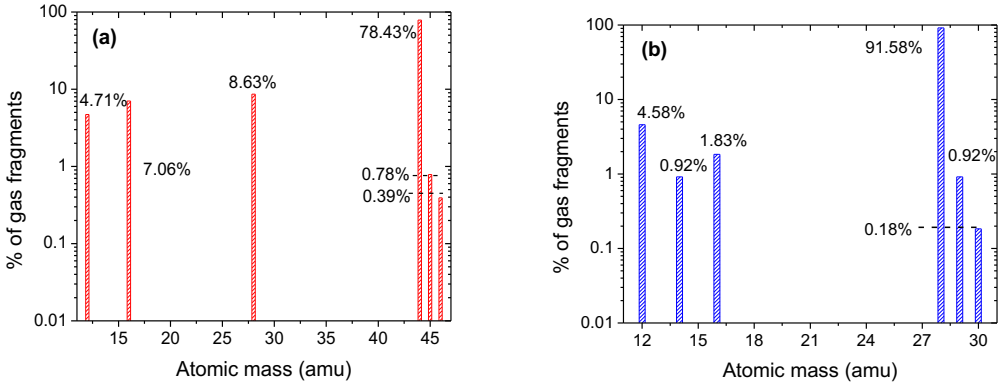


**Figure 4-26:** Gas fragmentation pattern for (a) $CO_2$ and (b) CO gases obtained from RGA software library.

In order to determine the real intensity of the signal detected of each gas, a mathematical correction was performed using information from cracking patterns of CO, $CO_2$ and $H_2O$ and assuming no interference between each gas (i.e. partial pressure of different fragmented gas will be summed if they have equal atomic mass). This correction is represented by equations (4-17), (4-18) and (4-19).

$$28Amu_{PP} = 0.086275\ CO_2 + 0.915751\ CO \tag{4-17}$$

$$18Amu_{PP} = 0.744048\ H_2O \tag{4-18}$$

$$44Amu_{PP} = 0.784314\ CO_2 \tag{4-19}$$

## Appendix D.2. Sample holder desorption subtraction.

When performing a fast desorption, not only the sample is heated up but also the sample holder is heated up. In order to correctly identify desorbed gases from sample only, TPD experiments were also performed with the sample holder and a clean $Al_2O_3$ (001) substrate.

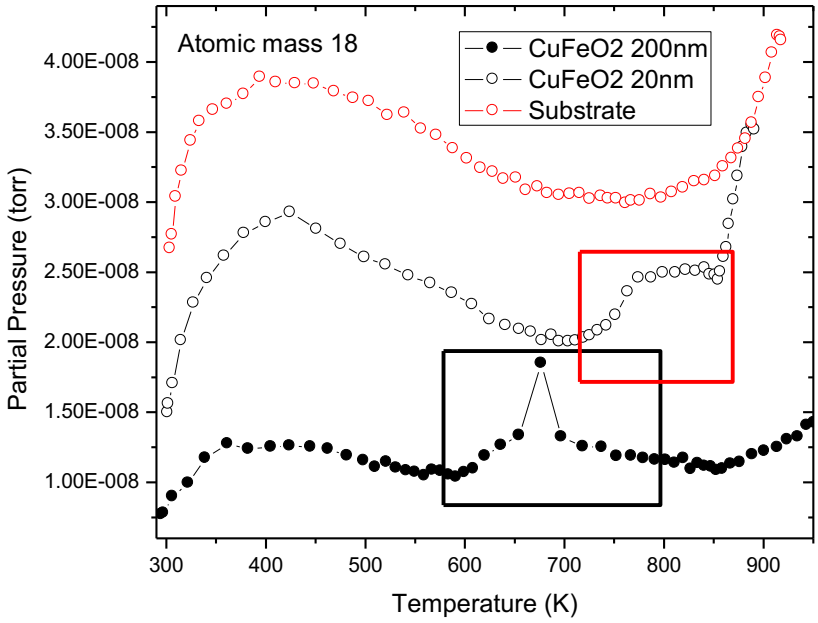


**Figure 4-27:** Thermal desorption spectra comparison for $CuFeO_2$ samples and substrate for water desorption.

Using data obtained from substrate and sample holder was possible to distinguish samples desorption peaks, as showed in Figure 4-27.

# Appendix E. X-ray Photoelectron Spectroscopy (XPS)

X-ray photoelectron spectroscopy (XPS) is a surface-sensitive quantitative spectroscopic technique that measures the elemental composition at the parts per thousand range, empirical formula, chemical state and electronic state of the elements that exist within a material. XPS spectra are obtained by irradiating a material with a beam of X-rays while simultaneously measuring the kinetic energy and number of electrons that escape from the top 0 to 10 nm of the material being analyzed. XPS requires high vacuum ($P \sim 10^{-8}$ millibar) or ultra-high vacuum (UHV; $P < 10^{-9}$ millibar) conditions, although a current

area of development is ambient-pressure XPS, in which samples are analyzed at pressures of a few tens of millibar.

Because the energy of an X-ray with particular wavelength is known (for Al $K_\alpha$ X-rays, $E_{photon}$ = 1486.7 eV), and because the emitted electrons' kinetic energies are measured, the electron binding energy of each of the emitted electrons can be determined by using an equation that is based on the work of Ernest Rutherford (1914):

$$E_{binding} = E_{photon} - (E_{kinetic} + \phi) \quad (4\text{-}20)$$

where $E_{binding}$ is the binding energy (BE) of the electron, $E_{photon}$ is the energy of the X-ray photons being used, $E_{kinetic}$ is the kinetic energy of the electron as measured by the instrument and $\phi$ is the work function dependent on both the spectrometer and the material. This equation is essentially a conservation of energy equation. The work function term $\phi$ is an adjustable instrumental correction factor that accounts for the few eV of kinetic energy given up by the photoelectron as it becomes absorbed by the instrument's detector. It is a constant that rarely needs to be adjusted in practice.

In this work, we used a high vacuum system composed by a stainless-steel chamber which was custom made by MDC Vacuum Inc. of approximately $4 \times 10^{-2}$ $m^2$, pumped by an Adixen 0.15 $m^3/s$ Turbo pump (ATP150), backed by an Adixen 20.7 $m^3/h$ dual stage rotatory pump (Pascal 2021C1). X-ray were produced using a STAIB RQ300X X-ray source (1) using Mg Kα x-radiation and electrons were detected using a STAIB DESA100 electron spectrometer (2) facing the sample holder (3).

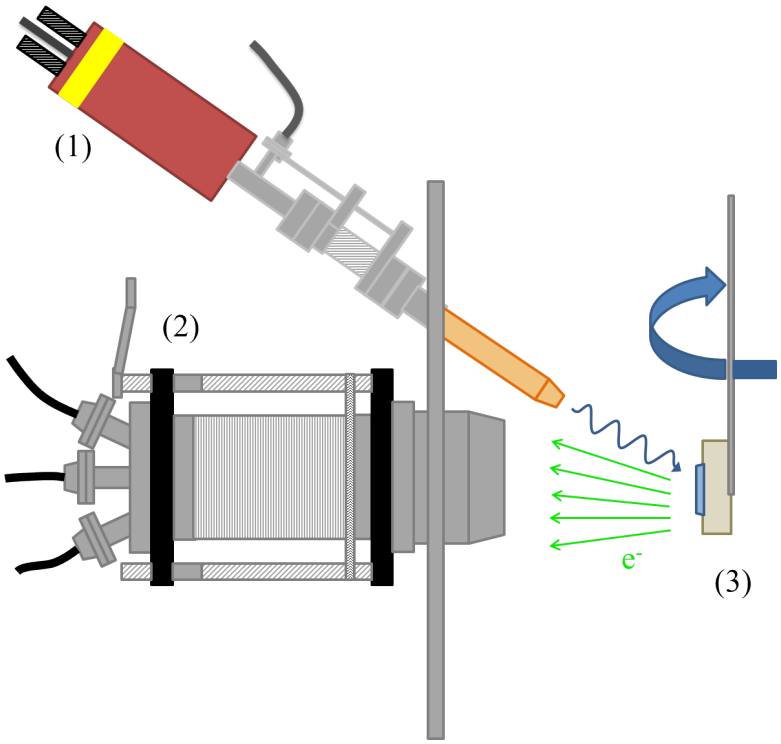


**Figure 4-28:** schematic diagram of the XPS system used for this work

# Appendix F. X-ray Diffraction (XRD) and Grazing Incidence Diffraction (GID)

Two important techniques based on x-rays interaction with solids will be detailed in this appendix; X-Ray Diffraction (XRD) and Gracing Incident X-Ray Diffraction (GID).

Depending on the atom, x-ray emissions will have different energies due to the specific electronic energy levels of the material. In our measurements, radiation from copper was used to perform XRD and GID measurements. In Table 4-6 we show the wavelength of the principal x-rays emitted by this atom.

| Transition | Wavelength (nm) |
|---|---|
| Kα (average) | 0.154184 |
| Kα1 | 0.154439 |
| Kα2 | 0.154056 |
| Kβ | 0.139222 |

**Table 4-6 :** Principal x-rays wavelength produced by a copper source. These x-rays were used in our study.

As is observed from the table, the x-ray wavelengths are in the order of the Å. This is very important, because the basic idea of XRD and GID techniques is to produce the x-ray diffraction on the crystal structure of a solid. Therefore, it is essential to use radiation having a wavelength of the same order as the average distance between the atoms of the solid.

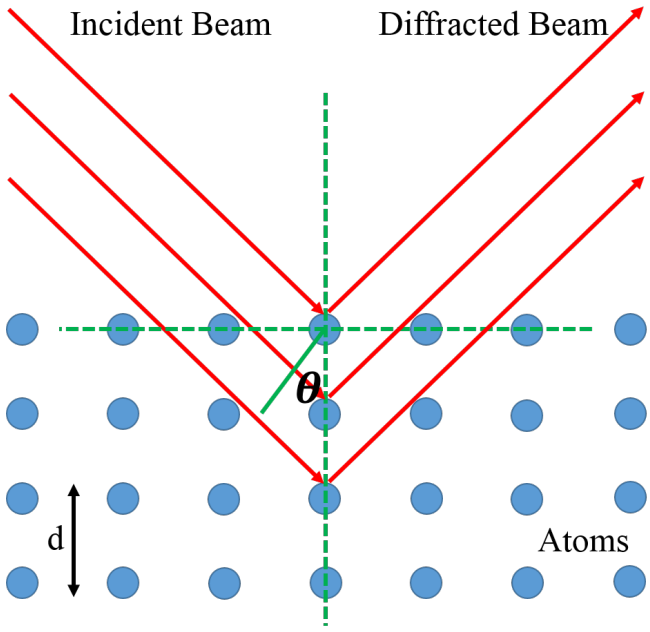


**Figure 4-29:** Scheme of diffraction produced in x-rays by a crystalline structure. The distance between the atoms d and diffraction angle θ are related by the Braggs law.

When X-rays reach a solid, they are diffracted due to the periodic structure of the material, as in a diffraction grating (Figure 4-29). If (h, k, l) are denoted as the Miller indexes of the crystallographic structure [61], d the distance between the atoms and λ the wavelength of the x-rays, the angles θ where the diffracted intensity is maximal follows the Bragg relation expressed as the equation (4-21),

$$2d(h,k,l)\sin\theta = \lambda \qquad (4\text{-}21)$$

It is worth to note that for each distance d, with a different set of Miller indexes, equation (4-21) gives a set of diffraction angles. Therefore, in XRD and GID measurements, an x-ray beam is directed to a sample and the angles θ where the diffracted intensity is maximal are detected. The difference between both techniques is the depth from where the information comes from. In XRD, x-ray source and detector are moved to measure the angles θ, while in GID, the x-ray source is keep at a constant small angle α, moving only the detector. A simpler schematic representation of these differences is shown in Figure 4-30. When the angle of the source is small, the incidence of the x-rays is always grazing, and therefore diffraction is preferentially from the surface [62].

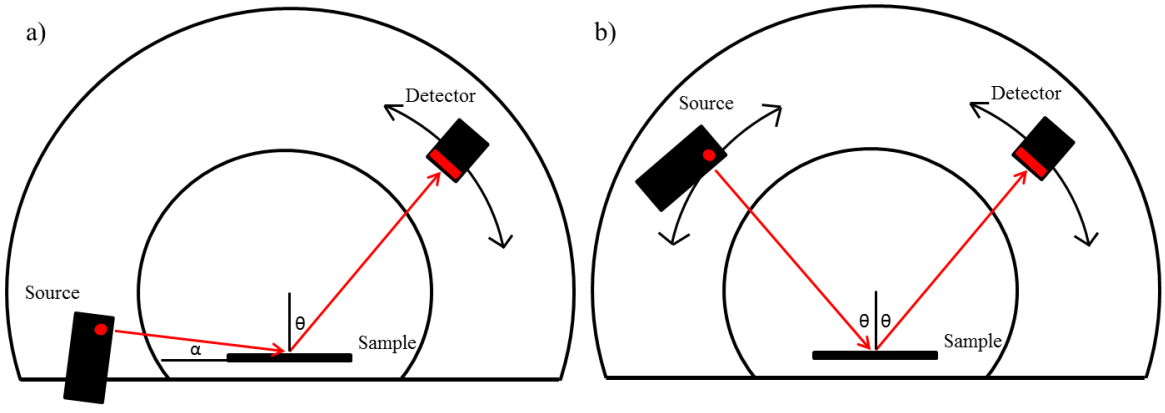


**Figure 4-30:** Differences between GID (a) and XRD (b) setups. In GID the x-ray source is keep at a constant small angle α, while in XRD source and detector are moved.

XRD is a technique generally used for determining for determining atomic and molecular structure of a crystal, instead GID as uses small incidence angles it is a diffraction surface sensitive and is used for study surfaces and layers because wave penetration is limited.

# Appendix G. Raman Spectroscopy

Raman spectroscopy, named after Sir C. V. Raman who discovered this effect on 1928, is a spectroscopic technique used to observe vibrational, rotational, and other low-frequency modes in a system [63]. Raman spectroscopy is commonly used in chemistry to provide a structural fingerprint by which molecules can be identified.

It relies on inelastic scattering, or Raman scattering, of monochromatic light, usually from a laser in the visible, near infrared, or near ultraviolet range. The laser light interacts with molecular vibrations, phonons or other excitations in the system, resulting in the energy of the laser photons being shifted up or down. The shift in energy gives information about the vibrational modes in the system. Infrared spectroscopy yields similar, but complementary, information.

The Raman effect occurs when electromagnetic radiation interacts with a solid, liquid, or gaseous molecule's polarizable electron density and bonds. The spontaneous effect is a form of inelastic light scattering, where a photon excites the molecule in either the ground (lowest energy) or excited rovibronic state (a rotational and vibrational energy level within an electronic state). This excitation puts the molecule into a virtual energy state for a short time before the photon scatters in elastically. Inelastic scattering means that the scattered photon can be of either lower or higher energy than the incoming photon, compared to elastic, or Rayleigh, scattering where the scattered photon has the same energy as the incoming photon. After interacting with the photon, the molecule is

in a different rotational or vibrational state. This change in energy between the initial and final rovibronic states causes the scattered photon's frequency to shift away from the excitation wavelength (that of the incoming photon), called the Rayleigh line.

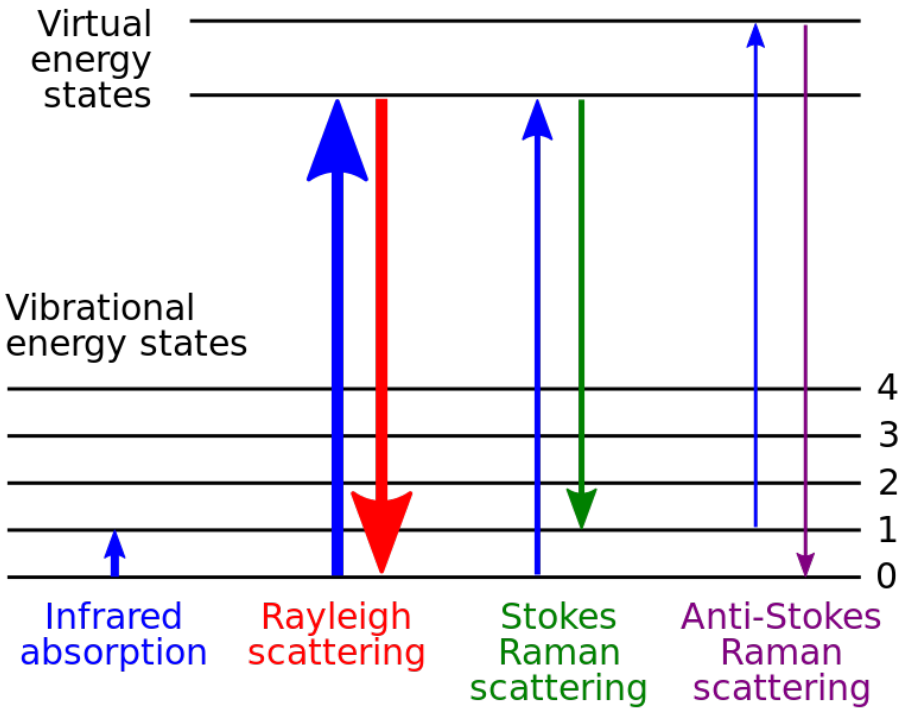


**Figure 4-31:** Possible electronic transitions due to interactions between photon and molecule

Typically, a sample is illuminated with a laser beam. Electromagnetic radiation from the illuminated spot is collected with a lens and sent through a monochromator. Elastic scattered radiation at the wavelength corresponding to the laser line (Rayleigh scattering) is filtered out by either a notch filter, edge pass filter, or a band pass filter, while the rest of the collected light is dispersed onto a detector.

Spontaneous Raman scattering is typically very weak, and as a result the main difficulty of Raman spectroscopy is separating the weak inelastically scattered light from the intense Rayleigh scattered laser light. Historically, Raman spectrometers used

holographic gratings and multiple dispersion stages to achieve a high degree of laser rejection. In the past, photomultipliers were the detectors of choice for dispersive Raman setups, which resulted in long acquisition times. However, modern instrumentation almost universally employs notch or edge filters for laser rejection and spectrographs either axial transmissive (AT), Czerny–Turner (CT) monochromator, or FT (Fourier transform spectroscopy based), and CCD detectors.

# Appendix H. : Tauc Equation

When working with semiconductors it is important to determine the semiconductor band gap, in this way one of the commonly used techniques is to determine optical bandgap trouch the Tauc equation. This method was developed by Jan Tauc who showed that the optical absorption spectrum of amorphous germanium resembles the spectrum of the indirect transitions in crystalline germanium (plus a tail due to localized states at lower energies), and proposed an extrapolation to find the optical gap of these crystalline-like states [64]. In this proposal, optical band gap ($E_g$) is related to optical absorbance ($\alpha$) as follows:

$$\alpha h\nu = b\left(h\nu - E_g\right)^n, \tag{4-22}$$

where $h$ is the Plank constant, $\nu$ corresponds to the incident wave frequency, $\alpha$ is the absorption coefficient, $b$ is a proportionality constant and $n$ is an arbitrary index that allows the linearization of the equation. The value of the exponent $n$ denotes the nature of the transition: [65]

- n = 1/2 for direct allowed transitions
- n = 3/2 for direct forbidden transitions.
- n = 2 for indirect allowed transitions

- n = 3 for indirect forbidden transitions

the main difficulty when trying to determine the optical bandgap trough this method is to properly determine the absorption coefficient *α*. When working optical transmittance spectroscopy, the absorption coefficient can be determined by the Beer Lambert law described by equation (4-23):

$$T = T_0 \cdot e^{\alpha \cdot x}, \tag{4-23}$$

where *T* is the absolute transmittance of the layer, $\alpha$ the absorption coefficient and *x* the thickness of the layer. Meanwhile if we are working with diffuse reflection, the absorption coefficient can be determined using the Kubelka Munk method that relates the reflection coefficient with the absorption coefficient. This method is described by the equation (4-24)

$$F(R) = \frac{1-R^2}{2R} = \frac{\alpha}{S}, \tag{4-24}$$

Where *R* is absolute reflectance of the layer, $\alpha$ the absorption coefficient and *S* the scattering coefficient.

# References


[1] BP: Statistical Review of World Energy, Workbook (xlsx), London, 2016

[2] CAIT Climate Data Explorer. 2015. Washington, DC: World Resources Institute. Available online at: http://cait.wri.org

[3] GISTEMP Team, 2016: GISS Surface Temperature Analysis (GISTEMP). NASA Goddard Institute for Space Studies. Dataset accessed 20YY-MM-DD at http://data.giss.nasa.gov/gistemp/.

[4] Hansen, J., R. Ruedy, M. Sato, and K. Lo, 2010: Global surface temperature change, Rev. Geophys., 48, RG4004, doi:10.1029/2010RG000345.

[5] Louis Schlapbach, Andreas Züttel (2001), *Hydrogen-storage materials for mobile applications*, NATURE, vol. 414 (6861), 353 – 358.

[6] Thomas, C. E. (2009). *Fuel cell and battery electric vehicles compared.* international journal of hydrogen energy, 34(15), 6005-6020.

[7] IEA. *Prospects for hydrogen and fuel cells*. En: serie de análisis tecnológico de energía. París: *International Energy Agency*; 2006.

[8] Andrews, J., & Shabani, B. (2012). *Re-envisioning the role of hydrogen in a sustainable energy economy*. International journal of hydrogen energy, 37(2), 1184-1203.

[9] Ogden, J. M. (1999). Prospects for building a hydrogen energy infrastructure. Annual Review of Energy and the Environment, 24(1), 227-279.

[10] HEAD, J., & TURNER, J. (2007). ANALYSIS OF THE WATER-SPLITTING CAPABILITIES OF GALLIUM INDIUM PHOSPHIDE NITRIDE (GaInPN). A Message from the Under Secretary for Science

[11] Navarro Yerga, R. M., Álvarez Galván, M. C., Del Valle, F., Villoria de la Mano, J. A., & Fierro, J. L. (2009). Water Splitting on Semiconductor Catalysts under Visible-Light Irradiation. ChemSusChem, 2(6), 471-485.

[12] Navarro, R. M., Del Valle, F., de la Mano, J. V., Álvarez-Galván, M. C., & Fierro, J. L. G. (2009). Photocatalytic water splitting under visible light: concept and catalysts development. Advances in chemical engineering, 36, 111-143.

[13] Schimmel, H. G., Kearley, G. J., Nijkamp, M. G., Visser, C. T., de Jong, K. P., & Mulder, F. M. (2003). Hydrogen adsorption in carbon nanostructures: comparison of nanotubes, fibers, and coals. Chemistry–A European Journal, 9(19), 4764-4770

[14] Sivula, K., & Van De Krol, R. (2016). Semiconducting materials for photoelectrochemical energy conversion. Nature Reviews Materials, 1, 15010.

[15] Boddy, P. J. (1968). Oxygen evolution on semiconducting TiO2. Journal of The Electrochemical Society, 115(2), 199-203.

[16] Fujishima, A., & Honda, K. (1972). Electrochemical photolysis of water at a semiconductor electrode. nature, 238(5358), 37-38.

[17] Woodhouse, M., & Parkinson, B. A. (2009). Combinatorial approaches for the identification and optimization of oxide semiconductors for efficient solar photoelectrolysis. Chemical Society Reviews, 38(1), 197-210.

[18] McLeod, J. A., Green, R. J., Kurmaev, E. Z., Kumada, N., Belik, A. A., & Moewes, A. (2012). Band-gap engineering in TiO 2-based ternary oxides. Physical Review B, 85(19), 195201.

[19] Thimsen, E., Biswas, S., Lo, C. S., & Biswas, P. (2009). Predicting the band structure of mixed transition metal oxides: theory and experiment. The Journal of Physical Chemistry C, 113(5), 2014-2021.

[20] C. Friedel, CR Hebd. Acad. Sci., 77, 211–214 (1873)

[21] Rogers, A. (1922). "Delafossite from Kimberly, Nevada" (PDF). American Mineralogist. 7: 102–104.

[22] Marquardt, M. A., Ashmore, N. A., & Cann, D. P. (2006). Crystal chemistry and electrical properties of the delafossite structure. Thin Solid Films, 496(1), 146-156.

[23] Marquardt, M. A., Ashmore, N. A., & Cann, D. P. (2006). Crystal chemistry and electrical properties of the delafossite structure. Thin Solid Films, 496(1), 146-156.

[24] Yu, M., Draskovic, T. I., & Wu, Y. (2014). Cu (I)-based delafossite compounds as photocathodes in p-type dye-sensitized solar cells. Physical Chemistry Chemical Physics, 16(11), 5026-5033.

[25] Tsuboi, N., Tosaka, K., Kobayashi, S., Kato, K., & Kaneko, F. (2008). Preparation of delafossite-type CuYO2 films by solution method. Japanese Journal of Applied Physics, 47(1S), 588.

[26] Ohashi, M., Iida, Y., & Morikawa, H. (2002). Preparation of CuAlO2 films by wet chemical synthesis. Journal of the American Ceramic Society, 85(1), 270-272.

[27] Tonooka, K., Shimokawa, K., & Nishimura, O. (2002). Properties of copper–aluminum oxide films prepared by solution methods. Thin Solid Films, 411(1), 129-133.

[28] Beznosikov, B. V., & Aleksandrov, K. S. (2009). Predictions of compounds in the family of delafossites. Journal of Structural Chemistry, 50(1), 102-107.

[29] Read, C. G., Park, Y., & Choi, K. S. (2012). Electrochemical synthesis of p-type CuFeO2 electrodes for use in a photoelectrochemical cell. The journal of physical chemistry letters, 3(14), 1872-1876.

[30] Prévot, M. S., Guijarro, N., & Sivula, K. (2015). Enhancing the Performance of a Robust Sol–Gel-Processed p-Type Delafossite CuFeO2 Photocathode for Solar Water Reduction. ChemSusChem, 8(8), 1359-1367.

[31] Gu, J., Yan, Y., Krizan, J. W., Gibson, Q. D., Detweiler, Z. M., Cava, R. J., & Bocarsly, A. B. (2014). p-Type CuRhO2 as a self-healing photoelectrode for water reduction under visible light. Journal of the American Chemical Society, 136(3), 830-833.

[32] Avila, J. I., Matelon, R. J., Trabol, R., Favre, M., Lederman, D., Volkmann, U. G., & Cabrera, A. L. (2010). Optical properties of Pd thin films exposed to hydrogen studied by transmittance and reflectance spectroscopy. Journal of Applied Physics, 107(2), 023504.

[33] Joshi, T., Senty, T. R., Trappen, R., Zhou, J., Chen, S., Ferrari, P., ... & Cabrera, A. L. (2015). Structural and magnetic properties of epitaxial delafossite CuFeO2 thin films grown by pulsed laser deposition. Journal of Applied Physics, 117(1), 013908.

[34] Aktas, O., Truong, K. D., Otani, T., Balakrishnan, G., Clouter, M. J., Kimura, T., & Quirion, G. (2011). Raman scattering study of delafossite magnetoelectric multiferroic compounds: CuFeO2 and CuCrO2. Journal of Physics: Condensed Matter, 24(3), 036003.

[35] Pavunny, S. P., Kumar, A., & Katiyar, R. S. (2010). Raman spectroscopy and field emission characterization of delafossite CuFeO 2. Journal of Applied Physics, 107(1), 013522.

[36] Pellicer-Porres, J., Segura, A., Ferrer-Roca, C., Martinez-Garcia, D., Sans, J. A., Martinez, E., ... & Rodríguez-Hernández, P. (2004). Structural evolution of the CuGaO 2 delafossite under high pressure. Physical Review B, 69(2), 024109.

[37] Biesinger, M. C., Lau, L. W., Gerson, A. R., & Smart, R. S. C. (2010). Resolving surface chemical states in XPS analysis of first row transition metals, oxides and hydroxides: Sc, Ti, V, Cu and Zn. Applied Surface Science, 257(3), 887-898.

[38] Ghijsen, J., Tjeng, L. V., Van Elp, J., Eskes, H., Westerink, J., Sawatzky, G. A., & Czyzyk, M. T. (1988). Electronic structure of Cu 2 O and CuO. Physical Review B, 38(16), 11322.

[39] Poulston, S., Parlett, P. M., Stone, P., & Bowker, M. (1996). Surface oxidation and reduction of CuO and Cu2O studied using XPS and XAES. Surface and Interface Analysis, 24(12), 811-820.

[40] Christopher, J., & Swamy, C. S. (1992). Catalytic activity and XPS investigation of dalofossite oxides, CuMO2 (M= Al, Cr or Fe). Journal of materials science, 27(5), 1353-1356.

[41] Biesinger, M. C., Payne, B. P., Grosvenor, A. P., Lau, L. W., Gerson, A. R., & Smart, R. S. C. (2011). Resolving surface chemical states in XPS analysis of first row transition metals, oxides and hydroxides: Cr, Mn, Fe, Co and Ni. Applied Surface Science, 257(7), 2717-2730.

[42] Paparazzo, E. (1987). XPS and auger spectroscopy studies on mixtures of the oxides SiO2, Al2O3, Fe2O3 and Cr2O3. Journal of electron spectroscopy and related phenomena, 43(2), 97-112.

[43] Hawn, D. D., & DeKoven, B. M. (1987). Deconvolution as a correction for photoelectron inelastic energy losses in the core level XPS spectra of iron oxides. Surface and interface analysis, 10(2-3), 63-74.

[44] Lekse, J. W., Underwood, M. K., Lewis, J. P., & Matranga, C. (2012). Synthesis, Characterization, Electronic Structure, and Photocatalytic Behavior of CuGaO2 and CuGa1–x Fe x O2 (x= 0.05, 0.10, 0.15, 0.20) Delafossites. The Journal of Physical Chemistry C, 116(2), 1865-1872.

[45] Chen, H. Y., & Wu, J. H. (2012). Transparent conductive CuFeO 2 thin films prepared by sol–gel processing. Applied Surface Science, 258(11), 4844-4847.

[46] Benko, F. A., & Koffyberg, F. P. (1987). Opto-electronic properties of p- and n-type delafossite, CuFeO2. Journal of Physics and Chemistry of Solids, 48(5), 431-434.

[47] Ong, K. P., Bai, K., Blaha, P., & Wu, P. (2007). Electronic structure and optical properties of AFeO2 (A= Ag, Cu) within GGA calculations. Chemistry of materials, 19(3), 634-640.

[48] Galakhov, V. R., Poteryaev, A. I., Kurmaev, E. Z., Anisimov, V. I., Neumann, M., Lu, Z. W., ... & Zhao, T. R. (1997). Valence-band spectra and electronic structure of CuFeO 2. Physical Review B, 56(8), 4584.

[49] Haycock, B. J., Rice, M. K., & Lewis, J. P. (2014). High-throughput calculations of alloyed delafossite materials: Application to CuGa 1− xFexO 2. Computational Materials Science, 86, 155-164.

[50] Nie, X., Wei, S. H., & Zhang, S. B. (2002). Bipolar doping and band-gap anomalies in delafossite transparent conductive oxides. Physical review letters, 88(6), 066405.

[51] Freund, H. J., & Roberts, M. W. (1996). Surface chemistry of carbon dioxide. Surface Science Reports, 25(8), 225-273.

[52] Redhead, P. A. (1962). Thermal desorption of gases. Vacuum, 12(4), 203-211.

[53] Kato, S., Fujimaki, R., Ogasawara, M., Wakabayashi, T., Nakahara, Y., & Nakata, S. (2009). Oxygen storage capacity of CuMO 2 (M= Al, Fe, Mn, Ga) with a delafossite-type structure. Applied Catalysis B: Environmental, 89(1), 183-188.

[54] Isahak, W. N. R. W., Ramli, Z. A. C., Ismail, M. W., Ismail, K., Yusop, R. M., Hisham, M. W. M., & Yarmo, M. A. (2013). Adsorption–desorption of CO 2 on different type of copper oxides surfaces: Physical and chemical attractions studies. Journal of CO2 Utilization, 2, 8-15.

[55] Breyer, C., Reichert, D., Seidel, J., Hüttl, R., Mertens, F., & Kureti, S. (2015). Kinetic modeling of the adsorption and desorption of CO 2 on α-Fe 2 O 3. Physical Chemistry Chemical Physics, 17(40), 27011-27018.

[56] Ramos-Moore, E., Diaz-Droguett, D.E., Spring, P., Evans, J.T. and Cabrera, A.L. (2011). Generation of oxygen vacancies in the surface of ferroelectric Pb (Nb, Zr, Ti) O 3. Applied Surface Science, 257:4695-4698

[57] Marquardt, M. A., Ashmore, N. A., & Cann, D. P. (2006). Crystal chemistry and electrical properties of the delafossite structure. Thin Solid Films, 496(1), 146-156.

[58] Ross, J. R. (2011). Heterogeneous catalysis: fundamentals and applications. Elsevier

[59] R. Chang and K. Goldsby, "Chemistry", McGraw-Hill Companies, 11ST Edition, 2012.

[60] Manual, O. (2003). Models RGA100, RGA200, and RGA300 Residual Gas Analyzer.

[61] C. Kittel, "Introduction to Solid State Physics", Reverté, 3ST Edition, 2003.

[62] C. Suryanarayana and M Grant Norton, "X-Ray Diffraction, A Practical Approach", Plenum Press, 1ST Edition, 1998.

[63] Gardiner, D.J. (1989). Practical Raman spectroscopy. Springer-Verlag. ISBN 978-0-387-50254-0.

[64] Tauc, J.; Grigorovici, R.; Vancu, A. (1966). "Optical Properties and Electronic Structure of Amorphous Germanium". Physica status solidi (b). 15 (2): 627

[65] Davis, E. A.; Mott, N. F. (1970). "Conduction in non-crystalline systems V. Conductivity, optical absorption and photoconductivity in amorphous semiconductors". Philosophical Magazine A. 22 (179): 903–922